Pontifícia Universidade Católica
do Rio de Janeiro

Verônica da Rocha Weaver

Modeling of a two-phase thermosyphon loop with low environmental impact refrigerant applied to electronic cooling

Dissertação de Mestrado

Dissertation presented to the Programa de Pós graduação em Engenharia Mecânica of PUC-Rio in partial fulfillment of the requirements for the degree of Mestre em Engenharia Mecânica.

Advisor: José Alberto dos Reis Parise

Rio de Janeiro
Outubro de 2020

Pontifícia Universidade Católica
do Rio de Janeiro

Verônica da Rocha Weaver

Modeling of a two-phase thermosyphon loop with low environmental impact refrigerant applied to electronic cooling

Dissertation presented to the Programa de Pós-graduação em Engenharia Mecânica of PUC-Rio in partial fulfillment of the requirements for the degree of Mestre em Engenharia Mecânica. Approved by the Examination Committee:

Prof. José Alberto dos Reis Parise
Advisor
Departamento de Engenharia Mecânica – PUC-Rio

Prof. Florian Alain Yannick Pradelle
Departamento de Engenharia Mecânica – PUC-Rio

Prof. Sergio Leal Braga
Departamento de Engenharia Mecânica – PUC-Rio

Prof. Enio Pedone Bandarra Filho
UFU

Rio de Janeiro, October 6th, 2020

Verônica da Rocha Weaver

The author graduated in Mechanical Engineering from Pontifícia Universidade Católica do Rio de Janeiro – PUC-Rio in 2017

Bibliographic data

Weaver, Verônica da Rocha

Modeling of a two-phase thermosyphon loop with low environmental refrigerante impact applied to electronic cooling/Verônica da Rocha Weaver; advisor José Alberto Reis Parise. – Rio de Janeiro: PUC-Rio, Departamento de Engenharia Mecânica, 2020.

115 f.: il. ; 29,7 cm

1. Dissertação (mestrado) – Pontifícia Universidade Católica do Rio de Janeiro, Departamento de Engenharia Mecânica.

Inclui bibliografia

1.Introduction. 2.State-of-the-art review. 3.Mathematical model. 4.Numerical solution. 5.Results. 6. Concluding remarks and considerations. II Pontifícia Universidade Católica do Rio de Janeiro. Departamento de Engenharia Mecânica. III. Título.

CCD: 004

Acknowledgements

As we are going through this trying times where a global pandemic has shaken our world, and forced us to re-evaluate our priorities in life, I am happy to be able to give thanks to people that were essential in the development of this work.

First and foremost, I would like to thank my advisor Prof. José Alberto Reis Parise who has accompanied me through my undergrad and now masters' degree. He has provided the guidance I needed in both the academic and personal matters, as a sort of father figure, who has always been able to calm me. I will forever cherish all our conversations.

I would also like to show my gratitude towards my fellow colleagues Vanessa Bautista, Marcus Pinto and Bernardo Landim, who shared a working space with me before the pandemic hit, and were a source of support with their kind words of encouragement, and shared knowledge, which helped me in this dissertation. Further, to Dr. Paul Ortega who has also been a source of support during the time of this work, and other projects throughout these years.

Additionally, to my boyfriend, Lucas Lima, who listened attentively while I talked about my work even when he did not understand any of it yet, tried his best to encourage me, and provided good advice throughout these years. His support was essential in the development of this work.

Moreover, to my friends and family which who put up with me as I complained my way through this degree, which is always a part of the process. As, if it was easy, then it would not be worth it.

Furthermore, I want to dedicate this work to my grandmother, Tanya Chagas Pereira, who has fallen ill in the last four years, but has shown so much strength fighting through it all, including after being diagnosed with COVID-19. She has always been an extraordinarily strong woman, and she keeps showing it every single day.

Finally, to CNPq, PUC-Rio, and Honeywell for their financial support.

This study was financed in part by the Coordenação de Aperfeiçoamento de Pessoal de Nível Superior - Brasil (CAPES) - Finance Code 001.

Abstract

Weaver, Verônica da Rocha; Parise, José Alberto Reis (Advisor). Modeling of a two-phase thermosyphon loop with low environmental impact applied to electronic cooling. Rio de Janeiro, 2020. 115p. Dissertação de Mestrado - Departamento de Engenharia Mecânica, Pontifícia Universidade Católica do Rio de Janeiro.

Given the constant advances in technology, electronic devices have been going through a process of miniaturization while sustaining an increase in power. This trend proves to be a challenge for thermal management since commonly electronic cooling systems are air-based, so that the low heat transfer coefficient of air limits its capacity to keep up with the thermal needs of today's industry. In this respect, two-phase cooling has been regarded as a promising solution to provide adequate cooling for electronic devices.

Two-phase thermosyphon loops combine the technology of two-phase cooling with its inherent passive nature, as the system does not require a pump to provide circulation for its working fluid, thanks to gravity and buoyancy forces. A micro-channel heat sink located right on top of the electronic device dissipates the heat generated. This makes for an energy and cost-efficient solution. Moreover, having a thermosyphon loop operating with a low GWP refrigerant such as R-1234yf results in low impact for the environment since it is an environmentally friendly refrigerant, and the system has low to none energy consumption.

This work provides a detailed numerical model for the simulation of a two-phase thermosyphon loop operating under steady-state conditions. The loop comprises an evaporator (chip and micro-fin heat sink), a riser, a tube-in-tube water-cooled condenser and a downcomer. Fundamental and constitutive equations were established for each component. A finite-difference method, 1-D for the flow throughout the thermoysphon's components and 2-D for the heat conduction in the evaporator and chip, was employed. The model was validated against experimental data for refrigerant R134a, showing a mass flux discrepancy of around 6% for when the system operated under gravity dominant regime. The predicted evaporator inlet pressure showed a maximum relative error of 4.8% when compared to the experimental results. Also, the chip temperature's largest discrepancy was lower than 1°C.

Simulations were performed to present a performance comparison between R134a and its environmentally friendly substitute, R1234yf. Results showed that when the system operated with R134a, it yielded a higher evaporator inlet pressure as well as a higher mass flux. Because of that, R134a was able to keep the chip temperature lower than R1234yf. Yet, that difference in chip temperature was slightly lower than 1°C, showing R1234yf as comparable in performance to R134a. In addition, the safety factor of the system's operation was evaluated for both refrigerants, and for a maximum chip heat flux of 33.1 W/cm^2, R1234yf showed a safety factor above 3. This means the thermosyphon loop can operate safely under the critical heat flux.

Given the investigation on the performance comparison of refrigerants R134a and R1234yf, results pointed to R1234yf being a great environmentally friendly substitute for R134a for the two-phase thermosyphon loop.

Keywords

Modeling, thermosyphon loop, two-phase flow, low GWP, electronic cooling, passive cooling, heat sink, R1234yf, chip cooling, microchannel, thermal performance, low energy consumption, data center

Resumo

Weaver, Verônica da Rocha; Parise, José Alberto Reis (Advisor). Modelagem de um circuito de termossifão de baixo impacto ambiental com aplicação em resfriamento de eletrônicos. Rio de Janeiro, 2020. 115p. Dissertação de Mestrado - Departamento de Engenharia Mecânica, Pontifícia Universidade Católica do Rio de Janeiro.

Diante dos constantes avanços da tecnologia os dispositivos eletrônicos vêm passando por um processo de miniaturização, ao mesmo tempo em que sustentam um aumento de potência. Essa tendência se mostra um desafio para seu gerenciamento térmico, uma vez que os sistemas de resfriamento típicos para eletrônicos utilizam ar como fluido de trabalho, e o seu baixo coeficiente de transferência de calor limita sua capacidade de atender às necessidades térmicas da indústria atual. Nesse sentido, o resfriamento bifásico tem sido considerado uma solução promissora para fornecer resfriamento adequado para dispositivos eletrônicos.

Circuitos de termossifão bifásico combinam a tecnologia de resfriamento bifásico com sua inerente natureza passiva, já que o sistema não requer uma bomba para fornecer circulação para seu fluido de trabalho, graças às forças da gravidade e de empuxo. Um dissipador de calor de microcanais, localizado bem em cima do dispositivo eletrônico, dissipa o calor gerado. Isto o torna uma solução de baixo custo e energia. Além disso, ter um circuito de termossifão operando com um refrigerante de baixo GWP, como o R-1234yf, resulta em baixo impacto para o meio ambiente, uma vez que é um refrigerante ecologicamente correto e o sistema tem baixo ou nenhum consumo de energia.

Este trabalho fornece um modelo numérico detalhado para a simulação de um circuito de termossifão bifásico, operando em condições de regime permanente. O circuito compreende um evaporador (chip e dissipador de calor de micro-aletas), um "riser", um condensador refrigerado a água de tubo duplo e um "downcomer". Equações fundamentais e constitutivas foram estabelecidas para cada componente. Um método numérico de diferenças finitas, 1-D para o escoamento do fluido por todos os componentes do sistema, e 2-D para a condução de calor no “chip” e evaporador foi empregado.

O modelo foi validado com dados experimentais para o refrigerante R134a, mostrando uma discrepância em relação ao fluxo de massa em torno de 6%, para quando o sistema operava sob regime dominado pela gravidade. A pressão de entrada do evaporador prevista apresentou um erro relativo máximo de 4,8% quando comparada aos resultados experimentais. Além disso, a maior discrepância da temperatura do chip foi inferior a 1 ° C.

Simulações foram realizadas para apresentar uma comparação de desempenho entre o R134a e seu substituto ecologicamente correto, R1234yf. Os resultados mostraram que quando o sistema operava com R134a, ele trabalhava com uma pressão de entrada no evaporador mais alta, assim como, com um fluxo de massa mais alto. Por causa disso, o R134a foi capaz de manter a temperatura do chip mais baixa do que o R1234yf. No entanto, essa diferença na temperatura do chip foi levemente inferior a 1°C, mostrando o R1234yf como comparável em desempenho ao R134a. Além disso, o fator de segurança da operação do sistema foi avaliado para ambos os refrigerantes, e para um fluxo de calor máximo do chip de 33,1 W/cm^2, R1234yf mostrou um fator de segurança acima de 3. Isso significa que o circuito de termossifão pode operar com segurança abaixo do ponto crítico de fluxo de calor.

Dada a investigação sobre a comparação de desempenho dos refrigerantes R134a e R1234yf, os resultados apontaram o R1234yf como um excelente substituto ecologicamente correto para o R134a, para operação em um circuito de termossifão bifásico.

Palavras-Chave

Modelagem, circuito de termossifão, escoamento bifásico, baixo GWP, resfriamento de eletrônicos, resfriamento passivo, dissipador de calor, R1234yf, resfriamento de chip, micro canais, performance térmica, baixo consumo de energia, data center

Summary

List of Figures

List of Tables

List of Symbols and Abbreviations

List of Latin Letters

A	Heat transfer area; $[m^2]$
A_v	Bubble nose acceleration, $[m/s^2]$
asp	Aspect ratio, $[-]$
B	Matrix of coefficients of the 2-D heat conduction; $[-]$
b	Coefficient of matrix B; $[-]$
C	Constant, $[-]$
c_p	Specific heat, $[J/(kg.K)]$
D	Diameter, $[m]$
d_{eq}	Equivalent diameter, $[m]$
d_h	Hydraulic diameter, $[m]$
d_{heat}	Heated diameter, $[m]$
E	Liquid entrainment fraction; $[-]$
f	Friction factor, $[-]$
fr	Bubble frequency, $[1/s]$
g	Gravity, $[m/s^2]$
G	Mass flux, $[kg/(m^2.s)]$
h	Specific enthalpy, $[J/kg]$
h_{lv}	Latent heat of vaporization, $[J/kg]$
H	Height, $[m]$
I	Vector of independent terms; $[-]$
i	Discretized element in the flow direction; $[-]$
J_v	Superficial vapor velocity; $[m/s]$
k	Pressure drop coeficiente due to a bend; $[-]$
L	Length, $[m]$
$LMTD$	Logarithmic mean temperature difference; $[K]$
L_{ex}	Length of the heat exchange; $[m]$
$\dot{m}$	Mass flow rate, $[kg/s]$
M	Mass; $[kg]$
ny	Number of discretized elements in the y-direction; $[-]$

nz	Number of discretized elements in the z-direction; $[-]$
N	Number, $[-]$
P	Pressure, $[kPa]$
Per	Perimenter; $[m]$
q	Heat; $[W]$
q''	Heat flux, $[W/m^2]$
r	Linear proration factor, $[-]$
Ra	Wall Roughness, $[-]$
S	Cross sectional area, $[m^2]$
SF	Safety factor; $[-]$
T	Temperature, $[K]$
t	Time, $[s]$
th	Thickness
u	Velocity, $[m/s]$
U	Overall heat transfer coefficient; $[W/m^2.K]$
UA	Overall heat transfer conductance; $[W/K]$
$u_{v,0}$	Initial bubble nose velocity, $[m/s]$
u_v	Local bubble nose velocity, $[m/s]$
V	Volume, $[m^3]$
W	Width, $[m]$
x	Vapor quality, $[-]$, or a direction; $[-]$
y	Direction perpendicular to the flow; $[-]$
z	Flow direction, $[-]$

Greek Symbols

α	Heat transfer coefficient, $[W/(m^2.K)]$
β	Coefficient of the void fraction model for annular flow; $[-]$
$\delta_{N,0}$	Initial liquid film thickness, $[m]$
δ_N	Liquid film thickness, $[m]$
δ_{end}	Liquid film thickness at the end of the elongated bubble; $[m]$
δ_{min}	Liquid film thickness at the dry-out zone; $[m]$

δ_{vbl}	Viscous boundary layer thickness, $[m]$
ε	Void fraction, $[-]$
η	Fin efficiency, $[-]$
ϕ	Two-phase multiplier; $[-]$
λ	Thermal conductivity, $[W/(m.K)]$
μ	Dynamic viscosity, $[Pa.s]$
ω	Exponent for the void fraction model for annular flow; $[-]$
ρ	Density, $[kg/m^3]$
τ_w	Wall shear stress; $[Pa]$
θ	Angle between the horizontal and the flow direction, [°]
σ	Surface tension; $[N/m]$

Subscripts

$3Z$	Three-zone model
AF	Annular flow model
a	Acceleration
amb	Ambient
$base$	Relative to the base of the heat sink package
c	Core
$CB-AF$	Coalescing bubble to Annular flow transition
cd	Condenser
ch	Channel
CHF	Critical heat flux
$comp$	Component
dc	Downcomer
$dryfilm$	Relative to the depletion of the liquid film
eq	Equivalent
ev	Evaporator
f	Fin
$film$	Related to the liquid film
fl	Fluid
$fric$	Frictional

ftp	Footprint
i	Discretized element in the flow direction
in	Inlet
j	Discretized element in the y-direction perpendicular to the flow
k	Layer
l	Liquid
lf	Liquid film
lo	Liquid only
lv	Two-phase mixture
max	Maximum
min	Minimum
out	Outlet
ph	Phase
ref	Refrigerant
rs	Riser
sec	Secondary fluid
ST	Standard temperature
v	Vapor
vo	Vapor only
w	Water

Dimensionless numbers

Bl	Boiling number
Bo	Bond number
Ca	Capillary number
Co	Confinement number
F	Froude number
Nu	Nusselt number
P_{red}	Reduced pressure
Pr	Prandtl number
Re	Reynolds number
T^+	Dimensionless liquid film thickness

We	Weber number
Y^*	Dimensionless coordinate

Acronyms

$2U$	Two Units
CPU	Central Processing Unit
$CRAC$	Computer Room Air Conditioners
$CRAH$	Computer Room Air Handlers
FDR	Friction Dominant Regime
GDR	Gravity Dominant Regime
GWP	Global Warming Potential
$LTCM$	Heat and Mass Transfer Laboratory from Ecole Polytechnique Fédérale de Lausanne
ME	Micro-evaporator
$REFPROP$	Reference Fluid Thermodynamic and Transport Properties Database
TIM	Thermal Interface Material

1 Introduction

1.1 Data center and electronic cooling

Ensuring adequate cooling for electronic devices is a necessity since their performance and reliability are dependent on temperature and declining as temperature rises. With the ever-increasing power and miniaturization of electronic devices, thermal management has been facing challenges of insufficient heat removal and highly non-uniform power dissipation (Murshed, 2016). Thus, a great amount of work has been applied in the development of electronic cooling in recent years.

Datacenter thermal management is a branch of electronic cooling which has been receiving considerable attention lately. Thermal management systems have been estimated to account for 30 to 50% (Kheirabadi and Groulx, 2016; Khalaj and Halgamuge, 2017; Sulaiman et al., 2020) of all electricity consumption in data centers, resulting in high operational costs and contributing to a high overall carbon footprint for this facility.

Computer Room Air Conditioners (CRAC) and Computer Room Air Handlers (CRAH) are the most widely used systems for thermal management in data centers. They are both air-cooling based. Some of the present issues with these systems pertain to the low convective heat transfer of air. It presents itself as a problem for new electronic devices, such as high heat flux processors, as their power density is being continuously increased yet the maximum temperature for electronics remains at 85°C. The air's poor performance and the high consumption of power by cooling towers, chillers, water pumps, and circulation fans amount to high energy inefficiencies by these cooling systems (Khalaj and Halgamuge, 2017). For the above, more investigation on energy-efficient technologies, for the cooling of electronics, is needed.

Within a data center, cooling is required by different levels, each one with its own strategy. Figure 1.1 displays the schematics of a multi-level thermal management of data centers, highlighting the different levels from chip to room, with a typical cooling system based on a chilled water plant (CRAH).

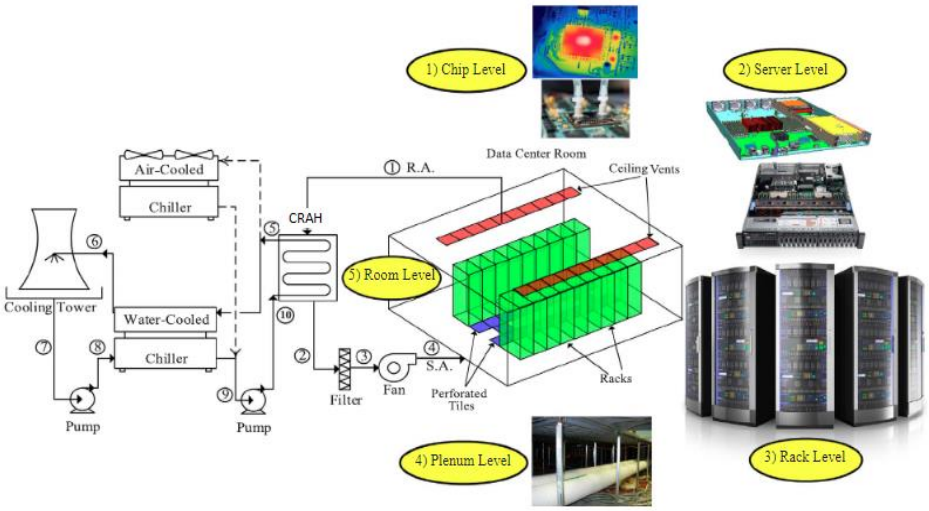

Figure 1.1 - Schematic of multi-level thermal management of data centers (Khalaj and Halgamuge, 2017)

Two-phase liquid cooling is presented as a promising thermal management technology because of its much higher convective heat transfer coefficient compared to air or single-phase liquids, and easy adaptation for chip and server-level applications. Besides, it also reduces thermal resistances by bringing the coolant closer to the heat source. Two-phase liquid cooling can be effective both in direct and indirect contact.

Based on the classification of air and liquid cooling solutions for sever electronics by Kheirabadi and Groulx (2016), and reviews on different thermal management technologies for electronics, Figure 1.2 provides a schematic classifying these cooling strategies.

For “on-chip” two-phase cooling, where the heat sink is attached to the heat source, high heat transfer performance can be achieved by combining its evaporating latent heat transfer with the small footprint area and large heat exchange surface of microchannels (Lamaison et al., 2017).

Indirect passive two-phase liquid cooling entails no power consumption to circulate the working fluid throughout the cooling system. So, in natural circulation systems, the fluid is driven by the temperature difference between the heat source and heat sink, and by capillary action, for heat pipes, or by gravity and buoyancy, for thermosyphon loops.

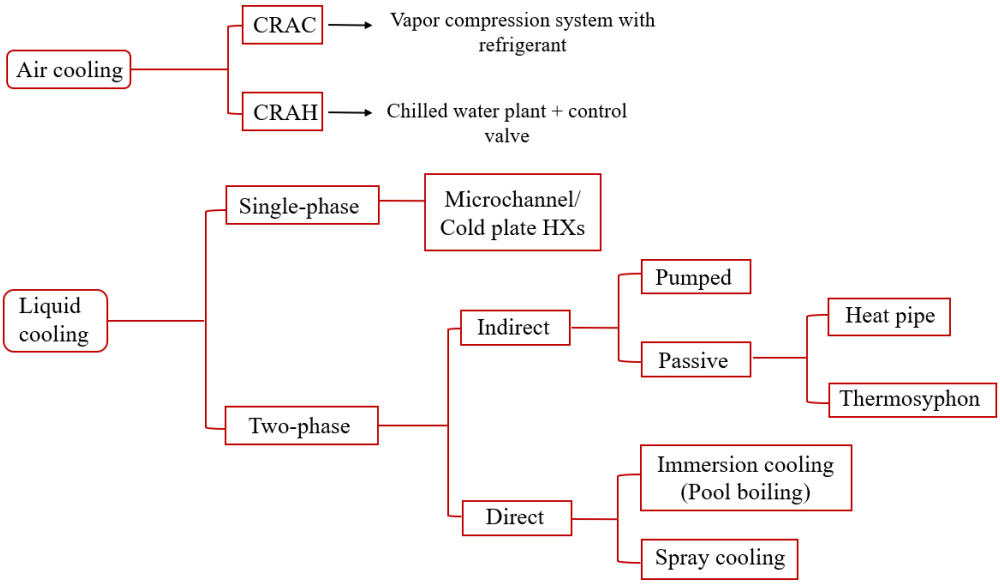

Figure 1.2 - Classification of electronic thermal management technologies

1.2 Two-phase thermosyphon loops

A two-phase thermosyphon loop sometimes referred to as a wickless heat-pipe loop or just natural circulation loop, is a closed-loop typically composed of four main components namely: an evaporator, a condenser, and two tubes that connect both heat exchangers, the riser and downcomer. Due to its passive nature, the thermosyphon loop operation depends on gravity and buoyancy to drive the refrigerant flow throughout the loop. The driving force (static pressure drop) is a product of the difference in height between the condenser and the evaporator, and the difference in density between the high-density single-phase liquid flow in the downcomer and the low-density two-phase flow in the riser. Equilibrium steady-state regime is achieved when the sum of static and frictional pressure drops alongside the entire loop is zero.

The driving potential of the thermosyphon loop yields a much higher mass flow rate and, consequently, a higher heat dissipation rate, compared to capillary heat pipe. Besides, it does not rely on any mechanical component, such as a pump or a compressor in traditional electronic cooling systems, which culminates in a much lower electrical energy consumption (Lamaison et al., 2017). Furthermore, the system can be completely passive by relying on natural convection for an air-cooled condenser. However, even when opting for forced convection in the

condenser, with the addition of fans, or a pump for liquid coolants, which yields greater heat transfer coefficients and thus a higher heat removal capacity, the energy consumption for a pump or fan is still much lower than the electricity consumed by a mechanically driven system, sized to remove the same prescribed heat load for an electronic device. This was confirmed by Lamaison et al. (2018), when the authors estimated a reduction of 95% in electricity consumption for the replacement of an air conditioning system, with a thermosyphon loop system instead, for the cooling of an existing 2U server.

In addition to the lower energy consumption of the closed thermosyphon loop system, the exemption of mechanical components means a more reliable system. Without moving parts, it is possible to reduce costs, vibrations that could upset the electronic apparatuses and, consequently, reduce noise levels (Ong et al. , 2017). The possible drawback of the thermosyphon loop system is regarding instabilities and flow reversal, so the system must be carefully designed for its whole range of operation, so as to avoid undesirable operational problems such as evaporator dry out, difficult start-up or condenser flooding (Agostini and Yesin, 2008).

Figure 1.3 illustrates a thermosyphon loop system and its components placements.

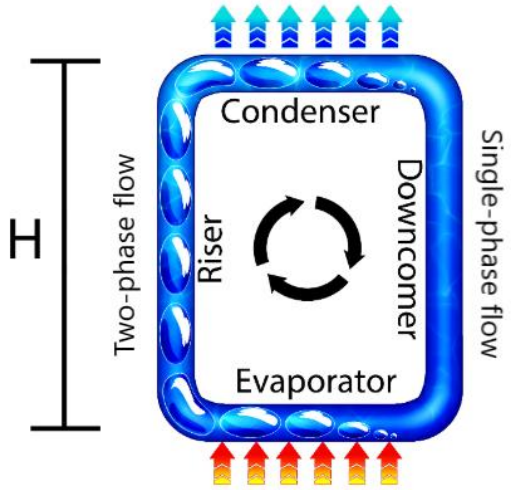

Figure 1.3 – Schematic of a thermosyphon loop system (Seuret et al., 2018)

Heat dissipated by an electronic component is absorbed by the refrigerant flowing through the evaporator, where it boils leaving it as a liquid-vapor mixture.

This two-phase flow ascends through the riser into the condenser by the driving potential of the system, as explained earlier. While in the condenser, the fluid is cooled by a heat transfer fluid which essentially removes the heat dissipated by the device. Subcooled liquid refrigerant exits the condenser, and then flows back, by means of gravity, to the evaporator passing through the downcomer. This system operation allows for the necessary cooling of the electronic device attached to the evaporator. It is important to note that the refrigerant flow rate is: i) adjustable according to the heat load imposed by the electronic component, and ii) is self-sustained as long as heat is being applied in the evaporator and removed in the condenser.

1.3 Working fluid considerations

Working fluids of thermosyphon loops operate at approximately the same temperature and pressure levels that of vapor compression refrigeration cycles. Therefore, to determine the working fluid to be employed in a two-phase thermosyphon loop, same considerations as in refrigeration have to be taken into account. A brief history on the progress of refrigerants throughout the years is provided below. Additionally, a specific section is dedicated to working fluids on the state-of-the-art review in chapter 2.

Figure 1.4 shows a schematic developed by Calm (2008) on the progress of refrigerants.

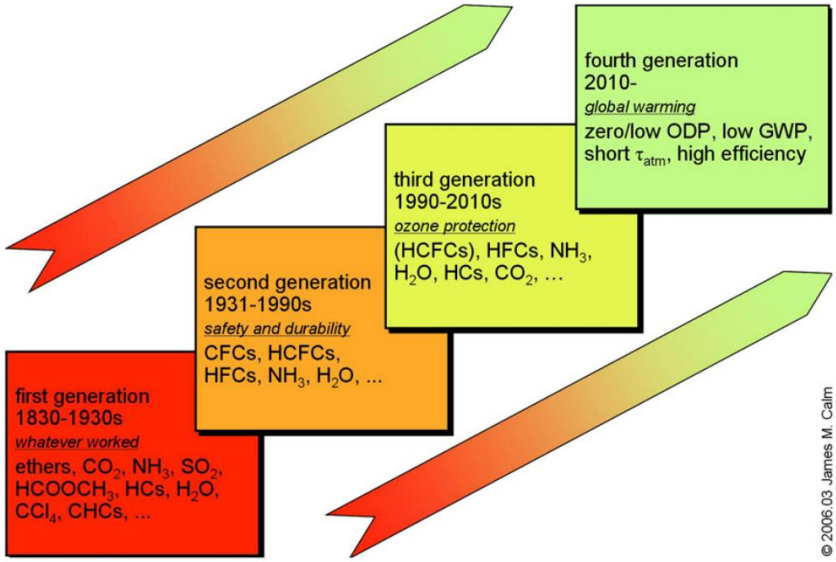

Figure 1.4 – Refrigerant progression throughout the years (Calm, 2008)

As shown in Figure 1.4, Calm (2008) identified four generations of refrigerants, each one with its highlighted characteristics.

The first generation which covered 100 years was marked as “whatever worked” since refrigerants were chosen regarding only their availability and provided result. Calm (2008) noted that most of these refrigerants were highly flammable, toxic, or both, and because of it, prone to accidents. Accordingly, a new generation of refrigerants emerged with the need for safety and durability. The industry solutions were chlorofluorocarbons (CFCs) and hydrochlorofluorocarbons (HCFCs) which were primarily stable, non-toxic nor flammable. The CFCs and HCFCs dominated the second generation of refrigerants, however, CFCs were later linked to the depletion of the planet’s ozone layer. And with that, the Montreal Protocol forced the banning of CFCs and limited the application of HCFCs by planning a phaseout.

As HCFCs had its employment limited, hydrofluorocarbons (HFCs) as well as natural refrigerants such as ammonia, carbon dioxide, water and hydrocarbons were researched, manufactured, and employed by industry.

Global concerns regarding climate change, however, lead to legislation restrictions in order to reduce greenhouse gas emissions that cause global warming. Therefore fluorochemicals (“F-gas”) refrigerants, such as HFCs have been facing gradual restrictions and even banning for certain applications. While these limitations on HFCs employment are underway, research on alternative refrigerants that have a low GWP (global warming potential), also fulfilling the needs of the second and third generation, has been developed. Therefore, a fourth generation of refrigerants can now be identified.

Hydrofluoroolefins (HFOs) have been investigated in the past decade, as some of them are being considered as potential alternatives to HFCs due to their extremely low GWP. However, due to their mild flammability its application is still being studied.

1.4 Motivation and objective

The motivation of this work comes down to investigating an energy-efficient technology that allows for more reliable and cost-effective operations.

Passive two-phase cooling shows great promise for replacing air-cooling technologies for electronic devices. Having detailed the operation of thermosyphon loop systems, the main objective of this work is to develop a numerical model of a two-phase thermosyphon loop while also evaluating its operation with a low GWP refrigerant, R1234yf, for on-chip electronic cooling (the chip is attached to the evaporator's cold plate). With that, contributing to the investigations being made on thermosyphon loops for electronic cooling.

Secondarily, this work was set out to provide a deep understanding of the operations and processes of the two-phase thermosyphon loop, when modeling each heat exchanger, and the loop as a whole.

The contribution of this work, is the development of a model based on fundamental balance equations, resulting in a general model, able to evaluate the performance of different working fluids, as well as distinct geometries. Only the pressure drop due to possible bends is based on a semi-generic model which is specific to the LTCM experimental apparatus.

The numerical model is validated with experimental data for refrigerant R134a. In addition, a numerical study on the comparison of the thermal performance of the system operating with R134a and R1234yf is performed. Futhermore, an extensive literature survey on modeling of a two-phase thermosyphon loop applied to electronic cooling was carried out.

1.5 Work outline

This dissertation is organized as follows. A literature survey is presented in Chapter 2. The entire mathematical model is described in Chapter 3 whereas the numerical solution is presented in Chapter 4. Results, including grid independence test, model validation against experimental data and parametric analysis, are discussed in Chapter 5. Finally, in Chapter 6, conclusions are drawn and suggestions for future work are put forward.

2 State-of-the-art review

As two-phase flow has been thoroughly studied over the years, natural circulation loops such as the thermosyphon loop have also been extensively investigated both by numerical and experimental studies, since the 1980s (Ramos et al., 1985; Chen and Chang, 1988; Lin and Faghri, 1997; Jeng and Pan,1999). In order to deliver a brief state-of-the-art review, the focus of the present work will be on the modeling of two-phase thermosyphon loops applied to electronic cooling. Some experimental works on this technology will also be highlighted to paint a complete picture of the developments of the thermosyphon loop for electronic cooling throughout the years.

Investigation on two-phase thermosyphon loops for electronic cooling began to surface during the end of the ‘90s and has continued ever since. Leading works on experimental investigations (Chu et al, 1999; Min-Kyun Na et al., 2001; Khodabandeh, 2004; Khodabandeh, 2005; Chang et al., 2010) and the modeling (Haider et al., 2002) of thermosyphon loops have been developed to study the complex behavior of the system. Datacenter cooling is also an application for which the two-phase thermosyphon loop has been investigated since most of the electricity consumption in a data center is linked to cooling. Recent studies such as Nadjahi et al. (2020) and Zhang et al. (2017) have been published, but they are outside the scope of this review since cooling provided by the thermosyphon loop, is for the air inside a data center instead of the electronic equipment (not for chip or server levels) even though the heat load is originated by the equipment.

2.1 Modeling

Computer cooling by a thermosyphon loop with mini channels was investigated numerically by Bieliński and Mikielewicz (2010). They studied the interaction between mass flow rate and heat load, and were able to identify and later to detail (Bieliński and Mikielewicz, 2011) the findings of two operational regimes for the thermosyphon loop as seen in Figure 2.1. In the first regime, for low to medium heat loads, the increase in the imposed heat load results in an increase of the mass flow rate of the system. They named it the gravitational dominant regime

(GDR). They explained it by highlighting that, when the thermosyphon is operating under this regime, a small increase of vapor quality culminates in a large rise in void fraction and thus, density and buoyancy force. However, the continued conversion of higher density liquid in lower density vapor, caused by the rise in heat load, increases the velocity of the mixture which leads to a rise of the frictional force. So, after achieving a point of maximum refrigerant mass flow rate, for high heat loads, they noted a decrease of mass flow rate with the continuing increase of heat load and called it the friction dominant regime (FDR). The plotting of the mass flow rate as a function of the imposed heat load, is now regarded as the characteristic curve of a thermosyphon loop system.

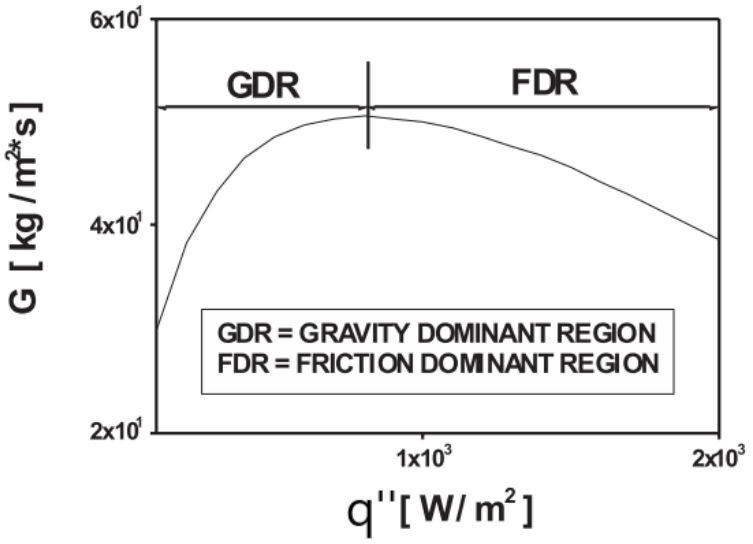

Figure 2.1 Mass flux rate as a function of imposed heat flux
(Bieliński and Mikielewicz, 2010)

Agostini et al. (2011) developed a numerical model only for the air-cooled condenser of a thermosyphon loop for cooling two power modules ABB Hipak, operating with R245fa as the working fluid. Their model was validated experimentally, for the mean temperature of the panel of the condenser as a function of dissipated power. For a heat load varying from 250 to 1500W, the authors reported that a good agreement was obtained, although the error was not disclosed. Following this study, Agostini et al. (2014) simulated a double loop thermosyphon system for electronic cooling. This configuration was proposed to allow higher flexibility in installation and operation and was not specific to any electronic device.

The loops were connected in cascade with the evaporator of the second loop being attached to the condenser of the first loop. The authors also performed an experimental study and noted that results for total thermal resistance, differed 33.6% between experimental and numerical data for the lowest heat load while only 2.8%, for the highest. The authors then concluded that, for low heat loads, the model and its correlations did not represent the system well.

Over the years, a team of researchers from the LTCM laboratory at the Ecole Polytechnique Fédérale de Lausanne has developed a series of works on the thermosyphon loop applied to the cooling of electronic equipment. For all numerical models, the authors considered one-dimensional flow throughout the loop and two-phase flow as homogeneous. Treating the two-phase flow as homogeneous simplifies the process of computing its thermo-physical properties, since it considers the flow as a single-phase flow, so that the vapor and liquid phases move at the same speed.

These LTCM works are displayed over a timeline in Figure 2.2.

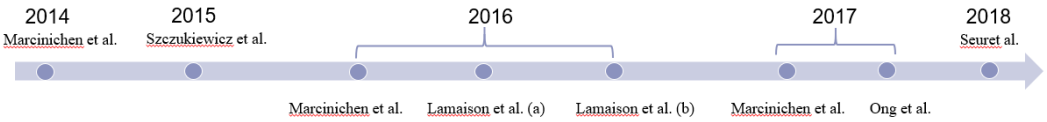

Figure 2.2 – Timeline of LTCM works on modeling two-phase thermosyphon loop for electronic cooling

Marcinichen et al. (2014) modeled this system for cooling a server in a data center. In this study, the authors also carried out an extensive parametric study, detailed in a later section, to understand how key parameters affected the hydrodynamic and thermal performance of the system operating in steady state. The authors also took account of the frictional drop across the whole loop and illustrated that the evaporator, followed by the condenser, was shown to be the major sources of frictional pressure drop for the loop. They concluded that these components could be improved by reducing their frictional pressure drops. Simulations for transient states for the micro-evaporator of a thermosyphon loop of 10 cm of height operating with R134a were also performed. Throughout the whole simulations, the system was able to keep the chip's temperature below 85°C and without the risk of dry out.

Szczukiewicz et al. (2015) added to the work of Marcinichen et al. (2014) by carrying out a thermo-economic analysis of a double thermosyphon loop system applied to a datacenter rack. The findings of the study provided by the authors are described in detail later in the thermo-economic analysis section.

The LTCM laboratory team, after conducting a number of numerical studies on two-phase thermosyphon loop, as previously described, carried out a four-part series. The first one was an experimental campaign, and the following were: a steady-state model, a transient model, and finally the application of the transient model to the cooling of 2U servers. All the presented models were validated against the experimental data from part 1, which is detailed in the following experimental work section.

Marcinichen et al. (2016) developed a steady-state simulation for the thermosyphon loop for the second part series and validated it against the experimental data presented by Ong et al. (2016). They chose a water-cooled tube-in-tube condenser and assumed a constant overall heat conductance estimating its value from the average of experimental results. The micro-evaporator used was one of the designs presented by Marcinichen et al. (2014).

For part 3, Lamaison et al. (2016a) presented a dynamic model for the thermosyphon loop, opting to include a liquid accumulator in the system. Previously the models presented by the team from LTCM were all steady-state except for the modeling of the evaporator in Marcinichen et al. (2014). The authors applied the conservation equations to all components considering the mass flow rate the same for all cells at each time step and neglecting the accumulation term in the momentum equation, arguing that the pressure gradient exhibited very fast dynamics. They also took the heat loss along the piping into account, instead of assuming adiabatic piping as the previously stated models (Marcinichen et al., 2014, Szczukiewicz et al., 2015 and Marcinichen et al., 2016). Dynamic energy equations were solved for each component and time-dependent conduction in the evaporator package was evaluated. For the liquid accumulator, they opted for a lumped capacitance model. They experimentally validated this model, and results are presented on a later section.

Following the experimental validation of the transient model presented in part 3, Lamaison et al. (2016b) took the same dynamic code and applied it to the cooling of two CPUs of the server HP ProLiant DL180 G6, which has a maximum

heat load of 80W each. However, for this application, the height of the thermosyphon must be lower than 8cm. The thermosyphon loop is split into two parallel loops, as shown in Figure 2.3, with the main downcomer distributing its flow between two microchannel evaporators, whose outlets flows meet up at the main riser, to pass through to the single water-cooled microchannel condenser at the outlet of the condenser. Then the flow goes to the liquid accumulator which ensures that the subcooled liquid flows to the main downcomer.

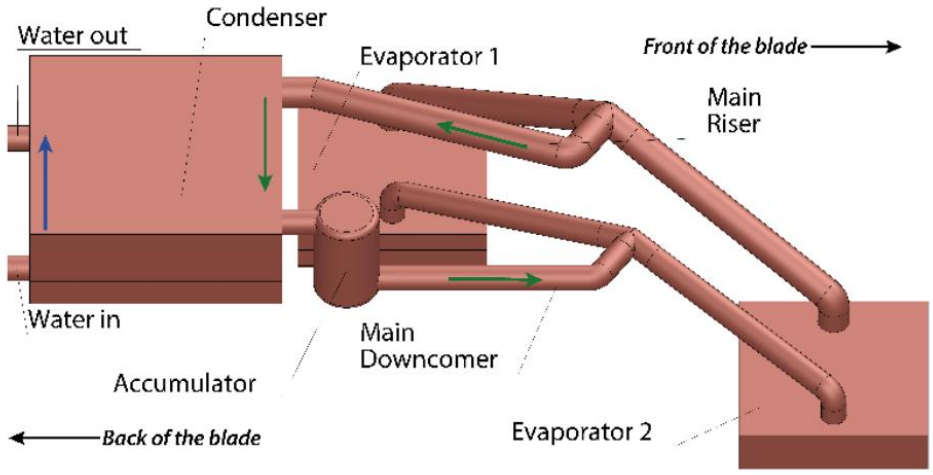

Figure 2.3 – Mini two-phase thermosyphon loop proposed for 2U blade cooling (Lamaison et al., 2016b)

The authors then performed a parametric study by having a benchmark experiment and simulating various cases where they varied significant parameters to investigate their influence on the system's performance. The parameters evaluated were: working fluid, riser and downcomer diameters, secondary fluid mass flow rate, the inlet temperature of the secondary fluid in the condenser, and filling ratio (ratio of the volume of refrigerant to the volume of the system). For all cases simulated, both gravity and friction dominant regimes were evident from characteristic curves of mass flow rate as a function of input heat flux.

Marcinichen et al. (2017) investigated numerically two different types of condensers for the thermosyphon loop. The first one was an air-cooled louvered-fin flat-tube condenser and the second, an ultra-compact counter-flow heat exchanger with R134a as the secondary fluid. The architecture of both condensers differs from the tube-in-tube presented in the former works. This investigation is also part of a 4-part series on two-phase liquid cooling systems for electronics. The first one

encompassed a state-of-the-art review and provided a numerical analysis on a pumped two-phase loop for electronic cooling. The second and third parts each consisted of experimental campaigns on a thermosyphon loop operating with an air-cooled condenser (Amalfi et al. 2017a) and the ultra-compact liquid-cooled condenser (Amalfi et al. 2017b). This study implements the LTCM numerical code on the thermosyphon loop operating with both condensers previously characterized and validate it with the experimental data. A pump-driven loop is also experimentally validated. Afterward, a parametric study was conducted on the thermosyphon loop with the air-cooled condenser for various working fluids and geometric conditions.

The study performed by Ong et al. (2017) centered on adding data for a wider range of imposed heat load for a thermosyphon loop of 15 cm of height, designed to cool a pseudo-chip which emulated a server. The authors performed more experimental tests and provided new validations for the LTCM code on working fluid's mass flow rate, mean chip temperature, and system pressure.

The focus of the work by Seuret et al. (2018) was to provide a new model for a thermosyphon loop with a microchannel water-cooled condenser, operating under steady-state with a better convergence with experimental data. The design of this thermosyphon loop of 8 cm of height was catered to provide cooling for a Virtex 7 FPGA chip with a thermal design power of 60 W. The model was validated for various parameters while also conducting a parametric study. Transient measurements on mean chip temperature were also made explicit in their experimental campaign. A comprehensive report on the geometry of each component of the loop was unfortunately not disclosed.

2.1.1 Parametric studies

A parametric study is an important tool in understanding the complex behavior of the thermosyphon loop system. It consists of varying key input parameters and analyzing the response of the system, in search of the conditions that will lead to greater overall performance.

2.1.1.1 Geometric parameters

Marcinichen et al. (2014) performed an extensive parametric study evaluating the effect of orientation of the evaporator microchannels, horizontal or vertical, diameters of the riser and downcomer, height of the thermosyphon and two different designs for the evaporator on the performance of the system. For the evaporator's designs considered, both had the same cold plate area but distinct cross-sectional channel area and fin width. The evaporator with the higher cross-sectional channel area, showed a higher critical heat flux since its mass flow rate was higher. With both designs, by increasing the thermosyphon height, the critical heat flux rose, and the evaporator's outlet vapor quality decreased as the mass flow rate increased. Results showed that the thermosyphon height is a major factor for the system's performance, since while increasing it, the critical heat flux also raised, as did the working fluid mass flow rate. By its turn, the evaporator's outlet vapor quality was reduced. However, the thermosyphon height showed a negligible effect on the chip temperature. Regarding the evaporator channel orientation, the horizontal channels performed better since the vertical up-flow had a higher overall pressure drop, because of the additional gravitational term, thus performing with a lower mass flow rate. Nonetheless, the difference in performance is minor, in this case, as a result of the short length of the evaporator. Also, both evaporators orientations showed safety factors (ratio of critical to prescribed heat flux) over 1, for a thermosyphon height of 5 cm or above. The authors studied three pairs of risers and downcomers diameters. Throughout their numerical simulation, only the pair with the smallest combination of both riser and downcomer diameters was not able to perform with a thermosyphon height of 5 cm. For this height, superheating was achieved at the outlet of the evaporator. This condition is not good since it can lead to dry out or chip burnout. The authors concluded that a thermosyphon of at least 10 cm of height was better because of its safety factor of 1.6 or over.

One of the main conclusions drawn from the parametric study performed by Lamaison et al. (2016b) was that the reduction of the riser diameter led to a drastic reduction in the working fluid mass flow rate, and in this case, this reduction caused the system to not be able to disperse the amount of heat flux needed for this application which was 7 W/cm^2.

As investigated previously by Marcinichen et al. (2014 and 2017) performed another parametric study on thermosyphon height and riser and downcomer diameters. However, for this application, the height was much bigger, as the authors

studied heights of 50, 75 and 100 cm. Consequently, higher heat loads were imposed. Results confirmed the conclusions of Marcinichen et al. (2014) when the thermosyphon height showed no influence upon the cold plate wall temperature, but a significant one in the mass flow rate of the system. Again, the system operating with the highest height showed a higher mass flow rate. As for the riser and downcomer diameters, two pairs were tested. In both, the riser had a larger diameter because it is beneficial to minimize the two-phase pressure drop in the riser. Once again, the influence of riser and downcomer on the cold plate temperature was negligible, although a better thermal performance was shown for the pair with greater riser and downcomer diameters since it performed with a higher mass flow rate.

2.1.1.2 Secondary fluid conditions

The effect of secondary fluid conditions, such as mass flow rate and inlet temperature on the system's performance, is a subject of interest since they are input conditions for the thermosyphon loop system. Lamaison et al. (2016) decided to study the secondary fluid's inlet temperature as part of their parametric study. They discovered that, by increasing the secondary fluid inlet temperature, the pressure of the working fluid was increased, and resulted in a lower driving potential and thus, a lower mass flow rate. Results showed that the simulated case with higher secondary fluid mass flow rate presented the smallest chip temperatures for a range of heat fluxes.

In their parametric investigation, Seuret et al. (2018) only focused on the influence of the secondary fluid inlet conditions since extensive parametric work on other parameters had already been previously done by other members of their team. For their model, water was used as the coolant for refrigerant R236fa at the microchannel condenser. Three different values for the water mass flow rate (3.59, 4.79 and 6.88 kg/h), and two inlet temperatures (20 and 30.7°C) were investigated for a heat load from 20 to 60 W. This parametric study was also carried out in combination with the experimental validation since, for each case considered, the numerical and experimental responses were displayed together. The influence of water mass flow rate and inlet temperature were investigated against chip temperature, water temperature variation along the condenser, heat losses, and total

thermal resistance. Results showed that the variation of water mass flow rate did not influence the chip temperature substantially. However, the slope of the curve (water mass flow rate as a function of heat load) did slightly increase when the water mass flow rate decreased. A chip temperature increase from about 51°C to 57°C was reported for a reduction of 48% in mass flow rate, at a maximum power of 60W. The increase of the water inlet temperature, from 20 to 30.7°C, shifted the curve upwards, showing a considerable increase in chip temperatures averaged in 11.35°C. However, the slope of this curve remained the same throughout the range of input heat load. Nonetheless, the chip temperature was affected greatly by the specific packaging, and the heat conductivity of their thermal test vehicle was said to be lower than in conventional chips, so this result represents, according to Seuret et al. (2018), the worst-case scenario. The water temperature difference across the condenser was not affected by the inlet temperature. On the other hand, a mass flow rate reduction increases this temperature difference. The heat loss by natural convection was only evaluated experimentally, and defined by Seuret et al. (2018), as the difference between the input electrical power and the heat received by the water. This rate of heat loss was reported to increase with the increase of heat load since, for higher system temperatures, the heat loss is expected also be higher. However, looking at the curves shown by the authors, their results do not always correspond to this trend. For some prescribed heat loads, the heat loss was shown to be reduced when the heat load was increased. The authors did not address this behavior or report on any trend regarding the variation of secondary fluid conditions, only that the total heat loss was below 12%. Finally, the total thermal resistance was shown to decrease when increasing the heat load, since the overall vapor quality increases. It can also be concluded from their results, that an increase in water mass flow rate leads to lower thermal resistance values, and a higher inlet water temperature was shown to result in higher thermal resistance, as expected.

2.1.1.3 Filling ratio

Lamaison et al. (2016b) studied the influence of the filling ratio on the system mass flow rate. The increase of the working fluid filling ratio resulted in a higher mass low rate since it increases the amount of liquid in the accumulator. However, the authors also highlighted that this trend is not always beneficial to the

system performance since a full liquid accumulator causes condenser flooding which is detrimental to the performance.

2.1.1.4 Working fluid

Marcinichen et al. (2014) evaluated numerically the performance of refrigerant R1234ze as an environmentally friendly substitution for R134a. Even though R134a was able to keep the chip temperature about 4.5°C lower than R1234ze, its alternate was found by the authors as an excellent option.

Refrigerants R236fa and R1234ze were tested and compared with R134a for the thermosyphon loop with two parallel evaporators considered in Lamaison et al. (2016b). It was shown that, for low heat fluxes (up to 4 $\mathrm{W/cm^2}$ per chip), the driving potential of R236fa was higher than for the other refrigerants, because of its larger liquid density and lower two-phase density, causing its mass flow rate to be the highest. On the other hand, for higher heat fluxes, the friction forces increase significantly and for fluids with a larger density ratio (ρ_l/ρ_v), the mass flow rate drops faster, which is the case for R236fa, followed by R1234ze. Refrigerant R134a was the only one shown to be able to cool up to 7 $\mathrm{W/cm^2}$ which is the thermal design power for this application.

The predicted wall temperatures of the cold plate and the working fluid mass flow rate of the thermosyphon system proposed by Marcinichen et al. (2017), operating with R134a, R245fa, and R1234ze, were compared for the same input conditions. The system's architecture included an air-cooled condenser for this analysis. Refrigerant R134a had the lowest cold plate wall temperatures throughout the entire range of heat loads, which may be a result of its higher thermal conductivity resulting in higher heat transfer coefficients. Still, all fluids were able to keep the cold plate wall temperatures below 40 ºC, which is much lower than the limit of 85°C. It also displayed the highest mass flow rate, followed by R1234ze and, lastly, R245fa, except for low rates of heat loads of about 250 to 500 W, where R245fa had the highest mass flow rate. This same behavior was shown by Lamaison et al. (2016b) for refrigerant R236fa for low heat loads, where the low-pressure fluids seem to perform better. The higher mass flow rate of R134a at medium and high heat loads its due to lower pressure drops since it has a lower density difference between the liquid and vapor phases. It is also important to note that refrigerants

R134a and R1234ze operated under the gravity dominant regime throughout the entire range of prescribed heat load, unlike R245fa, which was shown to have reached its maximum mass flow rate at about 1000 W, and then entered in the frictional dominant regime.

2.1.1.5 Liquid accumulator

The addition of a liquid accumulator downstream the condenser is also a common architecture of the thermosyphon system (Figure 2.4). The role of the accumulator is to passively store and release refrigerant as a function of the input heat load. Without the liquid accumulator, for a high filling ratio and high heat load, the liquid could accumulate in the condenser leading to condenser flooding. And for a low filling ratio and low heat load, there may not be enough liquid height in the downcomer to drive the flow across the loop. Both extreme cases result in a lower system performance and are worrisome for practical application, so they should be avoided. The accumulator also guarantees that only subcooled liquid will flow through to the downcomer. So, with the addition of a liquid accumulator the thermosyphon loop system is assured to have a more stable and safe operation for a range of imposed heat loads (Lamaison et al., 2018).

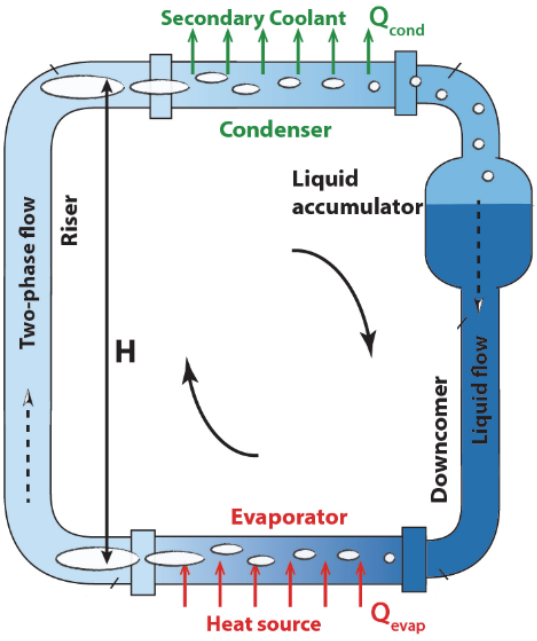

Figure 2.4 – Schematic of a thermosyphon loop with a liquid accumulator (Lamaison et al. 2018)

Lamaison et al. (2016b) also investigated the influence of the size of the liquid accumulator in the performance of the system, by testing volumes of 15, 45 and 80 cm^3, and finding that a bigger liquid accumulator, while maintaining the same volume of the rest of the loop, and the same height for the accumulator, reduced the system's mass flow rate. This is caused by the fact that when the heat flux is increased, the extra mass pushed into the accumulator is distributed over a larger volume, so the height of the downcomer is lower which leads to a lower driving potential for a larger accumulator.

2.1.2 Thermo-economic analysis

Szczukiewicz et al. (2015) added to the work of Marcinichen et al. (2014) by carrying out a thermo-economic analysis of a double thermosyphon loop system applied to a datacenter's rack for cooling. The proposed system is displayed in Figure 2.5. The authors evaluated the initial investment and operational costs of this new system and compared it to the standard air-cooled system. The payback period for one cabinet was estimated with and without heat recovery which consists of selling the hot water produced, to the District Heating Network, and since this selling value may vary, the authors estimated three prices, 30, 50, and 70 $/MWh. Results for a 90% server's fan reduction showed a payback period of 13.0, 10.9 and 9.4 months for the system with heat recovery, its period reducing with the increase of hot water price. For the system without heat recovery, the payback period was still 13.1 months. Another indicator used by authors to measure the viability of the system was the annual profit generated when substituting the current system for the proposed one. They found the following profit per year of $8647, $11116 and $13584, for respective water selling prices of 30, 50 and 70 $/MWh, and $6096 without heat recovery. The results of this thermo-economic study highlight that for an equipment life cycle of four years, the substitution for the double thermosyphon loop is not only viable but lucrative.

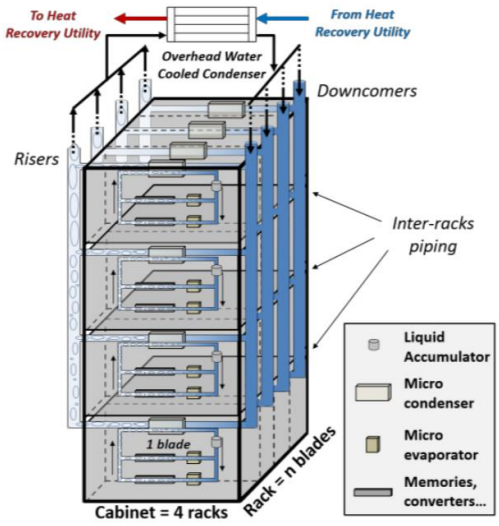

Figure 2.5 – Potential blade/cabinet architecture with double-thermosyphon on-chip cooling technology (Szczukiewicz et al., 2015)

2.1.3 Dynamic behavior investigation

When operating electronic equipment, one observes that it does not work releasing a heat load constant with time. Therefore, a model and experiment adapted to study the operation of the system under a transient regime are necessary. Hence, the importance of investigating the transient regime of thermosyphons, to understand how their variables respond over time, to a sudden change in an operating condition, sometimes referred to as a disturbance.

Marcinichen et al. (2014) developed a steady-state model for the thermosyphon loop but also modeled the evaporator for transient regime to study its dynamic behavior. Simulations for transient states for the micro-evaporator of a thermosyphon loop of 10 cm of height operating with R134a were performed. The heat flux was varied from 0 to 80 W/cm^2, representing the range of cold start to maximum heat load, and inlet pressure and subcooling were prescribed. Heat load disturbances and hot spots were simulated. After an initial step of 40 W/cm^2 for the heat flux, the system was shown to achieve a steady state in about 0.5 seconds.

After an increase of heat flux of 5 W/cm^2 to each of the two evaporators from Lamaison et al. (2016b), and before achieving the new steady state regime, the chip temperature rose as expected, and the mass flow rate of the system initially decreased because of the increase of vapor generated in both evaporators, causing extra friction in these components. However, after that, the mass flow rate starts to

rise as a result of higher vapor quality that has reached the riser and because of its lower density increases the driving potential in this component. The mass flow rate and chip temperature then converged, and another steady state was obtained in about 100 seconds. Another disturbance was carried out on the system, this time by increasing the mass flow rate of the water entering the condenser. The system responded by showing a rapid increase in mass flow rate which is a product of the extra accumulation of liquid at the condenser outlet, but as this extra liquid reaches the liquid accumulator, it increases the subcooling at the downcomer inlet, causing the vapor quality at the outlet of the evaporators to decrease, resulting in the opposite reaction observed in the first disturbance, leading to a decrease of mass flow rate. The chip temperature also dropped significantly. This study helped to better understand the complex nature of the thermosyphon performance after having suffered a disturbance on the system's conditions.

2.1.4 Experimental validation

To evaluate if the model can predict the thermosyphon loop behavior accurately, it is fundamental to validate the model with experimental data.

2.1.4.1 Steady state

For a thermosyphon of 15 cm of height operating with R134a, the model by Marcinichen et al. (2016) underpredicted the mean chip temperature by around 5%, which the authors noted is reasonable since the heat transfer correlations used ensures a predictability rate of around $\pm$20%. The model also overpredicted the approach temperature (temperature difference between inlet working fluid and outlet secondary fluid flow in the condenser) by about 4 K. The authors found that such discrepancy might be due to their assumption of an average value for the overall condenser thermal conductance and figured that a better model for the condenser conductance should result in a better agreement with experimental data.

Lamaison et al. (2016a) contrasted the experimental results from part 1 (Ong et al., 2016), with those of the numerical simulation for steady-state with heat fluxes ranging from 15.2 to 33.1 W/cm^2, there was an overprediction with a 2.9% error

for the mean chip temperature, and also an overprediction of 0.35 bar for the evaporating pressure, which the authors associated to an underprediction of the heat loss from all the piping.

The experimental validation carried out by Marcinichen et al. (2017) on the thermosyphon loop focused on validating parameters that differ from the usual one, which is the working fluid mass flow rate. They evaluated the mean thermal resistance of the system operating with the air-cooled condenser, as a function of the imposed heat load. An overprediction of 15% at most, for a maximum heat load of 1841 W was reported. The authors highlighted that this result was reasonable given the range of predictability of the two-phase heat transfer correlations, and model assumptions of no heat loss in the piping and condenser. They also mentioned that the error regarding the predictability seems to grow with the heat load, since for higher heat fluxes the heat losses are probably more significant, but also pointed out that the system is thermally insulated. As it is not within the scope of this project, the experimental validation on the pumped two-phase loop will not be detailed here. For the air-cooled condenser, a validation on the total pressure drop across the cold plate, as a function of the prescribed heat load, was also performed. Results showed that the pressure drop was overpredicted by the simulation, especially when the heat load was lower, as by increasing the heat load, the curves grew closer to each other indicating a better agreement. This error was justified by the authors on the total pressure drop being very low, and the differential pressure transducer accuracy could be influencing this result. Also, for this application, the correlations were reportedly extrapolated outside their optimum range, and this could be a point of improvement in the model. Finally, the thermosyphon loop operating with the ultra-compact liquid-cooled condenser was validated for the cold plate wall temperature as a function of the heat load. The wall temperature was slightly overpredicted throughout the whole range of heat loads, however for a heat load of 954 W a change on the temperature slope appears, and the error in predicting the cold plate wall temperature increases. This change of slope is characterized by the authors as a change in the flow pattern, possibly a transition from slug to annular flow. The model also had a change of slope, even though it appears that the predictability was not as accurate as for lower heat loads, perhaps pointing out that the model could be improved for different flow patterns.

While contrasting the mass flow rate as a function of heat load, obtained by the model of Ong et al. (2017) with their experimental data, it is evident that the model showed both gravitational and frictional dominant regimes across their whole heat load input range, as did the experimental campaign. However, the model was shown to overpredict the mass flow rate especially for lower heat fluxes (15 to 25 W/cm^2) which characterize the gravitational dominant regime. For higher heat fluxes (up to 40 W/cm^2), the model presented a much better agreement. It was also clear that the model achieved its maximum mass flow rate for a heat flux around 20 W/cm^2, while experimental results showed its peak value at 25 W/cm^2. The authors pointed out that this overprediction of mass flow rate may be due to an underprediction of the overall frictional and momentum pressure drops, as lower pressure drops signify lower flow resistances, that lead to a higher mass flow rate. They also highlighted that for this validation, the architecture of the system did not include the liquid accumulator to have enough subcooling and be able to apply their quasi non-intrusive method, to measure the mass flow rate experimentally. But because of that, the system was not able to dissipate more than 40 W/cm^2 of heat flux while for the system with the liquid accumulator heat fluxes of up to 70 W/cm^2 could be dissipated while keeping a chip temperature of 58°C. The authors also validated the model for mean chip temperature, with the inclusion of the liquid accumulator. A good agreement was obtained between the model and the experimental data while showing again a higher error for lower heat fluxes (15-35 W/cm^2), which is attributed to the accuracy of the two-phase flow boiling methods and the challenge to characterize heat losses at low heat fluxes. Still, the mean chip temperature was predicted with an error band of about 1 K.

As discussed previously in the parametric study section, Seuret et al. (2018) combined their experimental validation with a parametric investigation. Trends regarding the behavior of the system were detailed in that section, however here the accuracy of the model is highlighted. Their model predicted the same trends observed experimentally for the chip temperature, although the model underpredicted the temperatures, a mean average percentage error of 3.46% was found. The temperature variation of the water at the condenser was shown to be predicted with a 3.64% of error. Despite a small error of 1.9% over the thermal

resistance, the trend of reduced resistance for a higher heat load was not reproduced by the model.

2.1.4.2 Transient state

In addition to providing an experimental validation to their steady-state model, Lamaison et al. (2016a) also decided to investigate, by evaluating the transition period from steady states, if their code would be able to predict the complex dynamics of the system. Following a drop of heat flux of 33.1 to 29.4 W/cm^2, two variations with different time constants were observed for both the experimental and simulated data. The chip temperature first experiences a rapid, and then a slower decrease. The authors noted that the model predicted the first rapid decrease accurately in terms of amplitude and time constant, while for the slower variation, the simulation underpredicted the time constant of the experiment. The conclusions drawn from the authors were that the factors that led to this discrepancy were the non-consideration of thermal accumulation in the piping and condenser walls, the assumption of steady-state mass balance, and the underprediction of the dead space.

2.2 Experimental work

Franco and Filippeschi (2012) carried out an extensive literature review in experimental works of thermosyphon loop systems, with channels with diameters of the order of millimeters, and application for heat loads up to 1kW. According to the authors, results from different studies often showed disagreements with each other, showing that there is not a universal conclusion for connection between crucial parameters of the system dynamics, such as the relationship between applied heat load and working fluid mass flow rate. This implies the difficulty of a safe practical application of these systems since the heat load values, in practice, can vary considerably. The authors sought to carry out a critical analysis of the wide range of experimental results and were able to conclude that, in many studies, results could not be taken as trends for general cases, but were intrinsically linked to the respective system and application. Although many authors have investigated the effect of filling ratio or system instabilities, only a few authors have attempted

to study the connections between thermal performance and fluid dynamics. One could mention, the impact of the distance between evaporator and condenser, flow meter used, filling ratio, and combination of working fluid and diameter of channels in the mass flow rate. Another conclusion made by the authors was concerning the working fluid mass flow rate measurement, where the equipment used in particular, the Coriolis flowmeter, changed the relationship between the mass flow rate and heat load since it introduced flow resistance to the fluid dynamics. So, it is necessary to have a way of measuring, or rather predicting the mass flow rate, in a way that is not intrusive to the system. The authors then proposed a new architecture for the experimental apparatus, with three different ways to measure the mass flow of the system.

In the first part of a 4-part series study (Ong et al., 2016), the authors performed experiments with a mini-thermosyphon loop for cooling of a pseudo CPU package with heat fluxes of up to 61.4 W/cm^2. They investigated both steady and transient regime and experiments were made with and without the addition of a liquid accumulator. The experiments performed by Ong et al. (2016) showed that the architecture that does not include a liquid accumulator has limitations, as expected. For condenser water inlet temperatures above 20°C, or for mass water flow rates below 8 kg/h, the cooling in the condenser was insufficient, causing the two-phase flow to pass through to the downcomer and then to the evaporator. The authors noted that this resulted in fluctuations in the refrigerant pressure in the evaporator inlet and the temperature of the pseudo-chip. Therefore, for these conditions, the steady-state regime could not be achieved by the system. Tests showed that, for the thermosyphon system without the liquid accumulator, the mass flow rate started to drop when the heat fluxes were around 30 W/cm^2 and over, meaning the system was operating under the friction dominated regime which is undesirable and should be avoided to stay away from the critical heat flux. Contrarily, with the liquid accumulator the system was able to adjust its mass flow rate to suit higher heat fluxes, and its operation was stable for heat fluxes of up to 60.9 W/cm^2, while keeping the chip temperature lower than 58°C. The authors also compared the performance of the thermosyphon loop with that of a pumped loop. For this comparison, they evaluated the micro-evaporator thermal resistance for the system operating in thermosyphon and pump modes and found that the pumped loop with a refrigerant mass flow rate of 6 kg/h for heat fluxes from 30-50 W/cm^2

resulted in a comparable thermal resistance to the thermosyphon, whereas for a refrigerant mass flow rate of 4 kg/h, the pumped loop yielded a higher thermal resistance than the thermosyphon.

Cataldo and Thome (2019) studied experimentally a thermosyphon loop for cooling the transistor module of a transformer. They proposed a new loop architecture (Fig. 2.6), by adding a phase separator at the outlet of the evaporator, which recirculates the liquid back into the evaporator inlet, while the vapor goes up in the riser.

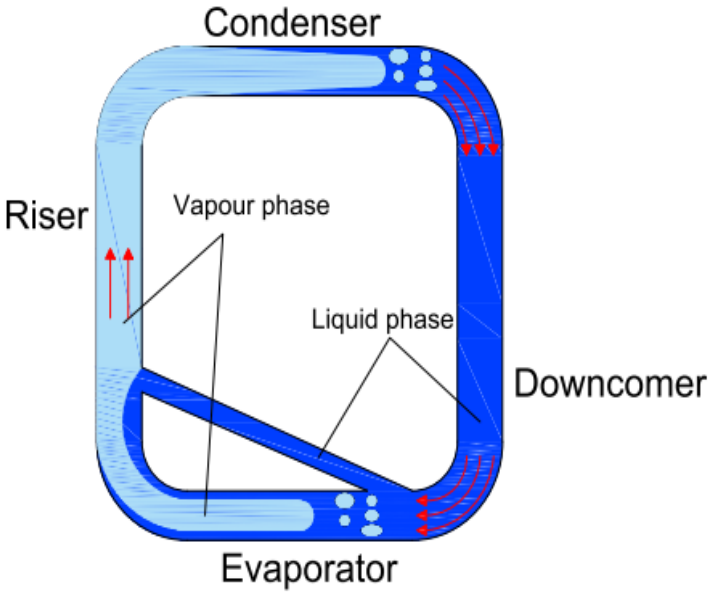

Figure 2.6 – Thermosyphon loop with the addition of a phase separator proposed by Cataldo and Thome (2019)

The new bypass recirculation loop provides a lower pressure drop in the riser, resulting in a higher mass flow rate for the system. However, the refrigerant charge required to avoid flow instabilities is also higher. The authors investigated both the standard configuration and the bypass one for R1234ze and R1234yf as working fluids, to evaluate if the addition of the phase separator was beneficial to the performance of the system. They found that the inclusion of the phase separator for refrigerant R1234ze ensured a safer operation without flow instabilities and yielded better performance. Despite guaranteeing a more desirable operation for R1234ze, the recirculation loop operating with R1234yf showed only a slight increase in mass flow rate and an increase in the overall thermal resistance, resulting in a lower thermal performance than the standard loop with the same prescribed

heat load. Finally, the authors concluded that the recirculation loop benefits low-pressure fluids, while it is not an optimal choice for higher pressure fluids.

2.3 Summary and present study

From the literature review, it was possible to conclude that a great deal of investigation on the two-phase thermosyphon loop operating with refrigerant R134a has been made. Other refrigerants have also been investigated although, R134a still provided the best overall performance for medium to high heat fluxes. Nevertheless, as mentioned previously, R134a has a high GWP of 1430, and because of it, is characterized as environmentally unfriendly. Therefore, its application in an upcoming thermosyphon loop system is impracticable.

Consequently, alternatives to R134a with low GWP that are also capable of providing an equivalent thermal performance must be considered. HFOs R1234ze (GWP<1) and R1234yf (GWP<1) have been appointed as alternatives to R134a due to their similar thermodynamic properties and low GWPs. However, as shown by Cataldo and Thome (2019) R1234yf is a better alternative than R1234ze for the standard configuration of the two-phase thermosyphon loop.

Table 2.1 exhibits the thermodynamic properties of refrigerants R134a and R1234yf.

Table 2.1 – Thermodynamic properties comparison between R134a and R1234yf (Reasor et al., 2010)

Thermodynamic Property	**R134a**	**R1234yf**
Chemical Formula	CF_3CH_2F	$C_3F_4H_2$
Molar Mass (kg/kmol)	102.03	114.04
Boiling Point at 1atm (K)	247.08	243.70
Freezing Point (K)	169.85	unknown
Critical Temperature (K)	374.21	367.85
Critical Pressure (MPa)	4.06	3.38
Critical Density (kg/m^3)	511.90	478.01

Figure 2.7 illustrates the saturation densities of both R134a and R1234yf.

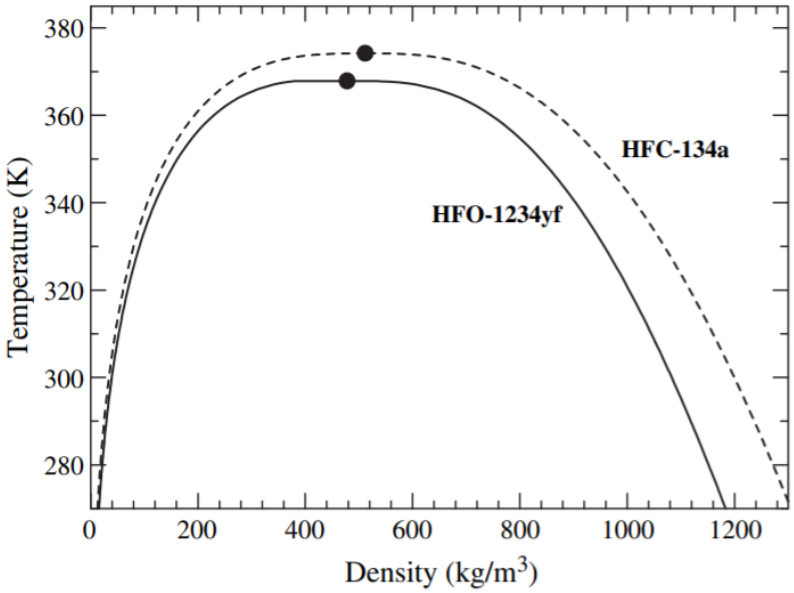

Figure 2.7 - Comparison of the saturation densities of R134a and R1234yf (Tanaka and Higashi, 2010)

Table 2.1 and Figure 2.7 show that the thermodynamic properties of refrigerant R1234yf and R134a are quite close in value, with R1234yf having slightly lower critical properties, which indicate that a system with R1234yf is expected to operate under lower pressures, temperatures and densities, than when working with R134a.

The literature survey also pointed to a lack of numerical studies on two-phase thermosyphon loops for electronic cooling operating with refrigerant R1234yf. Therefore, this study proposes to develop a steady-state numerical model for the standard no-accumulator two-phase thermosyphon loop operating with R1234yf, so as to provide a first performance study.

Finally, Table 2.2 presents a summary of the reviewed numerical models, which also illustrates their model assumptions, two-phase flow model, working and secondary fluids, and imposed heat load or heat flux.

Table 2.2 – Summary of works on two-phase thermosyphon loop modeling for electronic cooling

Authors, year	Modeling Regime	Two-phase flow model	Liquid Accumulator?	Working Fluid	Secondary Fluid	Heat Load /Heat Flux	Parametric Study?	Experimental Validation?
Seuret et al., 2018	Steady-state	Homogeneous	No	R236fa	Water	20-60 W	Yes	Yes
Ong et al., 2017	Transient	Homogeneous	Yes	R134a	Water	34-158 W/ 15-70 W/cm^2	Yes* experimental parametric study	Yes
Marcinichen et al., 2017	Transient	Homogeneous	No	**R134a/** R1234aze/ R245fa	Air/ Refrigerant	311-1841W	Yes	Yes
Lamaison et al., 2016a	Transient	Homogeneous	Yes	R134a	Water	34.5-75.9 W	No	Yes
Lamaison et al., 2016b	Transient	Homogeneous	Yes	R134a	Water	10-80 W for each evaporator	Yes	Yes* The model was already validated by Lamaison et al. (2016a)
Szczukiewicz et al., 2015	Steady-state	Homogeneous	No	R134a	Water	14.08 kW	Yes* the same parametric study as the one presented by Marcinichen et al. 2014	No

Marcinichen et al., 2014	Steady-state plus transient modeling of the evaporator	Homogeneous	No	**R134a**/ R1234ze	Water	0-200 W / 0 - 80 W/cm^2	Yes	No
Agostini et al., 2014	Steady-state	Homogeneous	No	R245fa	Air	200 - 1000 W	No	Yes
Bieliński and Mikielewic, 2010	Steady-state	Separated	No	R11	?	0- 2000 W	No	No

Table 2.2 – Summary of works on two-phase thermosyphon loop modeling for electronic cooling (continuation)

Authors, year	Model Assumptions
Seuret et al., 2018	Two-phase flow is modeled using a plug flow model with both phases in thermodynamic equilibrium; adiabatic piping; 2-D steady-state conduction in the evaporator package; Considers the maximum temperature at the chip layer as the chip temperature
Ong et al., 2017	Same model as the one presented by Lamaison et al. (2016a)
Marcinichen et al., 2017	Two-phase flow is modeled using a plug flow model; a constant and uniform heat load is imposed on the cold plate; there is uniform flow distribution within the cold plate; no heat loss on the piping and condenser
Marcinichen et al., 2016	Steady-state flow and cooling, adiabatic piping, a constant and uniform heat load on the ME (no hot-spot), uniform flow distribution within the evaporator, and 2D conduction in the evaporator. Assumed an average overall conductance for the condenser based on experimental results
Lamaison et al., 2016a	Two-phase flow modeled with a homogeneous plug flow model; steady-state momentum balance neglecting the accumulation term since the pressure gradient exhibits a very fast dynamic; considers the mass flow rate at each time step, the same for all cells; 2D dynamic conduction in the evaporator; heat loss in the piping; lumped capacitance model for the liquid accumulator
Lamaison et al., 2016b	The same modeling assumptions as Lamaison et al., (2016a) but applied to the cooling of a 2U server (2 evaporators), plus the addition of a microchannel condenser instead of the tube-in-tube one.
Szczukiewicz et al., 2015	Adiabatic piping, a constant and uniform heat load on the evaporator (no hot spot), uniform flow distribution within the evaporator, and 2D conduction in the evaporator
Marcinichen et al., 2014	Steady state simulation, adiabatic piping; uniform heat load (no hot spot), and flow distribution within the evaporator; Plus, for the evaporator: Transient 1-D energy balance, steady-state momentum balance and transient two-dimensional conduction scheme in the package are solved (considering thus thermal storage)
Agostini et al., 2014	A 1-D numerical model. Energy transfer occurs only in the evaporator and condenser sections. Same fluid for both loops. All the heat is transferred from loop 1 to loop 2
Bieliński and Mikielewic, 2010	A 1-D numerical model. Riser and downcomer are adiabatic. Thermosyphon loop with minichannels (constant cross-section area); heated at the bottom horizontal side and bottom vertical side, and cooled at the upper vertical side

3 Mathematical model

3.1 Description of the cooling system

As described in Chapter 1, this dissertation provides a numerical model for a thermosyphon loop system for on-chip cooling. This modeling effort will follow the traditional architecture of the thermosyphon loops, having a condenser followed by a falling tube named a downcomer, which leads to an evaporator whose outlet is connected to a two-phase rising tube called a riser, that returns the flow back into the condenser, closing the loop.

3.2 Modeling assumptions

The mathematical model will mostly follow the one-dimensional steady-state model presented by Seuret et al. (2018). Therefore, the thermosyphon will be modeled for steady-state regime, with its two-phase flow considered as homogeneous flow because of its simplicity and relatively good performance, and with both phases considered in thermodynamic equilibrium.

In the homogeneous flow model, the two phases are assumed to be well mixed and thus, with the same velocity. Essentially, it reduces the two-phase flow to a highly compressible single-phase flow, and this allows to use the same set of conservative equations for both single and two-phase flow. According to Agostini and Yesin (2008), the homogeneous flow model can be assumed for small diameter thermosyphons since the coupling between vapor and liquid is expected to be total, and the homogeneous model was shown to adequately predict the pressure drop in small channels, as in Ribatski et al. (2006), and Agostini and Bontemps (2005)

The two-phase properties are calculated using Equations (3.1) to (3.3) by Cicchitti et al. (1959) and as mentioned previously can be used for single and two-phase flow. With these equations, the void fraction ε (-), velocity u (m/s), and the density of the mixture ρ_{lv} (kg/m^3) are obtained, respectively.

$$\varepsilon = \frac{x\rho_l}{(1-x)\rho_v + x\rho_l} \tag{3.1}$$

$$u_l = u_v = u = \frac{x\dot{m}}{\rho_v S\varepsilon} \tag{3.2}$$

$$\rho_{lv} = \varepsilon\rho_v + (1-\varepsilon)\rho_l = \left(\frac{x}{\rho_v} + \frac{(1-x)}{\rho_l}\right)^{-1} \tag{3.3}$$

In Eq. (3.1) the void fraction is obtained as a function of the vapor quality (-), and the densities of the liquid ρ_l and vapor phases ρ_v (kg/m^3). The velocity of the fluid is calculated (Eq. 3.2) with its mass flow rate (m/s), the cross-sectional area of the channel (m^2), its vapor quality, vapor density and void fraction. And the density of the liquid-vapor mixture, is given with the vapor quality of the fluid and its liquid and vapor densities.

The dynamic viscosity of the mixture μ_{lv} $(Pa.s)$ is obtained by the empirical model presented by Beattie and Whalley (1982) .

$$\mu_{lv} = \mu_l(1-\varepsilon)(1+2.5) + \mu_v\varepsilon \tag{3.4}$$

Plug flow is assumed for the entire system, and for this model, there is no velocity gradient in the radial direction which means that there is complete mixing radially. Therefore, the plug flow model considers no mixing in the axial direction.

Considering one dimensional (z-direction) steady-state flow, the set of conservative equations derived from Navier-Stokes, and simplified for this application, of mass, momentum, and energy, are as follow respectively:

$$\frac{\partial(\rho u)}{\partial z} = 0 \tag{3.5}$$

$$\underbrace{\frac{\partial P}{\partial z}}_{total} = \underbrace{-\frac{\partial(\rho u^2)}{\partial z}}_{acceleration} \underbrace{-\left(\frac{\partial P}{\partial z}\right)_{fr}}_{friction} \underbrace{-g\rho\sin\theta}_{static} \tag{3.6}$$

$$\underbrace{\rho u \frac{\partial h}{\partial z}}_{convection} + \underbrace{\frac{1}{2}\frac{\partial(\rho u^3)}{\partial z}}_{kinetic\ energy} = \underbrace{u\left(\frac{\partial P}{\partial z}\right)_{fr}}_{viscous\ heating} + \underbrace{\frac{q"S}{V}}_{\substack{heat\ source \\ from\ the \\ perimeter}} - \underbrace{\rho g \sin\theta\, u}_{potential\ energy} \quad (3.7)$$

where θ represents the angle between the flow and horizontal direction, $q"$ the heat flux received, and S and V the cross-sectional area and volume of the component evaluated. Also, the pressure drop due to friction is determined via empirical correlations that will be later detailed.

Equations (3.5) to (3.7) are displayed in their generalized model but are later detailed and adapted for each of the thermosyphon's components.

Two-dimensional heat conduction is assumed for the micro-evaporator package. With this assumption not only uniform heat fluxes can be simulated but also row hot spots which are local higher heat flux zones perpendicular to the flow direction. Also, for when investigating transient regime, the two-dimensional heat conduction model considers thermal storage.

In summary, the main assumptions are:

- One dimensional flow throughout the loop
- Homogeneous two-phase flow model
- Phases in thermodynamic equilibrium
- Steady-state regime
- Plug flow in the whole system (no axial mixing)
- Implicit continuity equation
- Uniform flow through the microchannels
- Two-dimensional heat conduction in the heat sink package
- Adiabatic piping

The thermophysical properties of the working fluid are obtained locally based on the enthalpy and pressure of the working fluid, using a REFPROP (9.1 version) routine for Matlab (R2020a version).

3.3 Micro evaporator

As Figure 3.1 shows, the micro-evaporator is a microchannels heat exchanger attached to a heat sink package. This heat sink package is composed of a cold plate and thermal interface material that connects the micro-cooling element (cold plate) to the electronic chip. The chip will be simulated as a layer of the heat sink package assumed to be silicon. Figure 3.1 also highlights the heat transfer at the fin level.

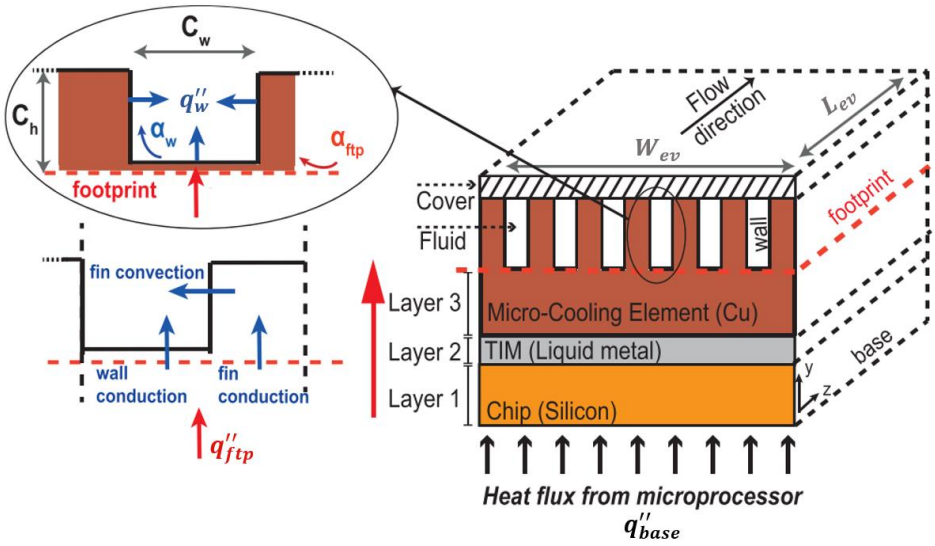

Figure 3.1 – Micro-evaporator model (Lamaison, 2014)

The heat transfer and fin equations for the micro-evaporator (Eqs. (3.8) to (3.12)) are solved iteratively and locally since the wall heat transfer coefficient for two-phase flow given by the model of Costa-Patry and Thome (2013), detailed in a further section, depends on the wall heat flux. This iteration process is solved by an algorithm that implements the Steffensen method which will be discussed in chapter 4.

$$q''_w = \alpha_w \left(T_{ftp} - T_f\right) \tag{3.8}$$

$$m = \sqrt{2\alpha_w \frac{W_f + L_{ev}}{\lambda_{ev}\, L_{ev}\, W_f}} \tag{3.9}$$

$$\eta_f = \frac{\tanh(mH_{ch})}{mH_{ch}} \tag{3.10}$$

$$q''_{ftp} = q''_w \frac{N_{ch}\left(W_{ch} + 2H_{ch}\,\eta_f\right)}{W_{ev}} \tag{3.11}$$

$$\alpha_{ftp} = \frac{q''_{ftp}\alpha_w}{q''_w} \tag{3.12}$$

The footprint heat flux q''_{ftp} and heat transfer coefficient α_{ftp}, both consider conduction and convection in the fins, plus the convection from the prime surface at the base of the channels, called footprint level as highlighted in Figure 3.1.

The temperatures at the footprint T_{ftp} are obtained by solving the two-dimensional steady-state conduction (Eq. (3.13)) in the heat sink package for position $y = ftp$ and position z varying from the inlet to the outlet of the channel.

Solving the two-dimensional conduction also provides the temperature of the chip, which is an output of the model, and of extreme importance since the system intends on maintaining the temperature of the chip below the limit of 85 ℃ or any other project limit.

$$0 = \frac{\lambda}{\rho c_p}\left(\frac{\partial^2 T}{\partial z^2} + \frac{\partial^2 T}{\partial y^2}\right) \tag{3.13}$$

3.3.1 Single-phase flow

The flow is expected to enter the microchannel in a subcooled liquid state or as a saturated liquid. Therefore, for as long as the flow is characterized as single-phase, proper correlations for single-phase flow in microchannels are necessary to determine its pressure drops and heat transfer.

The geometrical parameters such as the hydraulic diameter and aspect ratio for each non-circular microchannel are given respectively, by Equations (3.14) and (3.15).

$$d_h = \frac{4W_{ch}H_{ch}}{2(W_{ch} + H_{ch})} \tag{3.14}$$

$$asp = \frac{W_{ch}}{H_{ch}} \tag{3.15}$$

$$Re_{dh} = \frac{\rho_{lv} u d_h}{\mu_{lv}} \tag{3.16}$$

3.3.1.1 Laminar developing flow

In microchannel compact heat exchangers, single-phase flow usually presents in the range of laminar flow regime because of its small flow channels. In this work, the flow is considered laminar when the Reynolds number based on the hydraulic diameter (Eq. (3.16)), is lower than 2300. For the laminar regime, the flow is also considered as developing flow, and the following models are applied for friction pressure drop and heat transfer coefficient.

To determine the pressure drop in the hydrodynamic entry region, Equation (3.17) shows the incremental pressure drop between the entrance (position 0) and the position of concern:

$$\left.\frac{dP}{dz}\right|_{fr}^{0\to l} = \frac{2G^2 f_{app,l}}{\rho_l d_h} \tag{3.17}$$

And Equation (3.18) gives the pressure drop between a general position l and its following position:

$$\left.\frac{dP}{dz}\right|_{fr}^{l\to l+1} = \frac{2G^2}{d_h}\left[(l+1)\frac{f_{app,l+1}}{\rho_{l+1}} - l\frac{f_{app,l}}{\rho_l}\right] \tag{3.18}$$

Where the apparent Fanning friction factor f_{app}, is obtained from the model by Muzychka and Yovanovich (2009) and is a function of the square root of the channel's cross-sectional area $\sqrt{S}$.

$$f_{app} = \frac{1}{Re_{\sqrt{S}}}\left[\left(\frac{3.44}{\sqrt{z^+}}\right)^2 + \left(\frac{12}{\sqrt{asp}(1+asp)\left(1-\frac{192asp}{\pi^5}tanh\left(\frac{\pi}{2asp}\right)\right)}\right)^2\right]^{0.5} \quad (3.19)$$

With:

$$z = (l-1)\Delta z + \frac{\Delta z}{2} \quad (3.20)$$

$$z^+ = \frac{z}{\sqrt{S}Re_{\sqrt{S}}} \quad (3.21)$$

$$0 \leq asp \leq 1 \quad (3.22)$$

Where Δz is the length of a discretized element and l stands for the number of the discretized element being evaluated.

The Nusselt number in the hydrodynamic and thermal entry region, for laminar single-phase flow, through non-circular channels is given by the correlation of Muzychka and Yovanovich (2004).

$$Nu_{\sqrt{S}} = \left[\left(\frac{C_4 f(Pr)}{\sqrt{z^*}}\right)^m + \left(\left(C_2C_3\left(\frac{fRe_{\sqrt{S}}}{z^*}\right)^{1/3}\right)^5 + \left(C_1\left(\frac{fRe_{\sqrt{S}}}{8\sqrt{\pi}aspy\gamma^\gamma}\right)\right)^5\right)^{m/5}\right]^{1/m} \quad (3.23)$$

$$\begin{cases} z^* = \dfrac{z}{\sqrt{S}Re_{\sqrt{S}}} \\ C_1 = 3.86 \\ C_2 = 1 \\ C_3 = 0.501 \\ C_4 = 1 \\ f(Pr) = \dfrac{0.886}{[1+(1.909Pr^{1/6})^{9/2}]^{2/9}} \;\; with \;\; Pr = \dfrac{\mu c_p}{\lambda} \\ m = 2.27 + 1.65Pr^{1/3} \\ fRe_{\sqrt{S}} = \dfrac{12}{\sqrt{asp}(1+asp)\left[1 - \dfrac{192asp}{\pi^5}tanh\left(\dfrac{\pi}{2asp}\right)\right]} \\ \gamma = 0.1 \end{cases} \tag{3.24}$$

Finally, Equation (3.25) determines the heat transfer coefficient for the single-phase developing laminar flow.

$$\alpha = \frac{\lambda Nu_{\sqrt{S}}}{\sqrt{S}} \tag{3.25}$$

3.3.1.2 Turbulent flow

The flow is considered turbulent when the Reynolds number based on the hydraulic (Re_{dh}) diameter is above 2300. And for this, the friction factor is calculated with the correlation of Petukhov (1970) shown in Equation (3.26).

$$f = \frac{1}{4}(1.82\log_{10}(Re_{dh}) - 1.64)^{-2} \tag{3.26}$$

And the pressure drop is obtained with Eq. (3.27).

$$\left.\frac{dP}{dz}\right|_{fric} = \frac{2fG^2}{\rho d_h} \tag{3.27}$$

Then, the Nusselt number is determined by the correlation of Gnielinksi (1976), which is applied to Equation (3.28) to obtain the heat transfer coefficient for single-phase turbulent flow.

$$Nu = \frac{(f/2)(Re_{dh} - 1000)Pr}{1 + 12.7\sqrt{f/2}\ (Pr^{2/3} - 1)} \tag{3.28}$$

3.3.2 Boiling flow

3.3.2.1 Frictional pressure drop

The frictional pressure drop by Müller-Steinhagen and Heck (1986) presents an asymptotic fit based on the single-phase liquid and vapor frictional pressure drops, as follows:

$$\left.\frac{dP}{dz}\right|_{fr} = H(1-x)^{1/3} + Bx^3 \tag{3.29}$$

With:

$$\begin{cases} H = A + 2(B - A)x \\ A = \left.\dfrac{dP}{dz}\right|_{fr,l} \\ B = \left.\dfrac{dP}{dz}\right|_{fr,v} \\ Re_l = \dfrac{Gd_h}{\mu_l} \\ Re_v = \dfrac{Gd_h}{\mu_v} \end{cases} \tag{3.30}$$

Where the liquid and vapor frictional pressure drops, represented by coefficients A and B respectively, are determined by the models of Muzychka and Yovanovich (2009) for laminar, and Petukhov (1970) for turbulent flow.

3.3.2.2 Heat transfer model

Figure 3.2 illustrates the flow patterns present for evaporation of the fluid in a horizontal microchannel.

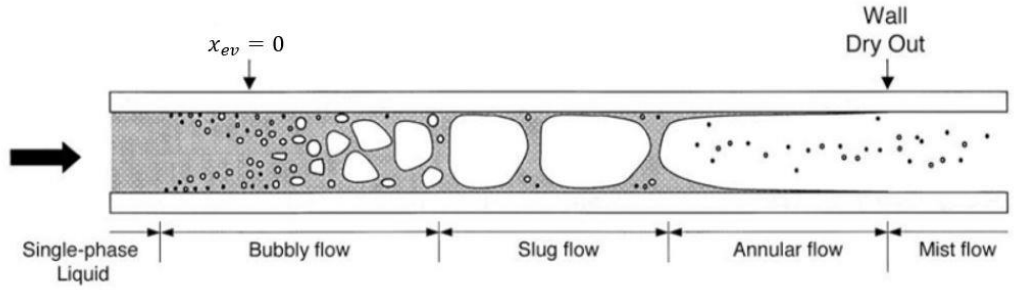

Figure 3.2 – Evaporation flow patterns in a horizontal microchannel
(Lee and Mudawar, 2009)

The heat transfer coefficient for boiling flow α_w, is determined by the combination of the model by Costa-Patry and Thome (2013) and the model by Magnini and Thome (2017).

Costa-Patry and Thome (2013) developed a new flow pattern-based prediction method, for heat transfer coefficients for two-phase boiling in microchannel evaporators from experimental results. They provided modifications for the three-zone flow boiling model of Thome et al. (2004) and adapted the annular flow model for convective boiling from Cioncolini and Thome (2011), for circular to non-circular microchannels.

Equation (3.32) provides a weighted linear proration between the three-zones slug flow model and the annular flow model, which gives the wall heat transfer coefficient for flow boiling.

$$x_{CB-AF} = 425\left(\frac{\rho_v}{\rho_l}\right)^{0.1} \frac{B_l^{1.1}}{Co^{0.5}} \tag{3.31}$$

$$\alpha_w = \frac{(1-r)\alpha_{3Z}^2 + r\alpha_{AF}^2}{r\alpha_{AF} + (1-r)\alpha_{3Z}} \tag{3.32}$$

The model quantifies the vapor quality transition, from coalescing bubble regime to annular flow x_{CB-AF}, and evaluates if the transition model should be

applied based on a vapor quality transition range $x_{tr,range}$. Then, a linear proration factor r that varies between 0 and 1 is implemented to determine the heat transfer coefficient.

$$x_{tr,range} = x_{CB-AF} \pm \frac{x_{exit}}{5} \tag{3.33}$$

$$r = \frac{x - x_{CB-AF}}{0.4x_{exit}} + 0.5 \tag{3.34}$$

Thome et al. (2004) first introduced the three-zone heat transfer model for slug flow boiling in microchannels. The three zones are namely, a liquid slug, an elongated bubble with an evaporating thin film, and a dry-out zone.

Figure 3.3 provides a schematic of the three-zones. Where L_p is the total length of the pair or triplet, L_l the length of the liquid slug, and L_v the length of the bubble including the vapor slug with a dry wall zone L_{dry}, and with L_{film} as the length of the liquid film trapped by the bubble. Finally, δ_0 and δ_{min} are the thicknesses of the liquid film trapped between the elongated bubble and the channel wall at its formation and at dry out, respectively.

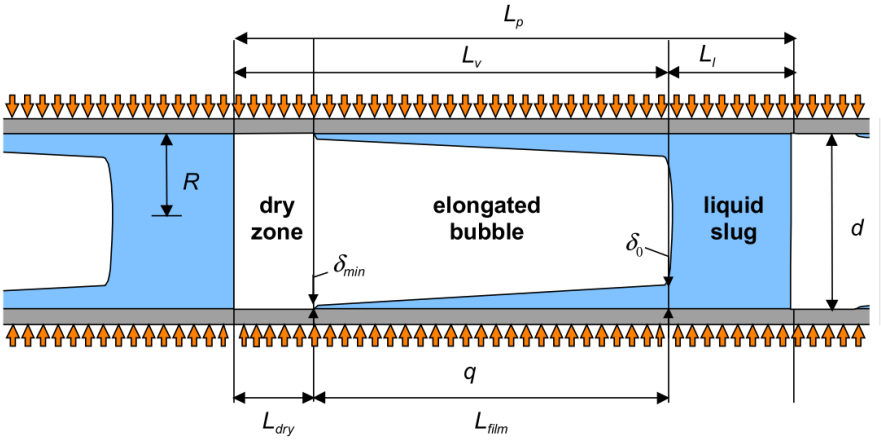

Figure 3.3 – Schematic of the three-zone model of Thome et al. (2004)

The authors described the process for a fixed location, as following the passing of a liquid slug, an elongated bubble passes, and if the thin evaporating film of the bubble dries out before the arrival of the next liquid slug, then a vapor slug passes. Therefore, either a liquid slug and elongated bubble pair (two-zones) or a

liquid slug, elongated bubble, and vapor slug triplet (three-zones) pass this fixed point at a designated frequency.

The heat transfer coefficient for the three-zone model is given as a function of the bubble frequency fr and the sum of each zone's product of residence time and heat transfer coefficient.

$$\alpha_{3Z} = fr(t_l\alpha_l + t_{film}\alpha_{film} + t_{dry}\alpha_v) \tag{3.35}$$

With the model assuming developed flow, Eq. (3.36) from Costa-Patry and Thome (2013) provide the heat transfer coefficient for the liquid and vapor slug zones, with subscript ph referring to either liquid or vapor.

$$\begin{cases} \alpha_{ph} = \dfrac{\lambda_{ph}}{d_{heat}}\left(Nu_{ph,lam}^4 + Nu_{ph,turb}^4\right)^{1/4} \\ d_{heat} = \dfrac{4W_{ch}H_{ch}}{W_{ch} + 2H_{ch}} \\ Nu_{ph,lam} = 4.36 \\ Nu_{ph,turb} = \dfrac{(f/2)/\left(Re_{dh,ph} - 1000\right)Pr_{ph}}{1 + 12.7\sqrt{f/2}\ \left({Pr_{ph}}^{2/3} - 1\right)} \end{cases} \tag{3.36}$$

The liquid slug and vapor slug residence times are calculated as follows:

$$\begin{cases} t_l = \dfrac{1}{fr\left(1 + \dfrac{\rho_l x}{\rho_v(1-x)}\right)} \\ t_v = \dfrac{1}{fr\left(1 + \dfrac{\rho_v(1-x)}{\rho_l x}\right)} \end{cases} \tag{3.37}$$

Magnini and Thome (2017) proposed to update the three-zone heat transfer model, by developing new prediction methods for determining the elongated bubble nose velocity, the initial liquid film thickness, and the bubble frequency for slug flow in microchannels.

The elongated bubble nose velocity is modeled assuming slip flow. The bubble nose velocity at its departure is given by Equation (3.38) from Goldsmith and Mason (1963).

$$u_{v,0} = \frac{u_{l,0}}{\left(1 - 2\delta_{N,0}/d_h\right)^2} \tag{3.38}$$

Where, $u_{l,0}$ is the liquid velocity at the bubble departure, given by Equation (3.39).

$$u_{l,0} = \frac{G}{\rho_l} \tag{3.39}$$

There are few correlations for the liquid film thickness for rectangular microchannels and their formulation is overly complex. Therefore, the correlations presented in Magnini and Thome (2017) for circular microchannels, will be adapted in this work for rectangular microchannels, by substituting the circular diameter with an equivalent diameter. This way, the film is redistributed to the rectangular perimeter keeping the same area proportion between the shapes. This adaptation was first reported by Costa-Patry and Thome (2013) for annular flow.

The initial liquid film thickness at the bubble nose is calculated with the correlation for steady moving bubbles proposed by Han and Shikazono (2009) (Eq. (3.40)) with the substitution of the diameter D for circular microchannels, for an equivalent diameter d_{eq} (Eq.(3.41)), for rectangular channels.

$$\frac{\delta_{N,0}}{D} = \frac{0.67Ca^{2/3}}{1 + 3.13Ca^{2/3} + 0.504Ca^{0.672}Re^{0.589} - 0.352(CaRe)^{0.629}} \tag{3.40}$$

$$d_{eq} = \sqrt{\frac{4W_{ch}H_{ch}}{\pi}} \tag{3.41}$$

From now on the next correlations that pertained to the circular microchannels with diameter D, will be shown as a function of the equivalent diameter as computed by this model.

For this correlation, the Reynolds and capillary numbers are computed with the elongated bubble velocity as Equations (3.42) and (3.43) point out.

$$Re_0 = \frac{\rho_l u_{v,0} d_h}{\mu_l} \tag{3.42}$$

$$Ca_0 = \frac{\mu_l u_{v,0}}{\sigma} \tag{3.43}$$

Valid for laminar flow condition of $Re_0 \leq 2000$, Equations (3.38) to (3.43) must be solved iteratively to obtain $u_{v,0}$. As an initial guess $u_{l,0}$ can be used to estimate an initial value of Re, Ca, and then $\delta_{N,0}$ for Equation (3.38) to obtain $u_{v,0}$. And then the iterative procedure restarts by correcting $\delta_{N,0}$ by means of Equation (3.40).

For Reynolds numbers over 2000, $Re = 2000$ is assumed, and the capillary number is replaced with:

$$Ca_0 = \frac{2000\mu_l}{\rho_l \sigma d_h} \tag{3.44}$$

Equation (3.45) gives the bubble nose velocity as a function of the initial bubble nose velocity.

$$u_v = u_{v,0} + \frac{Gx}{\rho_v} \tag{3.45}$$

The correlation by Han and Shikazono (2010) (Eq.(3.46)) gives the liquid film thickness as a function of the capillary number and bubble acceleration Bond number.

$$\frac{\delta_N}{d_{eq}} = \frac{0.968 Ca^{2/3} Bo_a^{-0.414}}{1 + 4.838 Ca^{2/3} Bo_a^{-0.414}} \tag{3.46}$$

Where Bo_a is the bubble acceleration Bond number and is calculated as:

$$Bo_a = \frac{\rho_l A_v d_h^2}{\sigma} \tag{3.47}$$

Using the local bubble nose velocity u_v, the bubble nose acceleration is estimated by:

$$A_v = \frac{4q''}{\rho_v h_{lv} d_h}\left[\frac{\left(u_v - u_{v,0}\right)}{ln\left(1 + Gx/\rho_v u_{v,0}\right)}\right] \tag{3.48}$$

Equation (3.49) gives the viscous boundary layer thickness δ_{vbl}, in the proximity of the bubble nose by Aussillous and Quéré (2000). The authors concluded in their investigation that for isolated bubbles $(\delta_{vbl} > \delta_N)$, traditional methods such as Eq. (3.46) for predicting the liquid film thickness presented a good agreement with their experimental data, however for high values of bubble frequency which correspond to short liquid slugs, the viscous boundary layer limited the development of the liquid film around the bubble, and because of that, the liquid film thickness should be computed as $\delta_N = \delta_{vbl}$.

$$\frac{\delta_{vbl}}{D} = \left(\frac{L_l}{D}\frac{1}{Re}\right)^{1/2} \tag{3.49}$$

In summary, Magnini and Thome (2017) proposed that the minimum value obtained by Equations (3.40),(3.46), and (3.49) for δ_N, should be assumed as the liquid film thickness.

$$\frac{\delta_N}{d_{eq}} = \min\left(\text{Eqs.}\,(3.40, 3.46, 3.49)\right) \tag{3.50}$$

Magnini and Thome (2017) also provided an empirical correlation based on a dimensional analysis to determine the bubble frequency for boiling in microchannels:

$$f_r = 1849 Bl^{0.66} Re_l^{0.18} P_{red}^{1.56} (1 + 10x)^{-2.05} \tag{3.51}$$

With dimensionless numbers:

$$\begin{cases} P_{red} = \dfrac{\rho_l}{\rho_v} \\ Bl = \dfrac{q''}{Gh_{lv}} \\ Re_l = \dfrac{Gd_h}{\mu_l} \end{cases} \tag{3.52}$$

The time it takes for the liquid film to be depleted $t_{dryfilm}$, is given by Eq. (3.53) (Costa-Patry and Thome, 2013). Lamaison (2014) noted that when the wall roughness Ra is unknown, which is the case, the surface roughness should be set to 1μm.

$$\begin{cases} t_{dryfilm} = \dfrac{\rho_l h_{lv}}{q}(\delta_N - \delta_{min}) \\ \delta_{min} = Ra \end{cases} \tag{3.53}$$

The film thickness at the end of the elongated bubble δ_{end}, and the dry-out and elongated bubble residence time, respectively t_{dry} and t_{film}, are computed by Equations (3.54) and (3.55).

If $t_{dryfilm} > t_v$, the heat transfer model works in the two-zone configuration:

$$\begin{cases} \delta_{end} = \delta_N - \dfrac{q''_w}{\rho_l h_{lv}} t_v \\ t_{film} = t_v \\ t_{dry} = 0 \end{cases} \tag{3.54}$$

If $t_{dryfilm} < t_v$, the heat transfer works in the three-zone configuration:

$$\begin{cases} \delta_{end} = \delta_{min} \\ t_{film} = t_{dryfilm} \\ t_{dry} = t_v - t_{film} \end{cases} \tag{3.55}$$

Finally, the local film heat transfer coefficient is given by Costa-Patry and Thome (2013):

$$\alpha_{film} = \frac{\lambda_l}{\delta_N - \delta_{end} + 10^{-9}} ln\left(\frac{\delta_N}{\delta_{end}}\right) \tag{3.56}$$

As mentioned previously, Costa-Patry and Thome (2013) introduced the equivalent diameter d_{eq} to adapt the model for annular flow by Cioncolini and Thome (2011), to allow its application for non-circular microchannels. Equations (3.57) to (3.59) carry out this method to determine the heat transfer coefficient for annular flow.

$$\alpha_{AF} = Nu\frac{\lambda_l}{\delta_{film,eq}} \tag{3.57}$$

$$\delta_{film,eq} = \frac{A_{eq}}{Per} = \frac{\pi/4\left(d_{eq}^2 - \left(d_{eq} - 2th_{film}\right)^2\right)}{2(W_{ch} + H_{ch})} \tag{3.58}$$

$$th_{film} = T^+Y^* \tag{3.59}$$

With dimensionless numbers Nu, T^+, Re_{lf} (liquid film Reynolds number) and Y^*:

$$Nu = 0.0776(T^+)^{0.9}Pr_l^{0.52} \tag{3.60}$$

$$T^+ = \max\left(\sqrt{\frac{Re_{lf}}{2}}; 0.0165Re_{lf}\right) \tag{3.61}$$

$$Re_{lf} = \frac{(1-E)(1-x)Gd_{eq}}{\mu_l} \tag{3.62}$$

$$Y^* = \frac{\mu_l}{\sqrt{\rho_l\tau_w}} \tag{3.63}$$

The wall shear stress τ_w, and the vapor core velocity u_c, are given as follow:

$$\tau_w = 0.5f\rho_c u_c^2 \tag{3.64}$$

$$u_c = \frac{Gx}{\rho_v\varepsilon} \tag{3.65}$$

Cioncolini and Thome (2012b) provided a prediction method for the void fraction for shear-driven annular flow, where the effect of gravity on the flow is negligible:

For flow conditions according to Eq. (3.66).

$$\begin{cases} 0 < x < 1 \\ 10^{-3} < \rho_v \rho_l^{-1} < 1 \\ 0.7 < \varepsilon < 1 \end{cases} \tag{3.66}$$

Eq. (3.67) gives the new void fraction for annular flow.

$$\begin{cases} \varepsilon = \dfrac{\beta x^{\omega}}{1 + (a-1)^{\omega}} \\ \beta = -2.129 + 3.129(\rho_v \rho_l^{-1})^{-0.2186} \\ \omega = 0.3487 + 0.6513(\rho_v \rho_l^{-1})^{0.5150} \end{cases} \tag{3.67}$$

A correlation by Cioncolini and Thome (2012a) gives the liquid entrainment fraction for annular two-phase flow.

$$\rho_c = \frac{x + E(1-x)}{(x/\rho_v)\,((E(1-x/\rho_l)} \tag{3.68}$$

$$We_c = \frac{\rho_c J_v^2 d_{eq}}{\sigma} \tag{3.69}$$

$$E = (1 + 279.6 We_c^{-0.8395})^{2.209} \tag{3.70}$$

As depicted in Eq. (3.68), the core flow density ρ_c depends on the entrained liquid fraction E, so Equations (3.68) to (3.70) should be solved iteratively. However, the authors proposed using an explicit predictor-corrector scheme instead to simplify its application and minimize computational costs. Predictor-corrector

methods are explicit algorithms that function in two steps. In the first step, a rough approximation of the desired quantity is calculated. In this case, the core flow density is estimated to be approximately the vapor density ($\rho_c \approx \rho_v$), and with that, the preliminary value of the Weber number We_c^p, and liquid entrainment fraction E^p, are obtained. Then, the corrector step refines the initial approximation computing a new value for ρ_c as function of E^p, We_c, and E, respectively.

$$\rho_c \approx \rho_v \tag{3.71}$$

$$J_v = \frac{xG}{\rho_v} \tag{3.72}$$

$$We_c^p = \frac{\rho_v J_v^2 d_{eq}}{\sigma} \tag{3.73}$$

$$E^p = \left(1 + 279.6 We_c^{p\,-0.8395}\right)^{2.209} \tag{3.74}$$

Lastly, the friction factor f is computed with Eq.(3.76) (Cioncolini et al., 2009) that was modified by Lamaison (2014), by the author adding the term $(1 + x^{0.8})$ to counter-balance unrealistic behaviors by the model at high vapor qualities.

$$Bo = \frac{g(\rho_l - \rho_v)d_h^2}{\sigma} \tag{3.75}$$

$$\begin{cases} f = 0.172 We_c^{-0.372} & if\ Bo > 4 \\ f = 0.0196 We_c^{-0.372} Re_{lf}^{0.318}(1 + x^{0.8}) & if Bo < 4 \end{cases} \tag{3.76}$$

3.3.2.3 Critical heat flux

The critical heat flux is computed with the empirical correlation for square multi-microchannels from Ong and Thome (2011).

$$\frac{q''_{CHF}}{Gh_{lv}} = 0.12\left(\frac{\mu_l}{\mu_v}\right)^{0.183}\left(\frac{\rho_v}{\rho_l}\right)^{0.062} We_l^{-0.141}\left(\frac{L_{ev}}{d_{heat}}\right)^{-0.7}\left(\frac{d_{heat}}{d_{th}}\right)^{0.11} \quad (3.77)$$

$$d_{th} = \frac{1}{0.5}\left(\frac{\sigma}{g(\rho_l - \rho_v}\right)^{0.5} \quad (3.78)$$

$$We_l = \frac{G^2 L_{ev}}{\sigma\rho_l} \quad (3.79)$$

The wall critical heat flux, q''_{CHF} is transformed into a base critical heat flux with Eq. (3.80) by assuming total heat load conservation.

$$CHF_{base} = q''_{CHF}\frac{N_{mc}(W_{mc} + 2H_{mc})}{W_{ev}} \quad (3.80)$$

With that, the safety factor of the system SF (-), is computed with the following equation.

$$SF = \frac{CHF_{base}}{q''_{base}} \quad (3.81)$$

3.4 Riser

The inlet of the riser is also the outlet of the evaporator so, the riser receives a two-phase mixture of vapor and liquid with its thermodynamic state being a result of the flow boiling that took place in the evaporator. This two-phase mixture is driven by buoyancy and gravity to the inlet of the condenser. Because the riser is assumed adiabatic, the heat source term in Eq. (3.7) is equal to 0 $\left(\frac{q"S}{V} = 0\right)$ thus, the mathematical model resumes to determining its pressure variations.

3.4.1 Frictional pressure drop

The frictional pressure drop for two-phase flow in the riser is obtained with the model by Friedel (1979) shown in the set of equations (Eq.(3.82)).ϕ is the two-

phase multiplier, C_{F1} C_{F2} are constants for the correlation, and F and We are the dimensionless Froude and Weber number, respectively.

$$\begin{cases} \phi_{lo}^2 = C_{F1} + \dfrac{3.24 C_{F2}}{F^{0.045} We^{0.0035}} \\ C_{F1} = (1-x)^2 + x^2 \left(\dfrac{\rho_l}{\rho_v}\right)\left(\dfrac{f_{vo}}{f_{lo}}\right) \\ C_{F2} = x^{0.78}(1-x)^{0.24} \left(\dfrac{\rho_l}{\rho_v}\right)^{0.91} \left(\dfrac{\mu_v}{\mu_l}\right)^{0.19} \left(1 - \dfrac{\mu_v}{\mu_l}\right)^{0.7} \\ F = \dfrac{G^2}{gD\rho_{lv}^2} \\ We = \dfrac{G^2 D}{\rho_{lv}\sigma} \\ \left.\dfrac{dP}{dz}\right|_{fr} = \phi \left.\dfrac{dP}{dz}\right|_{lo} \end{cases} \quad (3.82)$$

3.5 Condenser

The model considers a water-cooled tube-in-tube condenser where the working fluid flows into the inner chamber and exchanges heat with the water which flows counter-current in the annulus. The condenser is represented in Figure 3.4.

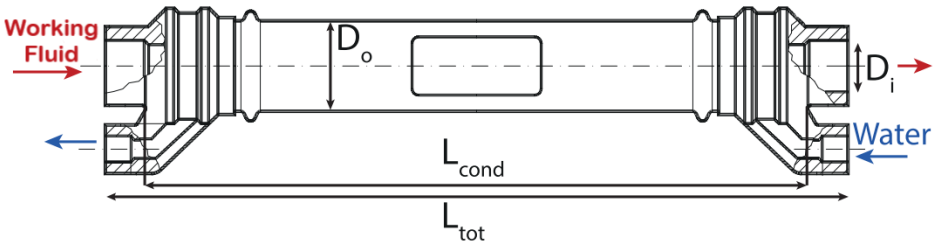

Figure 3.4 – Tube-in-tube condenser drawing (Lamaison, 2014)

The refrigerant flows into the inlet as a two-phase mixture and the desired outlet flow is single-phase liquid, in a saturated or subcooled state, ensuring that only liquid will be passed through into the downcomer's inlet.

The energy equation in the condenser for the refrigerant and secondary fluid side can be simplified into Eq. (3.83). Where U_{cd} is the condenser overall heat transfer coefficient, L_{ex} is the length of heat exchanged in the widthwise direction of the condenser, and T_{cd} and $A_{cd,ref}$ represent the temperature of condensation and heat transfer area for the refrigerant and T_{sec} and $A_{cd,sec}$, for the secondary fluid analogously.

$$\begin{cases} \left.\frac{\partial h}{\partial z}\right|_{ref} = -\frac{U_{cd} L_{ex} (T_{cd} - T_{sec})}{\rho_{lv} u A_{cd,ref}} \\ \left.\frac{\partial h}{\partial z}\right|_{sec} = +\frac{U_{cd} L_{ex} (T_{cd} - T_{sec})}{\rho_{lv} u A_{cd,sec}} \end{cases} \quad (3.83)$$

3.5.1 Single-phase flow

3.5.1.1 Laminar developed flow

For single-phase flow in laminar regime in the condenser, the flow is considered as fully developed so, the correlation for the friction factor is given by the well-known equation presented in Eq. (3.84).

$$f = \frac{16}{Re_{dh}} \quad (3.84)$$

And the frictional pressure drop is obtained with Eq. (3.27).

3.5.1.2 Turbulent flow

For single-phase turbulent flow, the frictional pressure drop is computed with the correlation by Petukhov (1970) presented in section 3.3.1.2, Eq. (3.26).

3.5.2 Condensing flow

The frictional pressure drop for the two-phase condensing flow is also obtained with the model by Müller-Steinhagen and Heck (1986) used for the evaporating pressure drop and presented in Eq. (3.29).

The heat transfer coefficient for both the single-phase and two-phase condensing flow is obtained with an experimentally fitted correlation by Lamaison (2014) for the condenser overall heat conductance. This experimental correlation was chosen since Lamaison (2014) reported that the local heat transfer coefficient models, namely fully developed flow on the water side, and Shah (1979) model on the condensing side, were observed to severely underpredict the condenser overall heat conductance by about 80% when compared to their experimental data.

The condenser overall heat conductance is given by the experimental correlation of Lamaison (2014) which is a function of the mass flow rate of the water and the logarithmic mean temperature difference:

$$UA_{cd} = -0.01664\dot{m}_{water}^2 - 1.2985\dot{m}_{water} + 0.01744LMTD^2 - 1.3481LMTD + 0.04997\dot{m}_{water}LMTD + 29.93 \quad (3.85)$$

The logarithmic mean temperature difference is obtained with Eq. (3.86).

$$LMTD = \frac{\Delta T_A - \Delta T_B}{ln(\Delta T_A/\Delta T_B)} \quad (3.86)$$

Where:

$$\begin{cases} \Delta T_A = T_{in,ref} - T_{out,water} \\ \Delta T_B = T_{out,ref} - T_{in,water} \end{cases} \quad (3.87)$$

3.6 Downcomer

Like the riser, the downcomer is also assumed adiabatic, there is no need to apply a heat transfer model, only a frictional pressure drop model.

For laminar flow (Re<2300), the flow is assumed fully developed and the friction factor is obtained with Eq. (3.84). And for turbulent flow (Re>2300), the friction factor is computed with the Petukhov (1970) correlation shown in Eq. (3.26).

3.7 Pressure loss across a bend

The pressure drop attributed to a bend for single-phase flow is computed with Eq. (3.88), where k (-) is the pressure drop coefficient.

$$\Delta P_{bend} = k \frac{G^2}{2\rho} \tag{3.88}$$

Since the two-phase flow is assumed as homogeneous, Eq. (3.88) is applied to all of the components of the thermosyphon, to determine its pressure drop due to bends.

4 Numerical solution

To solve the set of conservative equations (Eqs. (3.5) to (3.7)) for each component, Seuret et al. (2018) proposed using backward finite differences at every volume except for the pressure and enthalpy, whereas the forward finite difference scheme was applied to determine the next finite volume. This scheme was proposed to simplify the complexity of the model, since there is an inter-dependency of the steady-state equations, requiring a pressure-velocity coupling algorithm. Because of the inconsistency of using both backward and forward schemes, there could be error/delay between the studied volumes, so the authors noted that the volumes should be small enough to minimize them.

4.1 Finite difference method

The following equations (4.1) to (4.3) present the finite difference method which applies a truncated Taylor series expansion for first-order derivatives, in forward, backward and centered scheme, respectively. And Eq. (4.4) shows a centered difference approximation for a second-order derivative, which will be later implemented to solve the two-dimensional heat conduction in the heat package.

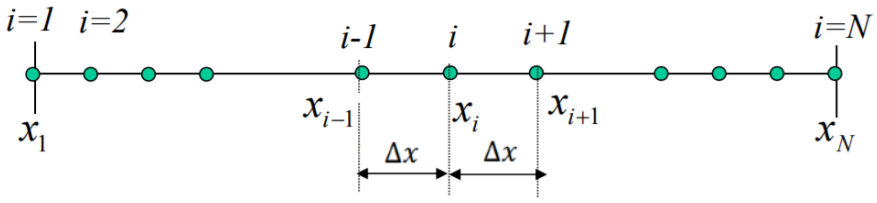

Figure 4.1 – Finite difference method

Figure 4.1 displays the process of discretization which is the division of a domain, in this case in the x-direction, into a series of nodes that vary between 1 and N (total length of the domain) and have a distance between them of Δx.

Forward difference approximation:

$$\frac{dy}{dx} \cong \frac{y_{i+1} - y_i}{\Delta x} \tag{4.1}$$

Backward difference approximation:

$$\frac{dy}{dx} \cong \frac{y_i - y_{i-1}}{\Delta x} \tag{4.2}$$

Centered difference approximation:

$$\frac{dy}{dx} \cong \frac{y_{i+1} - y_{i-1}}{2\Delta x} \tag{4.3}$$

$$\frac{d^2y}{dx^2} \cong \frac{y_{i+1} - 2y_i + y_{i-1}}{\Delta x^2} \tag{4.4}$$

In summary, the finite difference is a numerical method that substitutes the derivates in a specific equation, with approximations that enable the equation to be solved numerically.

4.2 Discretization of the equations

4.2.1 Flow-wise spatial discretization

The method reported by Seuret et al. (2018) is also applied here, and the partial differential conservative equations for continuity, momentum and energy presented in Eqs. (3.5) to (3.7) are thus discretized applying the finite difference method in its explicit form, resulting in local ordinary differential equations (Eqs. (4.5) to (4.7)) where subscript i refers to the i^{th} flow element.

$$u_i = \frac{\rho_{i-1} u_{i-1}}{\rho_i} \tag{4.5}$$

$$P_{i+1=} \left(-\rho_i g \sin\theta - \left(\frac{\partial P}{\partial z}\right)_{fr,i} - \frac{u_i - u_{i-1}}{\Delta z} \rho_i u_i \right) \Delta z + P_i \tag{4.6}$$

$$h_{i+1} = \left(u_i \left(\frac{\partial P}{\partial z}\right)_{fr,i} + \frac{\dot{q} S}{V} - \rho_i g \sin\theta \, u_i - \frac{1}{2} \frac{\rho_i u_i^3 - \rho_{i-1} u_{i-1}^3}{\Delta z} \right) \frac{\Delta z}{\rho_i u_i} + h_i \tag{4.7}$$

The only exception is made for the first element $i = 1$ since the numerical simulation is run in Matlab, and the software starts its numbering process of vectors at 1, there is not an element 0. To remedy this, for the first element only, it is considered:

$$\frac{u_i - u_{i-1}}{\Delta z} = 0 \tag{4.8}$$

$$\frac{\rho_i u_i^3 - \rho_{i-1} u_{i-1}^3}{\Delta z} = 0 \tag{4.9}$$

As it was mentioned (Seuret et al., 2018), the studied volumes must be small enough that possible errors regarding the inconsistency of using both backward and forward difference in the same model, is mostly reduced.

Following the inlet of the flow in a component of the thermosyphon, the thermodynamic state in the next flow element $(i + 1)$ is determined with the pressure and enthalpy obtained from solving the conservative equations (4.6) and (4.7). This process is continuously executed until all 100 elements have their thermodynamic state defined. The numerical solution process is done by Matlab using REFPROP to obtain the fluid's properties. Figure 4.2 illustrates this numerical solution procedure.

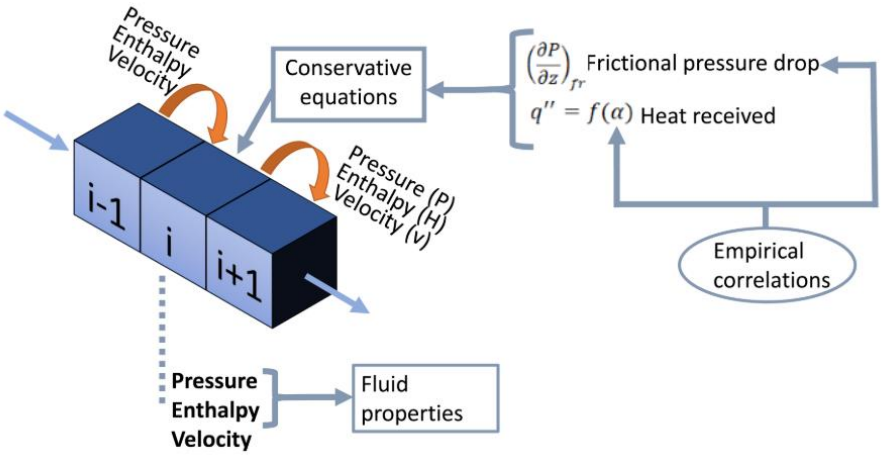

Figure 4.2 – Numerical solution procedure (Seuret et al., 2018)

4.2.2 Two-dimensional heat conduction

To solve the heat conduction in the heat sink package, first, the package is discretized perpendicular to the flow (heat flux direction), and along the flow direction, creating a two-dimensional grid represented in Figure 4.3.

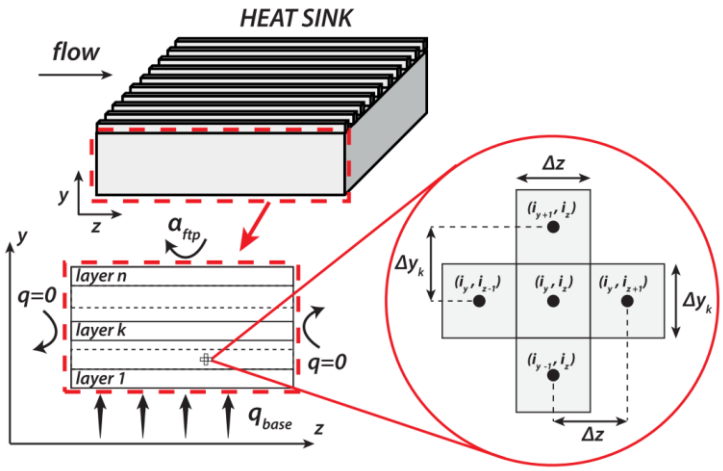

Figure 4.3 – Two-dimensional grid of the heat sink package

The sides of the heat package are considered adiabatic, and the heat flux generated by the CPU chip is given by q''_{base}. The heat exchanged by convection with the fluid on top of the package is modeled using α_{ftp}, which is obtained with the correlations showed in section 3.3. Therefore, the boundary conditions of the two-dimensional heat conduction are given by Eq. (4.10).

$$\begin{cases} q''_{(z=0)} = 0 \\ q''_{(z=L_{ev})} = 0 \\ q''_{(y=0)} = q''_{base} \\ q''_{(y=ftp)} = \alpha_{ftp}(T_{ftp} - T_{fl}) \end{cases} \quad (4.10)$$

The interior nodes of the discretized grid are given by the two-dimensional steady-state conduction equation in the heat sink package, with k representing each layer which is composed of a different material.

$$0 = \frac{\lambda_k}{\rho_k c_{p_k}} \left(\frac{\partial^2 T}{\partial z^2} + \frac{\partial^2 T}{\partial y^2} \right) \quad (4.11)$$

Each layer k is divided into the same number of elements in the y-direction, but since each layer has a different thickness, this leads to distinct values for Δy which are the increments in the y-direction. The z-direction is discretized with the same number of elements used to divide the flow in the evaporator.

4.2.2.1 Interior nodes

The heat conduction equation in finite difference form using truncated Taylor series expansion in a centered difference scheme for the interior nodes:

$$\begin{cases} \frac{\partial^2 T}{\partial z^2} = \frac{T_{i+1,j} - 2T_{i,j} + T_{i-1,j}}{\Delta z^2} \\ \frac{\partial^2 T}{\partial y^2} = \frac{T_{i,j+1} - 2T_{i,j} + T_{i,j-1}}{\Delta y^2} \end{cases} \quad (4.12)$$

Where subscript i refers to the discretized z-direction, and j to the y-direction.

The finite difference equation (4.13) is obtained by incorporating Eq. (4.12) in Eq. (4.11).

$$0 = \frac{1}{\Delta z^2}\left(T_{i+1,j} + T_{i-1,j}\right) + \frac{1}{\Delta y^2}\left(T_{i,j+1} + T_{i,j-1}\right) - \left(\frac{2}{\Delta z^2} + \frac{2}{\Delta y^2}\right) T_{i,j} \quad (4.13)$$

And by applying the finite-differenced equation to every interior node, the resulting set of linear algebraic equations (4.14) can be written in the form of:

$$\begin{cases} b_{1,1}T_1 + b_{1,2}T_2 + \cdots + b_{1,ny}T_{nzny} = I_1 \\ b_{2,1}T_1 + b_{2,2}T_2 + \cdots + b_{2,ny}T_{nzny} = I_2 \\ \vdots \\ b_{nz,1}T_1 + b_{nz,2}T_2 + \cdots + b_{nz,ny}T_{nzny} = I_{nzny} \end{cases} \quad (4.14)$$

Where nz and ny are the number of elements in the z and y-direction, respectively. $T_1, T_2, \ldots, T_{nzny}$ are the unknown nodal temperatures, $a_{1,1}, \ldots, a_{ny,nz}$ are the coefficients of the nodal temperatures and $I_1, \ldots, I_{nzny}$ are the independent terms.

Equation (4.14) can be written in matrix notation:

$$\begin{cases} [B] = \begin{bmatrix} b_{1,1} & \cdots & b_{1,ny} \\ \vdots & \ddots & \vdots \\ b_{nz,1} & \cdots & b_{nz,ny} \end{bmatrix}_{nz,ny} ; [T] = \begin{bmatrix} T_1 \\ T_2 \\ \vdots \\ T_{nzny} \end{bmatrix}_{(nz \times ny,1)} ; [I] = \begin{bmatrix} I_1 \\ I_2 \\ \vdots \\ I_{nzny} \end{bmatrix}_{(nz \times ny,1)} \\ [B][T] = [I] \end{cases} \quad (4.15)$$

4.2.2.2 Boundary condition nodes

For the boundary condition nodes, an energy balance is performed for a control surface under a prescribed constant heat flux, for all regions of the heat sink package. The energy balance is also written in finite differences.

The left and right walls of the package for all materials are considered insulated thus, $q'' = 0$. Figure 4.4 and equation (4.16) display the energy balance for a control surface on the left wall of the heat sink package. Where $q''_{i,j}$ represents the heat flux coming in through the boundary surface, and the other terms pertain to the heat in through conduction for the three remaining surfaces by applying Fourier's Law. One unit per depth is considered for all control surfaces.

Left wall:

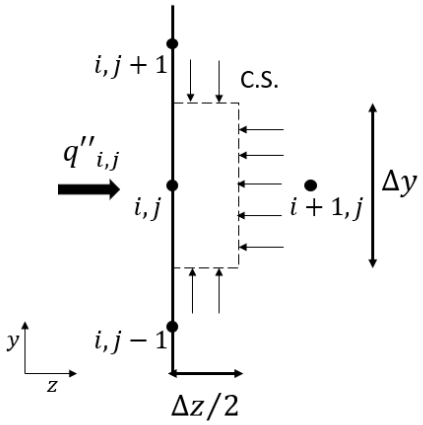

Figure 4.4 – Energy balance on a control surface for the left wall of the heat sink package

$$\begin{cases} q''_{i,j} = 0 \\ \left(\frac{\lambda_k \Delta y_k}{\Delta z}\right)\left(T_{i+1,j} - T_{i,j}\right) + \left(\frac{\lambda_k \Delta z}{2\Delta y_k}\right)\left(T_{i,j-1} - T_{i,j}\right) \\ \quad + \left(\frac{\lambda_k \Delta z}{2\Delta y_k}\right)\left(T_{i,j+1} - T_{i,j}\right) = 0 \end{cases} \tag{4.16}$$

An energy balance is also performed for the right wall of the package which is also considered adiabatic. A schematic of the energy balance is provided by Figure 4.5, and Eq. (4.17) shows the balance.

Right wall:

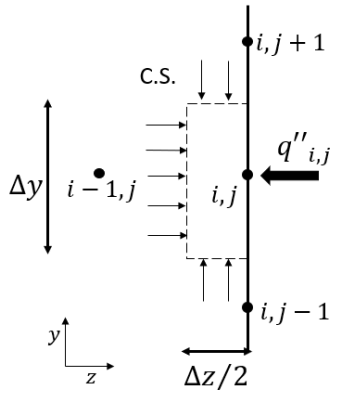

Figure 4.5 – Energy balance on a control surface for the right wall of the heat sink package

$$\begin{cases} q''_{i,j} = 0 \\ \left(\frac{\lambda_k \Delta y_k}{\Delta z}\right)(T_{i-1,j} - T_{i,j}) + \left(\frac{\lambda_k \Delta z}{2\Delta y_k}\right)(T_{i,j+1} - T_{i,j}) \\ + \left(\frac{\lambda_k \Delta z}{2\Delta y_k}\right)(T_{i,j-1} - T_{i,j}) = 0 \end{cases} \quad (4.17)$$

Similarly, the same process is applied to the top wall of the package where the heat transfer coefficient α_{ftp} which takes into account the heat exchanged by convection with the fluid, gives the heat flux coming in through the boundary condition on the top of the package. And Eq. (4.18) shows the energy balance for the top wall of the package.

Top wall:

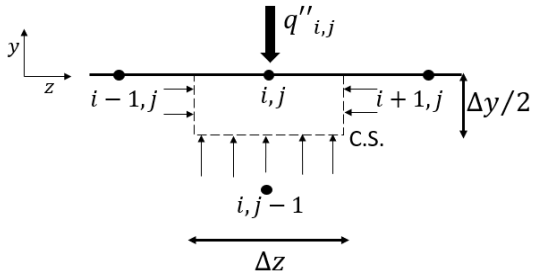

Figure 4.4 – Energy balance on a control surface for the top wall of the heat sink package

$$\begin{cases} q''_{i,j} = \alpha_{ftp}(T_{i,j} - T_{fl}) \\ \left(\frac{\lambda_k \Delta y_k}{2\Delta z}\right)(T_{i+1,j} - T_{i,j}) - \left(\frac{\lambda_k \Delta y_k}{2\Delta z}\right)(T_{i,j} - T_{i-1,j}) \\ - \left(\frac{\lambda_k \Delta z}{\Delta y_k}\right)(T_{i,j} - T_{i,j-1}) = -\alpha_{ftp}(T_{i,j} - T_{fl})\Delta z \end{cases} \quad (4.18)$$

On the lower wall, the heat in through the boundary condition q''_{base} is originated from the CPU chip. The energy balance is also applied for this control surface.

Lower wall:

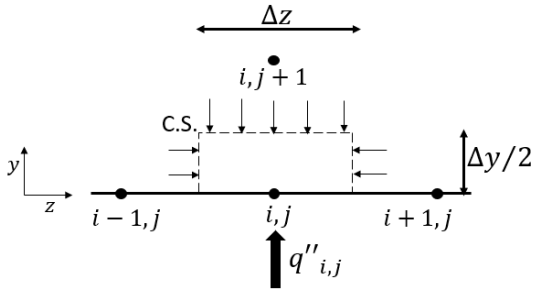

Figure 4.5 – Energy balance on a control surface for the lower wall of the heat sink package

$$\begin{cases} q''_{i,j} = q''_{base} \\ \left(\frac{\lambda_k \Delta y_k}{2\Delta z}\right)(T_{i+1,j} - T_{i,j}) - \left(\frac{\lambda_k \Delta y_k}{2\Delta z}\right)(T_{i,j} - T_{i-1,j}) \\ \quad -\left(\frac{\lambda_k \Delta z}{\Delta y_k}\right)(T_{i,j} - T_{i,j+1}) = -q''_{base}\Delta z \end{cases} \tag{4.19}$$

To account for all types of boundary surfaces, the energy balance is also performed on the corners of the package. Since the left and right walls are insulated, for the heat coming in through the boundary, the heat flux from the chip was considered for the bottom corners, and the heat from the convection with the working fluid was assumed for the top corners.

Bottom left corner:

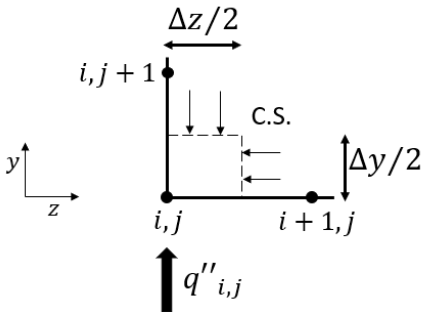

Figure 4.6 – Energy balance on a control surface for the bottom left corner of the heat sink package

$$\begin{cases} q''_{i,j} = q''_{base} \\ -\left(\frac{\lambda_k \Delta y_k}{2\Delta z}\right)\left(T_{i,j} - T_{i+1,j}\right) - \left(\frac{\lambda_k \Delta z}{2\Delta y_k}\right)\left(T_{i,j} - T_{i,j+1}\right) = -\frac{q''_{base}\Delta z}{2} \end{cases} \quad (4.20)$$

Bottom right corner:

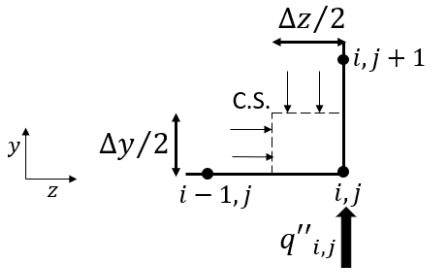

Figure 4.7 – Energy balance on a control surface for the bottom right corner of the heat sink package

$$\begin{cases} q''_{i,j} = q''_{base} \\ -\left(\frac{\lambda_k \Delta y_k}{2\Delta z}\right)\left(T_{i,j} - T_{i-1,j}\right) + \left(\frac{\lambda_k \Delta z}{2\Delta y_k}\right)\left(T_{i,j+1} - T_{i,j}\right) = -\frac{q''_{base}\Delta z}{2} \end{cases} \quad (4.21)$$

Top right corner:

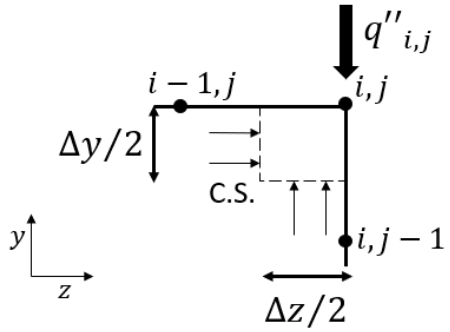

Figure 4.8 – Energy balance on a control surface for the top right corner of the heat sink package

$$\begin{cases} q''_{i,j} = \alpha_{ftp}(T_{i,j} - T_{fl}) \\ \left(\frac{\lambda_k \Delta y_k}{2\Delta z}\right)\left(T_{i-1,j} - T_{i,j}\right) + \left(\frac{\lambda_k \Delta z}{2\Delta y_k}\right)\left(T_{i,j-1} - T_{i,j}\right) \\ \quad = -\frac{\alpha_{ftp}(T_{i,j} - T_{fl})\Delta z}{2} \end{cases} \quad (4.22)$$

Top left corner:

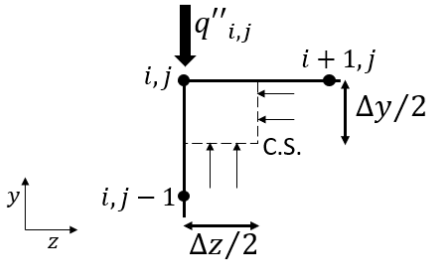

Figure 4.9 – Energy balance on a control surface for the top left corner of the heat sink package

$$\begin{cases} q''_{i,j} = \alpha_{ftp}(T_{i,j} - T_{fl}) \\ \left(\frac{\lambda_k \Delta y_k}{2\Delta z}\right)(T_{i+1,j} - T_{i,j}) - \left(\frac{\lambda_k \Delta z}{2\Delta y_k}\right)(T_{i,j} - T_{i,j-1}) \\ \quad = -\frac{\alpha_{ftp}(T_{i,j} - T_{fl})\Delta z}{2} \end{cases} \tag{4.23}$$

4.2.2.3 Heat conduction solution

For this particular chosen heat sink package, the same is composed of three layers, the top one being copper, the middle, a thermal interface material which is made of a high thermal conductivity alloy made of gallium, indium, and tin (62.5% Ga; 21.5% In; 16.0% Sn), with the commercial name of Indalloy 51. And finally, a silicon layer that represents the electronic component needs cooling. Table 4.1 points out the thermal conductivity and thickness of each layer.

Table 4.1 – Description of heat sink package materials

Material	Thermal Conductivity [$\boldsymbol{W/(m.K)}$]	Thickness of each layer [$\boldsymbol{mm}$]
Copper	394	1.8
TIM	35	0.1
Silicon	148	0.35

To obtain the CPU's chip temperature T_{chip} and the temperature at the footprint T_{ftp}, which itself is necessary to solve the micro-evaporator module, the two-dimensional heat conduction is solved numerically by performing an inversion of the coefficient matrix $[A]$ in Matlab, to obtain the temperature in all of the nodes given by vector $[T]$, according to equation (4.24).

$$[T] = [B]^{-1}[I] \qquad (4.24)$$

The maximum temperature obtained in the silicon layer is assumed as the chip's temperature.

4.3 Evaporator's loop

Since the energy balance of the micro-evaporator depends on the footprint heat flux, which itself is a function of the unknown two-phase wall heat flux and heat transfer coefficient, an iteration procedure is needed. Figure 4.10 presents the flowchart which explains the iteration process. With an iteration method proposed by Steffensen (1933), the heat transfer coefficient for two-phase flow is determined by both the balance equation (Eq.(3.8)), and the correlations for boiling flow presented in section 3.3.2.2., which are functions of the wall heat flux.

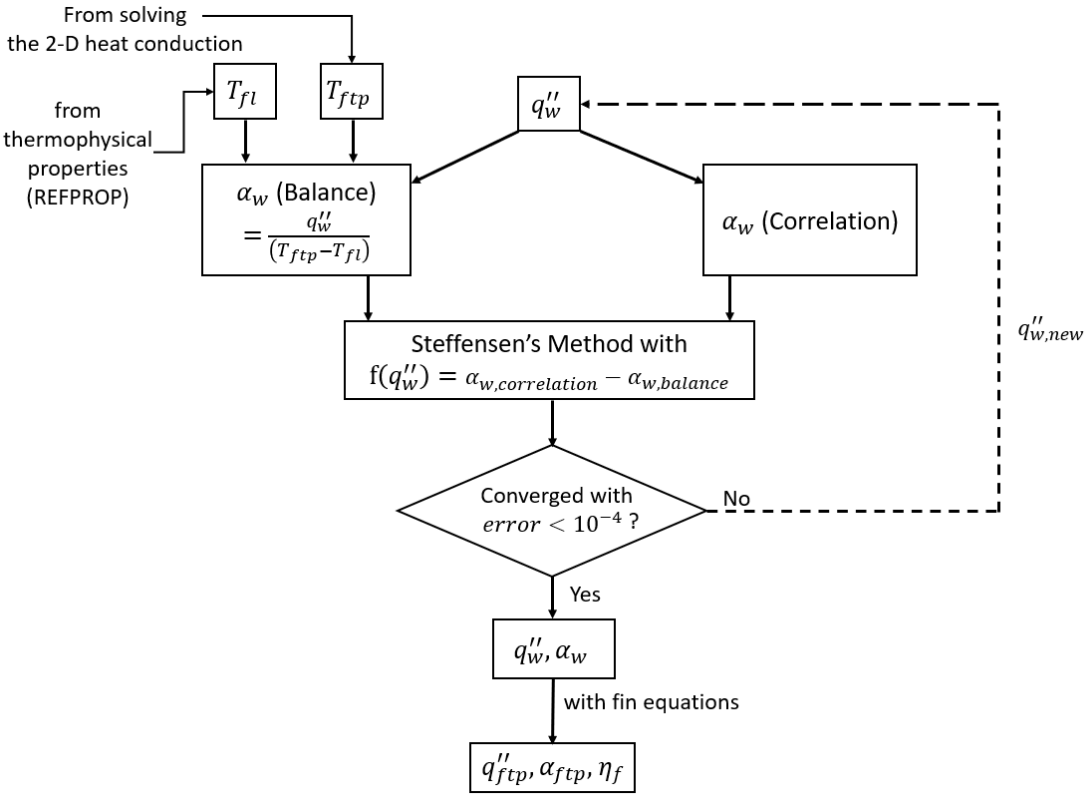

Figure 4.10 – Flowchart for the two-phase wall heat transfer coefficient iteration process

In addition, in the first iteration, the guess value for the two-phase q''_w is the wall heat flux at the previous flow element.

$$q''_w(i) = q''_w(i-1) \qquad (4.25)$$

In this work the Steffensen's iteration method was chosen in place of Newton Raphson's (Lamaison, 2014) since in contrast to Newton's method,

Steffensen's method is derivative-free, and this simplifies its application. Plus, Steffensen's method is also quadratically convergent, and Brown (1977) reported that Steffensen's method was superior to Newton's method in terms of computer run time. According to Steffensen (1933):

$$x_{n+1} = x_n - \frac{[f(x_n) - x_n]^2}{f(f(x_n)) - 2f(x_n) + x_n} \tag{4.26}$$

With Eq. (4.26) the new value for q''_w is obtained for the next iteration.

Figure 4.11 displays the flowchart of the entire evaporator. As can be observed, there is an initialization process for $T_{ftp}(z)$, where for the first iteration for the evaporator, the temperature at the footprint is initialized as 1 degree above the fluid's temperature, for all flow elements of the micro-evaporator, as given by Eq. (4.27).

$$T_{ftp}(z) = T_{fl}(i) + 1 \text{ , for iteration=1} \tag{4.27}$$

After all of the flow elements have been computed for the first iteration, the error over the heat received is calculated, where the heat at the footprint for each element is added and compared to the heat applied at the base of the heat sink package. If the error is lower than 10^{-2}, this iteration is saved, and the outlet thermodynamic state will be the inlet of the riser. However, if the error is higher than 10^{-2}, the temperature at the footprint along the flow direction is updated with the values obtained when solving the two-dimensional heat conduction in the package. This iteration process is repeated until the conversion criterium is met.

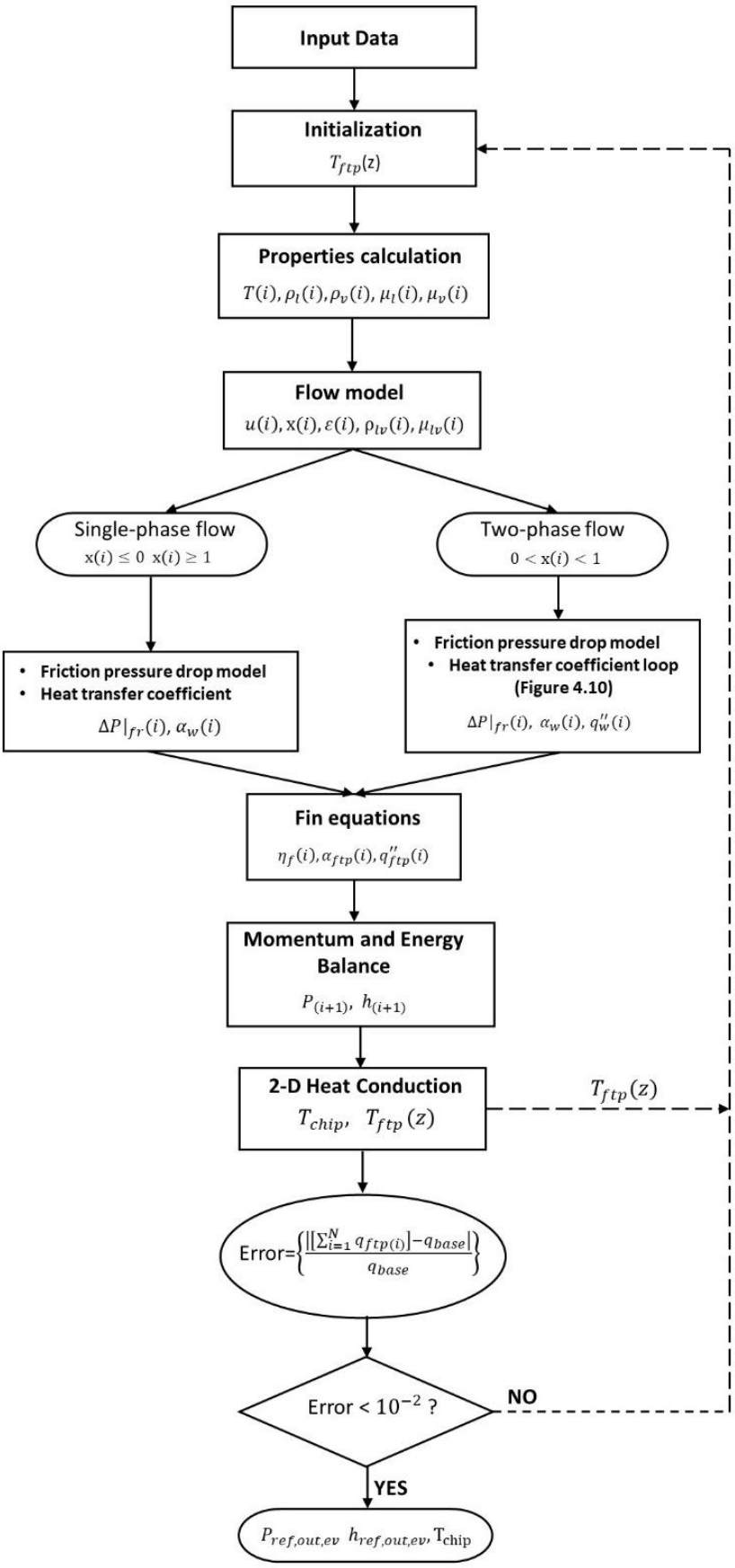

Figure 4.11 – Flowchart for the evaporator with its iteration process

4.4 Thermosyphon loop

The biggest challenge after modeling all the thermosyphon's components separately is to link them in a full simulation to close the loop. The numerical simulation executes one component after the other by assuming that its outlet thermodynamic state, is the inlet of the next component of the loop. And, with this process, the loop can be closed. As shown in table 4.2, the numerical model is coded in a way to take the geometry, the bottom chip heat flux, the filling ratio of the refrigerant, the mass flow rate of the water, and its inlet temperature as inputs for the model. And the outputs are all the characteristics of the thermosyphon, namely the thermodynamic and thermophysical properties of the working fluid across the whole loop, the temperature of the chip, and its mass flow rate.

Table 4.2 – Inlet and outlet parameters for the two-phase thermosyphon numerical model

Inlet	**Outlet**
• Working fluid • Geometry • Filling ratio • Chip heat flux • Water mass flow rate • Water inlet temperature	• Temperature, pressure, enthalpy, etc, in each element • Refrigerant mass flow rate • Temperature of the chip

The model starts right at the inlet of the evaporator. To initialize its thermodynamic state, the saturated temperature of the evaporator is assumed to be equal to the outlet temperature of the water, computed with the bottom heat flux (Eq. 4.28). Moreover, the initial enthalpy is calculated assuming saturated liquid at the evaporator's inlet ($x = 0$). With the temperature and enthalpy of the refrigerant set, it is possible to obtain the starting pressure at the inlet of the evaporator with REFPROP.

Then, the mass flow rate of the refrigerant is initialized with the vapor quality of the refrigerant at the outlet assumed to be $x_{out,ev} = 0.4$. So, the mass flow rate at the start is given by Eq. (4.28).

$$\begin{cases} q_{base} = q''_{base} S_{ev} \\ T_{w,out,cd} = \dfrac{q_{base}}{\dot{m}_w cp_w} + T_{w,in,cd} \\ T_{ref,in,ev} = T_{w,out,cd} \\ \dot{m}_{ref,start} = \dfrac{q_{base}}{h_{ref,out,ev} - h_{ref,in,ev}} \end{cases} \tag{4.28}$$

For the loop to be closed, the pressure and enthalpy at the end of the numerical simulation, which is right before the inlet of the evaporator, must be equal to the initial pressure and enthalpy for the same location. If the values of P_{end} and P_{start} does not match an absolute error over the pressure is calculated (Eq. (4.29)), and a new iteration is needed.

$$\Delta P_{error} = P_{end} - P_{start} = \sum_{comp}^{all\ components} \left(\Delta P_{friction,comp} + \Delta P_{momentum,comp} + \Delta P_{static,comp}\right) \tag{4.29}$$

Also, if after one iteration, the pressure is smaller than the initial assumption ($P_{end} < P_{start}$), the pressure drop is too large and the mass-flow rate should be reduced for the next iteration.

Seuret et al. (2018) suggested that the new mass flow rate of the refrigerant should be updated with Eq. (4.30).

$$\dot{m}_{ref,new} = \sqrt{\frac{-\left(\Delta P_{error} - \sum \Delta P_{fr,comp}\right)}{\sum -\dfrac{\Delta P_{fr,comp}}{\dot{m}_{ref}}}} \tag{4.30}$$

However, it was noted that Eq. (4.30) offered a higher value for the mass flow rate when the pressure at the end was smaller than the initial pressure, which contradicts the physics mentioned earlier, that the mass flow rate should be reduced to lower the pressure drop obtained along the loop.

For that reason, another iteration was executed with $\dot{m}_{ref,new} < \dot{m}_{ref,start}$ to obtain a linear interpolation model for the mass flow rate of the refrigerant. With this linear model, a new mass flow rate was approximated. It should be noted that

the interpolation model for the mass flow rate changes for different input conditions.

The enthalpy is also updated for the next iteration, with a simple average between the calculated enthalpy at the inlet of the evaporator, and the enthalpy obtained at the outlet of the downcomer by the model.

$$h_{new} = \frac{\left(h_{start} + h_{ref,out,dc}\right)}{2} \tag{4.31}$$

It is important to note that during this process, P_{start} does not change until the convergence criterium is met (for the mass flow rate and enthalpy), with a relative error over the pressure and enthalpy lower than 1%. Then, the total mass of the system is compared to the initial mass of the system. The initial mass is computed for when the thermosyphon loop is first charged thus, assuming a cold start-up. Equation (4.32) gives the initial mass of refrigerant, as a function of the filling ratio. Where subscript $comp$ refers to each of the components of the thermosyphon loop, and ST stands for standard temperature, assumed as 25°C.

$$\begin{cases} FR = \dfrac{V_{ref}}{V_{total}} \\ M_{initial} = \sum V_{comp}\, FR \rho_{l,ST} \end{cases} \tag{4.32}$$

And the total mass of the loop is computed as the sum of each component's mass, given by Eq. (4.33).

$$M_{total} = \sum \left(1 - \varepsilon_{comp}\right)\rho_{l,comp} + \varepsilon_{comp}\rho_{v,comp} \tag{4.33}$$

The starting pressure P_{start} is now updated and the loop is run until the system converges over the mass too.

Figure 4.12 shows the entire thermosyphon loop's flowchart described in this section.

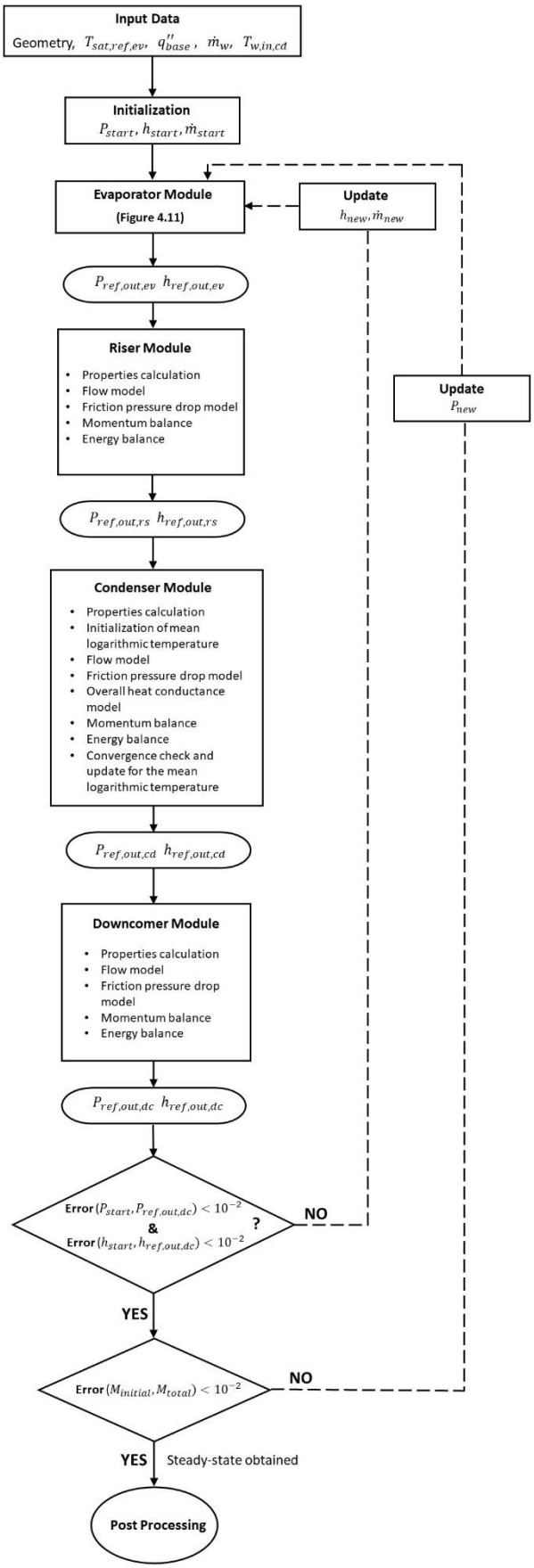

Figure 4.12 – Flowchart of the thermosyphon loop numerical model

5 Results

Table 5.1 presents the geometric parameters for each of the system's components, namely the length, diameter, and angle between the horizontal and the flow direction. Table 5.2 details the additional geometry of the microchannel evaporator. It is important to note that the geometry shown is considered for the numerical simulations as well as for all the experimental campaigns obtained.

The water-cooled tube-in-tube condenser considered is a Danfoss HE 0.5 model, and as mentioned, its overall heat conductance is determined by an experimental correlation by Lamaison (2014) which was presented in Eq. (3.80) in section 3.5.2.

Table 5.1 – Geometry considered for the simulations and experimental validation

Component	Length $[cm]$	Diameter $[mm]$	Angle between the horizontal and the flow direction [°]
Evaporator	1.27	-	0
Riser	25.4	6.35	25
Condenser	17.8	12.8	-2.6
Downcomer	51.6	6.35	-7.8

Table 5.2 – Additional geometric parameters for the micro-fin evaporator

	Width $[mm]$	Height $[mm]$	Number $[-]$
Evaporator	17.78	-	-
Microchannel	0.17	1.7	52
Fin	0.17	-	-

5.1 Grid-Independence analysis

A grid-independence analysis was performed to guarantee the accuracy of the numerical model, and to determine the most computational cost-effective grid for the thermosyphon loop.

During preliminary tests on each component separately, the micro evaporator proved to be the most difficult component to achieve the convergence, given its more intricate iteration processes. Therefore, the grid-independence analysis was focused on investigating chiefly the micro evaporator

Figure 5.1 shows the heat fluxes obtained at the footprint of the micro evaporator, according to the number of elements considered. It also displays the convergence criterium for the micro evaporator, as a solution is achieved when the error between heat flux at the footprint (calculated by the model) and the heat flux of the chip (input of the model) is lower than 0.1. Thereby the convergence is obtained when the result of the heat flux at the footprint lies within the range of $\pm 0.1\ q''_{base}$.

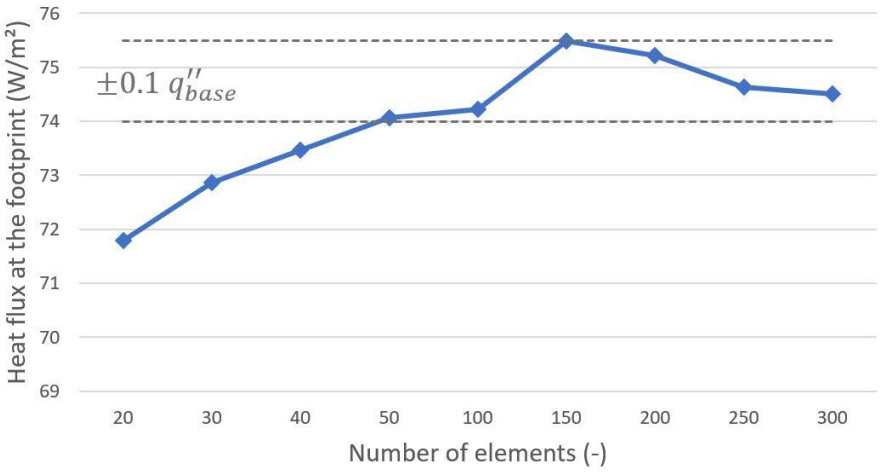

Figure 5.1 – Heat flux at the footprint as a function of the number of elements of the micro evaporator

Observing Fig. 5.1, one can conclude that as the number of elements grow from 20 to 40, the model approaches the solution. And for 50 elements, the model was able to meet the convergence criterium. It can also be seen that, for 100 to 300 elements, even though there is a slight variation on the heat flux at the footprint, the model was still able to reach a solution within the convergence criterium.

The temperature of the chip was also monitored for different number of elements, as shown is Figure 5.2.

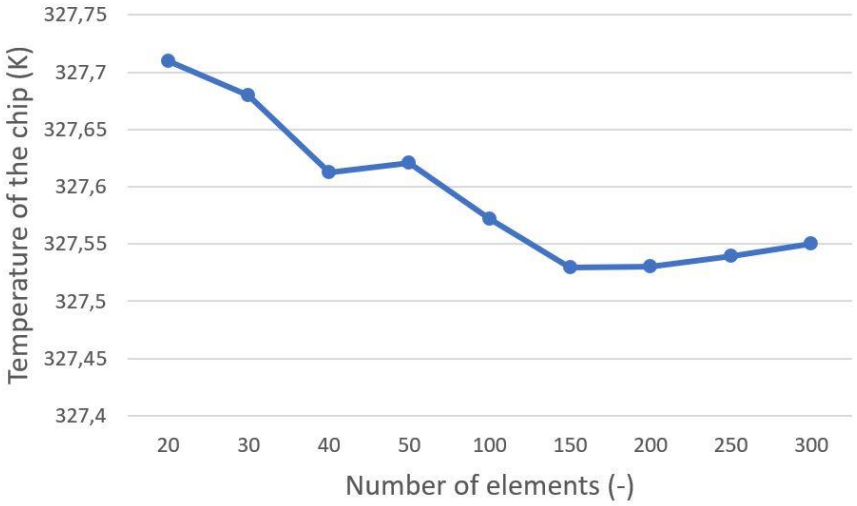

Figure 5.2 –Temperature of the chip as a function of the number of elements of the microevaporator

A more or less trend of increase of number of elements resulting in a decrease of chip temperature can be noted in Fig. 5.2. However, its also possible to notice that an increase from 40 to 50 elements did not followed this observed trend. Because of that, a grid with only 50 elements has been discarded. In addition, for 100 elements or more, the variation of chip temperature is relatively small. Consequently, a grid with 100 elements was chosen as the most computational cost-effective.

Since the condenser solution also must go through an iteration process, its grid was also investigated. A minimum of 10 elements was shown to achieve the same result for the same number of iterations, as grids with higher number of elements. However, for the sake of symmetry, all components were discretized in 100 elements.

5.2 Validation of the numerical model with experimental data

Often the relationship between the refrigerant mass flux (or mass flow rate) as a function of the prescribed heat flux is referred to as the characteristic curve of a thermosyphon. As it was explained in Chapter 2, the thermosyphon operates under two regimes that are the gravity dominant regime (GDR), and the friction dominant regime (FDR). For the GDR, the mass flux increases with an increase of the heat flux, and for the FDR, this trend changes and the mass flux decreases with the continued increase in heat flux. Therefore, the characteristic curve is of great importance to evaluate the behavior of a thermosyphon loop. A model prediction of the characteristic curve of a thermosyphon should be validated against experimental data.

All the experimental data used for comparison with the numerical model, were obtained with software GetData, which promotes the digitalization of data points displayed in graphs, thus making it possible to plot the experimental data and the simulated results together.

Figure 5.3, from Ong et al. (2016) investigation, displays three experimental characteristic curves for refrigerant R134a, all of them obtained for an inlet water temperature of 12 °C and for a geometry given by Tables 5.1 and 5.2, but with different operational conditions for the water mass flow rate and filling ratio.

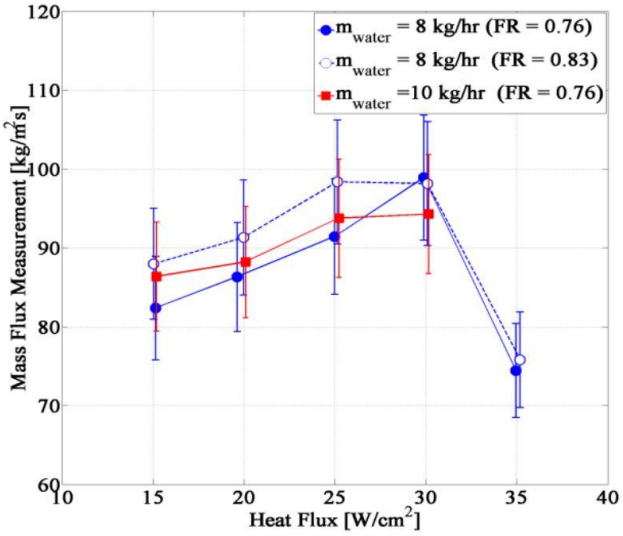

Figure 5.3 – Experimental mass flux measurement with $T_{w,in,cd} = 12℃$ (Ong et al., 2016)

It can be observed that a higher filling ratio resulted in a higher refrigerant mass flux when the thermosyphon is operating under the gravity dominant regime. The experimental campaign with a water mass flow rate of 8 kg/h and a filling ratio of 0.83 was chosen to validate the numerical model.

Due to the non-disclosure of the curvature radius of the existing bends of the experimental apparatus from Ong et al. (2016), it was not possible to carry out a direct calculation of the pressure drop due to these bends. Therefore, a primary test was performed without the addition of the friction pressure drop due to the existing bends.

Figure 5.4 (a) shows the pressure variation of the working fluid, throughout each component of the system, obtained by the present model was plotted against the number of elements of each component.

Although Ong et al. (2016) did not provide an experimental plot of the refrigerant pressure variation of each component, Lamaison et al. (2016a) performed a numerical one (Figure 5.4 (b)). Their model was also validated with the experimental data from Ong et al. (2016), showing a good agreement. In addition, the model by Lamaison et al. (2016a) considered the bends of the experimental apparatus from Ong et al. (2016).

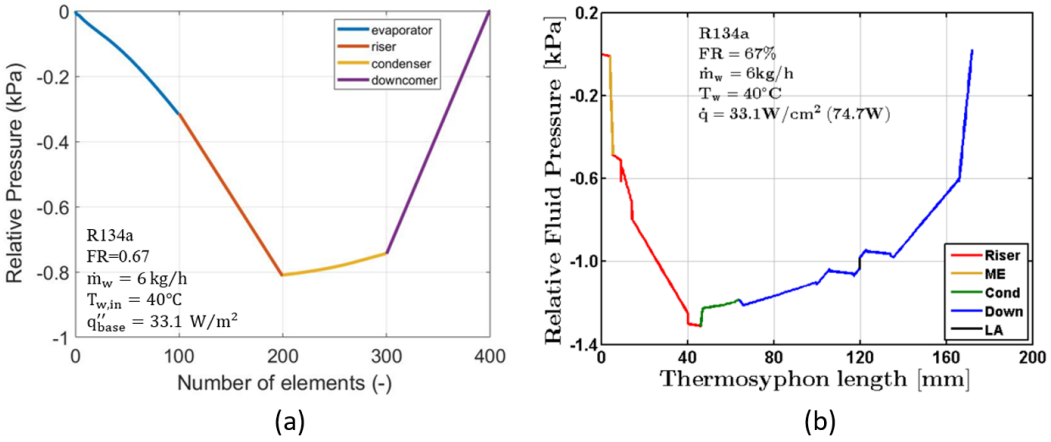

Figure 5.4 – Pressure profile of the thermosyphon loop; (a) Present numerical model; (b) Numerical model of Lamaison et al. (2016a)

The pressure variation in each component of the present model was compared to the data from the numerical model of Lamaison et al. (2016a), operating under the same conditions. The difference in results were assumed to be

the value of the pressure drop due to a bend in each respective component. Accordingly, with the pressure drop as a known parameter, and considering a single bend for each component, its coefficients (k) can be obtained with Equation (3.86).

Table 5.3 exhibits the estimated values for the pressure drop coefficients for each of the thermosyphon components.

Table 5.3 – Pressure drop coefficients due to bends

Pressure drop coefficient due to a bend			
Evaporator k_{ev}	**Riser** k_{rs}	**Condenser** k_{cd}	**Downcomer** k_{dc}
-0.00807	-0.04237	0.22001	0.13808

Figure 5.5 presents the plotting of the numerical model and experimental data (Ong et al., 2016) characteristic curves of a thermosyphon loop, obtained for the same operating conditions. Figure 5.5 also shows the experimental uncertainty range, reported by Ong et al. (2016) and represented by the dashed lines in the plot.

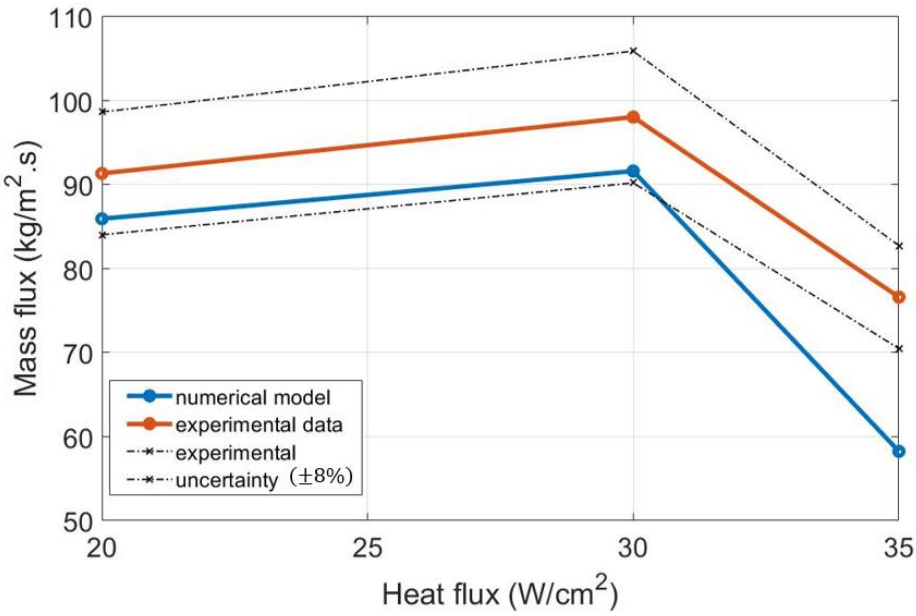

Figure 5.5 – Comparison between the numerical model and the experimental data obtained for the mass flux of the system

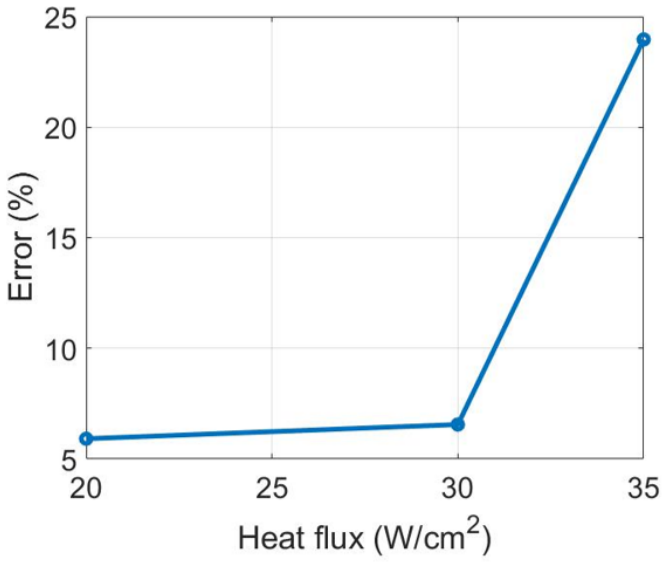

Figure 5.6 –Relative error between the numerical model and the experimental data for the mass flux of the system ($T_{w,in,cd} = 12$°C; $\dot{m}_w = 8\,kg/h\,; FR = 0.83$)

A good agreement for the mass flux (error around 6%, shown in Figure 5.6) can be observed when the thermosyphon is operating under the gravity dominant regime ($q''_{base} \leq 30\,W/cm^2$), with the model slightly under predicting the mass flux. Besides, Ong et al. (2016) reported that their mass flux measurement procedure has an uncertainty of $\pm$8%, thus, the results obtained by the model are within the experimental uncertainty zone.

The numerical model was also able to predict the switch from GDR to FDR, as the mass flux of the system decreased for a heat flux of $35\,\mathrm{W/cm^2}$. This proves that the numerical model was able to predict the complex behavior of the thermosyphon loop. However, a relative error higher than 23% (Figure 5.6) over the mass flux. was computed for the maximum heat flux. This behavior is probably due to an overprediction of the frictional pressure drop, which itself, may be a product of the estimation of the pressure drop due to bends of the experimental apparatus. And, as mentioned previously, this estimation on the value of the pressure drop due to bends throughout the thermosyphon loop, was made because of insufficient data on the existing bends of the experimental apparatus.

Figure 5.7 shows the results of the experimental validation of the model presented by Lamaison et al. (2016a) for the inlet pressure of the evaporator and mean chip temperature as functions of the chip's heat flux. The experimental curve

from Figure 5.7 was also used to validate the numerical model from the present work.

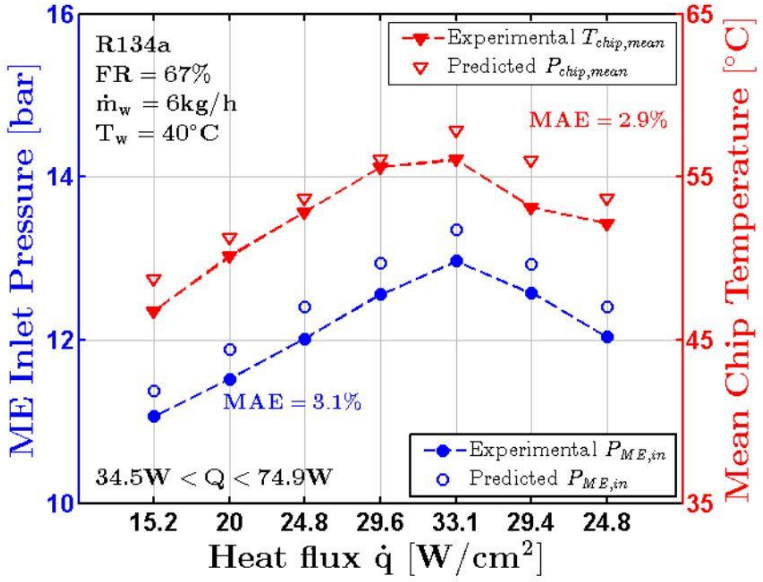

Figure 5.7 – Predicted vs experimental evaporator inlet pressure and mean chip temperature (Lamaison et al., 2016a)

Figures 5.8 and 5.9 present the comparison between the numerical model and the experimental data obtained for the evaporator inlet pressure and chip temperature, respectively.

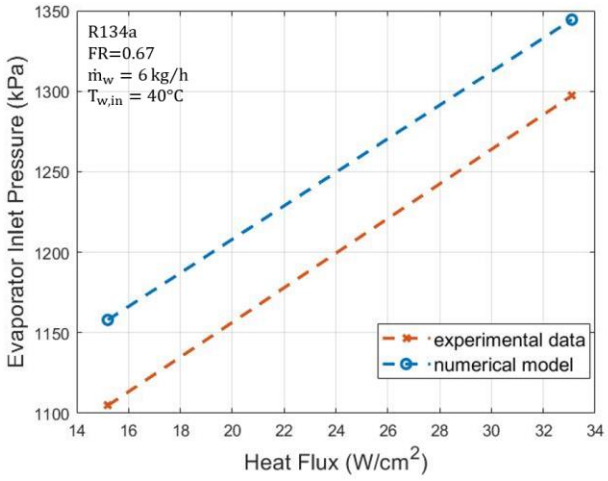

Figure 5.8 – Predicted vs experimental evaporator inlet pressure

The numerical model shows an overprediction of the pressure at the inlet of the evaporator by a maximum of 4.8%. An overprediction for the pressure was also noted for the Lamaison et al. (2016a) model, shown in Figure 5.7.

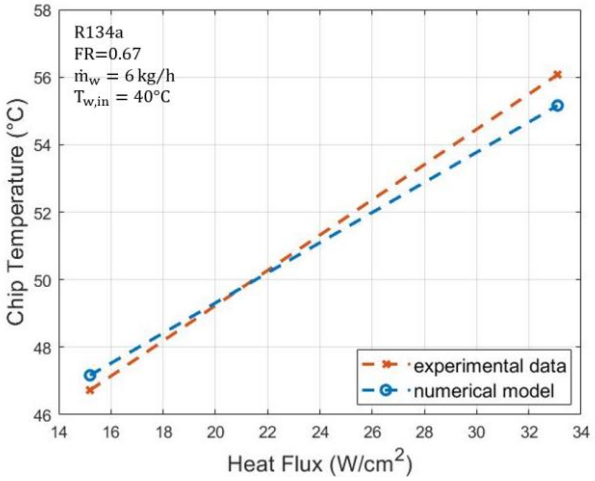

Figure 5.8 – Predicted vs experimental evaporator inlet pressure

Regarding the chip temperature (Fig. 5.9), the model was able to predict it with a reasonable accuracy. The largest discrepancy is seen for the highest heat flux, of 33.1 W/cm^2, although the difference in temperature is still lower than 1°C.

5.3 Comparison of thermal performance of R134a and R1234yf

Figure 5.10 presents the thermosyphon pressure profile for R1234yf as the working fluid. It shows the relative pressure (ratio of inlet pressure to pressure drop) variation along the discretized elements for the system, and as it can be observed, each component was discretized in 100 elements. The downcomer is clearly the component with the highest value of pressure variation, in its case, pressure gain. This gain, a result of the gravity force over the fluid, offsets the large pressure drop from the evaporator and riser, and as mentioned in chapter 1, this behavior drives the working fluid throughout the loop.

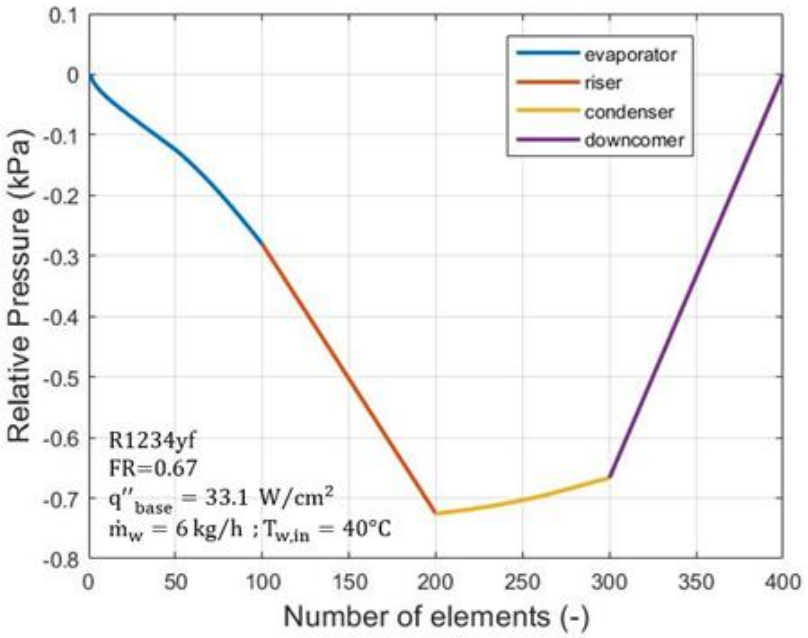

Figure 5.10– Thermosyphon pressure profile for R1234yf

Figure 5.11 exhibits the heat transfer coefficient of R1234yf at the evaporator.

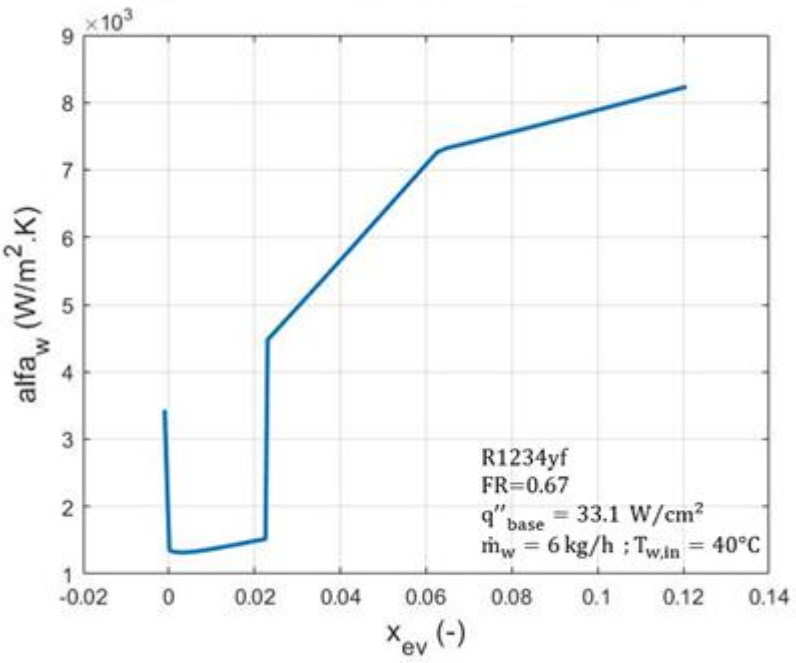

Figure 5.11 – Evaporator's wall heat transfer coefficient as a function of the vapor quality

It can be observed that, the refrigerant at the inlet of the evaporator is slightly subcooled and, as it leaves the evaporator, its two-phase liquid-vapor mixture presents a vapor quality of around 0.12.

Figure 5.12 provides additional information on the heat transfer coefficient. The linear proration factor r, was introduced in chapter 3, varying from 0 to 1, it points out if the heat transfer coefficient is under the three-zone model (slug flow) annular flow, or a transition between the two.

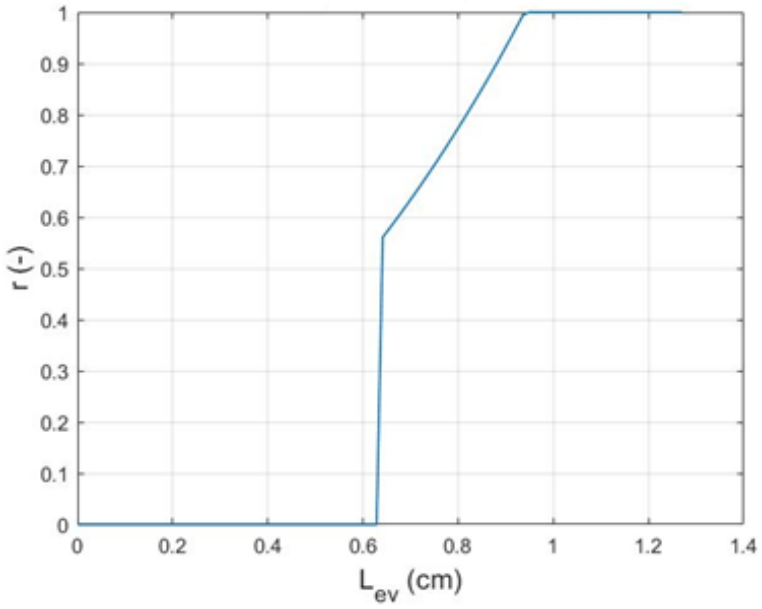

Figure 5.12 – Linear proration factor vs length of the evaporator
(transition from coalescing bubble to annular flow)

Figure 5.12 shows that the transition occurred a little over 0.6 cm from the inlet of the evaporator, where the refrigerant vapor quality was slightly over 0.02. Before that, the heat transfer coefficient was computed with the three-zone model, and after the transition, the annular flow model.

The following figures exhibit comparisons between refrigerants R134a and R1234yf, for the same input conditions.

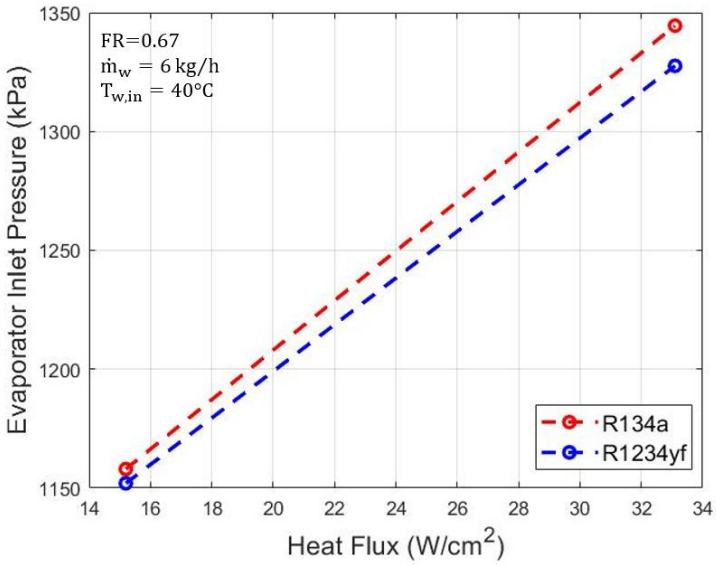

Figure 5.13 – Evaporator inlet pressure comparison for refrigerants R134a and R1234yf

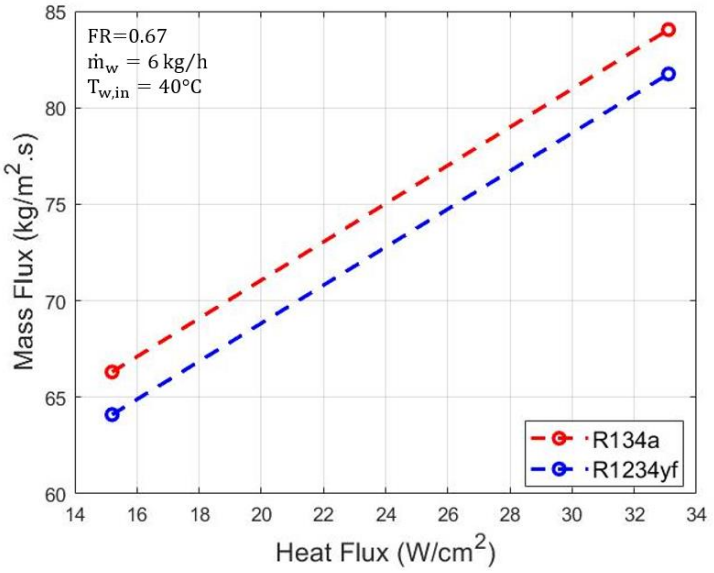

Figure 5.14 – Mass flux comparison for refrigerants R134a and R123yf

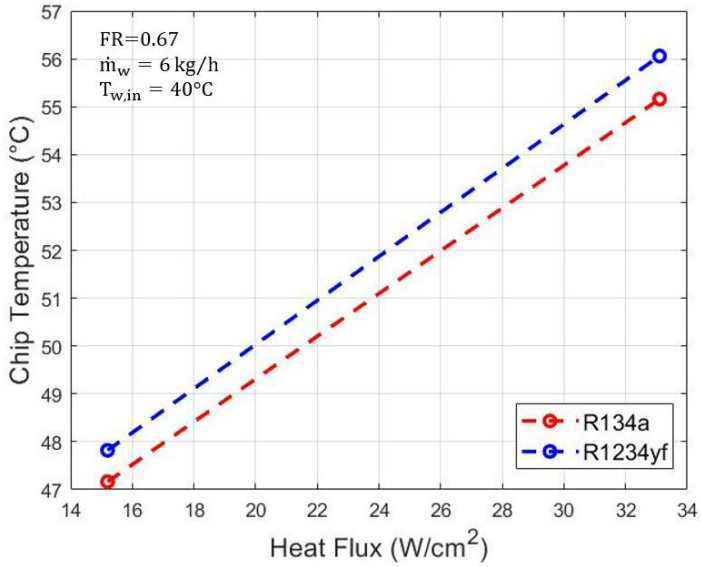

Figure 5.15 – Chip temperature comparison for refrigerants R134a and R1234yf

As expected, Figure 5.13 shows that R134a yields a higher pressure at the inlet of the evaporator. This was also noted by Lamaison et al. (2016b) and mentioned in chapter 2. Since R134a has a lower density difference between the liquid and vapor phases, it presents lower pressure drops and consequently operates with a higher mass flux as observed in Figure 5.13. This leads to R134a being able to keep the temperature of the chip lower than R1234yf (Figure 5.15). Although, the maximum temperature difference was slightly lower than 1°C, in contrast to 4.5°C obtained by the model of Marcinichen et al. (2014) for R1234ze, when compared to R134a, which the authors still reported that was an excellent result.

Figure 5.16 shows the comparison of the safety factors of refrigerants R134a and R1234yf.

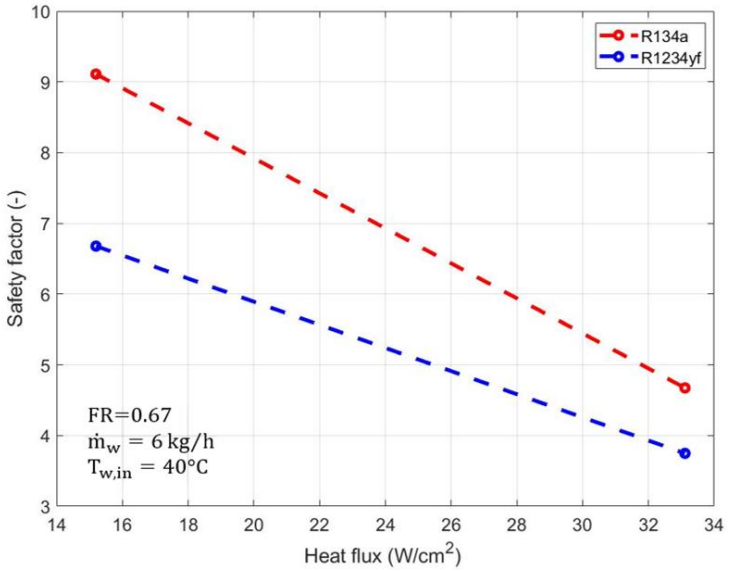

Figure 5.16 –Safety factor comparison for refrigerants R134a and R1234yf

As illustrated by Figure 5.16, the safety factor decreases with the increase of the given heat flux in accordance with Eq. (3.81). In addition, refrigerant R134a presents a higher safety factor for all given heat fluxes. Nevertheless, even for a maximum heat flux of 33.1 W/cm^2, the thermosyphon loop operates with a safety factor higher than 3. Therefore, pointing out a system operation still far from the critical heat flux.

6 Concluding remarks and considerations

The present work developed a numerical modeling for a two-phase thermosyphon loop. The mathematical model was presented for each component of the system, based on fundamental equations of conservation of mass, momentum and energy. Due to the assumption of homogeneous flow, the two-phase properties could be computed from the same set of equations. Empirical correlations were applied to determine the pressure drop due to friction, and the heat transfer coefficients, throughout the entire system. The numerical solution process was presented. It used the Finite Differences Method for one-dimensional flow discretization along the system, and two-dimensional for the thermal conduction in the evaporator package. The numerical model was validated against experimental data, showing good agreement for all variables, when the system was operating under the gravity dominated regime. For the FDR, the numerical model was able to identify the change in regime, however, the numerical model showed a higher discrepancy when comparing results with the experimental data. As pointed out, this may be due to the estimation made on the pressure drop due to bends of the experimental apparatus.

Because of the high GWP of refrigerant R134a (1430), R1234yf (GWP<1) was investigated numerically for the thermosyphon system. Its results were compared with those of R134a and were consistent with expectations. For the same input data, when operating with R1234yf, the system pressure was lower than that of R134a. In this way, the mass flux of refrigerant was also reduced, which led to a higher temperature of the chip. Although refrigerant R1234yf leads to a slightly lower performance than R134a, it was still able to ensure a safe system operation (safety factor above 3 for all heat fluxes), while also providing adequate cooling. Since, for a maximum heat flux of 33.1 W/cm^2, equivalent to a power rejection of approximately 74.74 W, the system maintained the chip temperature below 56°C, which is well below the thermal limit of 85°C. In addition, as previously mentioned, the thermosyphon loop is a promising technology for cooling electronics due to its low, if not zero, electrical energy consumption combined with the high thermal performance due to two-phase flow.

As for final considerations, there is still a need for a detailed sensitivity study to assess the behavior of the system when important parameters, such as the filling ratio, and secondary fluid inlet conditions, are varied. The investigation on time-dependency to achieve a steady-state after a disturbance is administered, results in the need for modeling transient regime. In addition, for practical applications, in order to ensure safer electronic components operation, it is necessary to include a liquid accumulator in the system architecture. With the liquid accumulator, the system will be able to operate under a larger range of heat fluxes.

7 Bibliography

AGOSTINI, B.; BONTEMPS, A. Vertical flow boiling of refrigerant R134a in small channels. **International Journal of Heat and Fluid Flow**, v. 26, n. 2, p. 296–306, 2005.

AGOSTINI, B.; YESIN, B. Modeling of a gravity driven two-phase loop. **Proceedings of the 6th International Conference on Nanochannels, Microchannels, and Minichannels, ICNMM2008**, , n. PART B, p. 1381–1388, 2008.

AGOSTINI, F.; GRADINGER, T.; DE FALCO, C. Simulation aided design of a two-phase thermosyphon for power electronics cooling. **IECON Proceedings (Industrial Electronics Conference)**, p. 1560–1565, 2011. IEEE.

AGOSTINI, F.; HABERT, M.; MOLITOR, F.; et al. Double-loop thermosyphon for electric components cooling. **IEEE Transactions on Components, Packaging and Manufacturing Technology**, v. 4, n. 2, p. 223–231, 2014.

AMALFI, R. L.; SALAMON, T.; LAMAISON, N.; MARCINICHEN, J. B.; THOME, J. R. Two-Phase Liquid Cooling System for Electronics, Part 2: Air-Cooled Condenser. 16th IEEE ITHERM Conference. **Anais...** , 2017a.

AMALFI, R. L.; SALAMON, T.; LAMAISON, N.; MARCINICHEN, J. B.; THOME, J. R. Two-phase liquid cooling system for electronics, part 3: Ultra-compact liquid-cooled condenser. **Proceedings of the 16th InterSociety Conference on Thermal and Thermomechanical Phenomena in Electronic Systems, ITherm 2017**, p. 687–695, 2017b.

AUSSILLOUS, P.; QUÉRÉ, D. Quick deposition of a fluid on the wall of a tube. **Physics of Fluids**, v. 12, n. 10, p. 2367–2371, 2000.

BEATTIE, D. R. H.; WHALLEY, P. B. A simple two-phase frictional pressure drop calculation method. **International Journal of Multiphase Flow**, v. 8, n. 1, Feb. 1982, p. 83–87, 1982.

BIELIŃSKI, H.; MIKIELEWICZ, J. Computer cooling using a two phase minichannel thermosyphon loop heated from horizontal and vertical sides and cooled from vertical side. **Archives of Thermodynamics**, v. 31, n. 4, p. 51–59, 2010.

BIELIŃSKI, H.; MIKIELEWICZ, J. **Natural Circulation in Single and Two Phase Thermosyphon Loop with Conventional Tubes and Minichannels**. InTech, 2011.

BROWN, J. M. **Notes on Numerical Computation: Non-Linear Equations**. UMIST: Department of Computation, September 1977.

CALM, J. M. The next generation of refrigerants - Historical review, considerations, and outlook. **International Journal of Refrigeration**, v. 31, n. 7, p. 1123–1133, 2008.

CATALDO, F.; THOME, J. R. Experimental performance of completely passive single and recirculating loop thermosyphon cooling systems using low GWP R1234ze and R1234yf. **InterSociety Conference on Thermal and Thermomechanical Phenomena in Electronic**

Systems, ITHERM, v. 2019-May, p. 1180–1189, 2019.

CHANG, C. C.; KUO, S. C.; KE, M. T.; CHEN, S. L. Two-phase closed-loop thermosyphon for electronic cooling. **Experimental Heat Transfer**, v. 23, n. 2, p. 144–156, 2010.

CHEN, K. S.; CHANG, Y. R. Steady-state analysis of two-phase natural circulation loop. **International Journal of Heat and Mass Transfer**, v. 31, n. 5, p. 931–940, 1988.

CHU, R.C SIMON, R.E CHRYSLER, G. . Experimental Investigation of an Enhanced Thermosyphon Heat Loopfor Cooling of a High Performance Electronics Module. , p. 1–9, 1999.

CICCHITTI, A. et al. **Two-phase cooling experiments: pressure drop, heat transfer and burnout measurements**. Centro Informazioni Studi Esperienze, Milan. Country unknown/Code not available. 1959.

CIONCOLINI, A.; THOME, J. R. Algebraic turbulence modeling in adiabatic and evaporating annular two-phase flow. **International Journal of Heat and Fluid Flow**, v. 32, n. 4, p. 805–817, 2011. Elsevier Inc.

CIONCOLINI, A.; THOME, J. R. Void fraction prediction in annular two-phase flow. **International Journal of Multiphase Flow**, v. 43, p. 72–84, 2012a. Elsevier Ltd.

CIONCOLINI, A.; THOME, J. R. Entrained liquid fraction prediction in adiabatic and evaporating annular two-phase flow. **Nuclear Engineering and Design**, v. 243, p. 200–213, 2012b. Elsevier B.V.

CIONCOLINI, A.; THOME, J. R.; LOMBARDI, C. Unified macro-to-microscale method to predict two-phase frictional pressure drops of annular flows. **International Journal of Multiphase Flow**, v. 35, n. 12, p. 1138–1148, 2009. Elsevier Ltd.

COLLIER, J. G.; THOME, J. R. **Convective boiling and condensation.** Clarendon Press, 1994.

COSTA-PATRY, E.; THOME, J. R. Flow pattern-based flow boiling heat transfer model for microchannels. **International Journal of Refrigeration**, v. 36, n. 2, p. 414–420, 2013. Elsevier Ltd and IIR.

FRANCO, A.; FILIPPESCHI, S. Closed loop two-phase thermosyphon of small dimensions: A review of the experimental results. **Microgravity Science and Technology**, v. 24, n. 3, p. 165–179, 2012.

FRIEDEL, L. **Improved friction pressure drop correlation for horizontal and vertical two-phase pipe flow**. Proc. of European Two-Phase Flow Group Meet. Ispra, Italy: [s.n.]. 1979.

GNIELINSKI, V. New equations for heat and mass transfer in turbulent pipes and channels flow. **International Chemical Engineering**, v.16, n. 2, p. 359–368, 1976.

GOLDSMITH, H. L.; MASON, S. G. The flow of suspensions through tubes. II. Single large bubbles. **Journal of Colloid Science**, v. 18, n. 3, p. 237–261, 1963.

HAIDER, S. I.; JOSHI, Y. K.; NAKAYAMA, W. A natural circulation model of the closed loop, two-phase thermosyphon for electronics cooling. **Journal of Heat Transfer**, v. 124, n. 5, p. 881–

890, 2002.

HAN, Y.; SHIKAZONO, N. Measurement of liquid film thickness in micro square channel. **International Journal of Multiphase Flow**, v. 35, n. 10, p. 896–903, 2009. Elsevier Ltd.

HAN, Y.; SHIKAZONO, N. The effect of bubble acceleration on the liquid film thickness in micro tubes. **International Journal of Heat and Fluid Flow**, v. 31, n. 4, p. 630–639, 2010. Elsevier Inc.

JENG, H. R.; PAN, C. Analysis of two-phase flow characteristics in a natural circulation loop using the drift-flux model taking flow pattern change and subcooled boiling into consideration. **Annals of Nuclear Energy**, v. 26, n. 14, p. 1227–1251, 1999.

KHALAJ, A. H.; HALGAMUGE, S. K. A Review on efficient thermal management of air- and liquid-cooled data centers: From chip to the cooling system. **Applied Energy**, v. 205, n. August, p. 1165–1188, 2017. Elsevier.

KHEIRABADI, A. C.; GROULX, D. Cooling of server electronics: A design review of existing technology. **Applied Thermal Engineering**, v. 105, n. 2016, p. 622–638, 2016.

KHODABANDEH, R. Thermal performance of a closed advanced two-phase thermosyphon loop for cooling of radio base stations at different operating conditions. **Applied Thermal Engineering**, v. 24, n. 17–18, p. 2643–2655, 2004.

KHODABANDEH, R. Heat transfer in the evaporator of an advanced two-phase thermosyphon loop. **International Journal of Refrigeration**, v. 28, n. 2, p. 190–202, 2005.

LAMAISON, N. **Dynamic Modeling and Experimental Evaluation of a Controlled Two-Phase On-Chip Cooling System Designed for High Efficiency Datacenters PAR**, 2014. École Polytechnique Fédérale de Lausanne.

LAMAISON, N.; AMALFI, R. L.; SALAMON, T.; MARCINICHEN, J. B.; THOME, J. R. Role of a Liquid Accumulator in a Passive Two-Phase Liquid Cooling System for Electronics: Experimental Analysis. **Journal of Electronic Packaging, Transactions of the ASME**, v. 140, n. 1, 2018.

LAMAISON, NICOLAS; MARCINICHEN, J. B.; CHIN LEE ONG; THOME, J. R. Two-phase mini-thermosyphon electronics cooling, Part 4: Application to 2U servers. **2016 15th IEEE Intersociety Conference on Thermal and Thermomechanical Phenomena in Electronic Systems (ITherm)**, v. 90, n. 3, p. 599–609, 2016.

LAMAISON, N.; MARCINICHEN, J. B.; ONG, C. L.; THOME, J. R. Two-phase mini-thermosyphon electronics cooling, Part 3: Transient modeling and experimental validation. **Proceedings of the 15th InterSociety Conference on Thermal and Thermomechanical Phenomena in Electronic Systems, ITherm 2016**, 2016.

LAMAISON, N.; ONG, C. L.; MARCINICHEN, J. B.; THOME, J. R. Two-phase mini-thermosyphon electronics cooling: Dynamic modeling, experimental validation and application to 2U servers. **Applied Thermal Engineering**, v. 110, p. 481–494, 2017.

LAMAISON, N.; ONG, C. L.; MARCINICHEN, J. B.; THOME, J. R. Two-Phase Thermosyphon Cooling of Datacenters. **Encyclopedia of Two-Phase Heat Transfer and Flow III**. p.157–219, 2018.

LEE, J.; MUDAWAR, I. Critical heat flux for subcooled flow boiling in micro-channel heat sinks. **International Journal of Heat and Mass Transfer**, v. 52, n. 13–14, p. 3341–3352, 2009. Elsevier Ltd.

LIN, L.; FAGHRI, A. Steady-state performance in a thermosyphon with tube separator. **Applied Thermal Engineering**, v. 17, n. 7, p. 667–679, 1997.

MAGNINI, M.; THOME, J. R. An updated three-zone heat transfer model for slug flow boiling in microchannels. **International Journal of Multiphase Flow**, v. 91, p. 296–314, 2017. Elsevier Ltd.

MARCINICHEN, J.; AMALFI, R. L.; LAMAISON, N.; SALAMON, T.; THOME, J. R. Two-phase liquid cooling system for electronics, part 4: Modeling and simulations. **Proceedings of the 16th InterSociety Conference on Thermal and Thermomechanical Phenomena in Electronic Systems, ITherm 2017**, , n. August, p. 696–705, 2017.

MARCINICHEN, J. B.; LAMAISON, N.; ONG, C. L.; THOME, J. R. Two-phase mini-thermosyphon electronics cooling, Part 2: Model and steady-state validations. **Proceedings of the 15th InterSociety Conference on Thermal and Thermomechanical Phenomena in Electronic Systems, ITherm 2016**, 2016.

MARCINICHEN, J. B.; SZCZUKIEWICZ, S.; LAMAISON, N.; THOME, J. R. Towards development of a passive datacenter cooling technology: On-server thermosyphon cooling loop under dynamic workload. **Thermomechanical Phenomena in Electronic Systems -Proceedings of the Intersociety Conference**, p. 1027–1037, 2014.

MIN-KYUN NA, JIN-SEOK JEON, HO-YOUN. Experimental Study on Closed-Loop Two-Phase Thermosyphon Devices for Cooling MCMs. **Heat Transfer Engineering**, v. 22, n. 2, p. 29–39, 2001.

MÜLLER-STEINHAGEN, H.; HECK, K. A simple friction pressure drop correlation for two-phase flow in pipes. **Chemical Engineering and Processing**, v. 20, n. 6, p. 297–308, 1986.

MURSHED, S. M. S. Introductory Chapter: Electronics Cooling — An Overview. **Electronics Cooling**, , n. July, 2016.

MUZYCHKA, Y. S.; YOVANOVICH, M. M. Laminar forced convection heat transfer in the combined entry region of non-circular ducts. **Journal of Heat Transfer**, v. 126, n. 1, p. 54–61, 2004.

MUZYCHKA, Y. S.; YOVANOVICH, M. M. Pressure drop in laminar developing flow in noncircular ducts: A scaling and modeling approach. **Journal of Fluids Engineering, Transactions of the ASME**, v. 131, n. 11, p. 1111051–11110511, 2009.

NADJAHI, C.; LOUAHLIA-GUALOUS, H.; LE MASSON, S. Experimental study and analytical modeling of thermosyphon loop for cooling data center racks. **Heat and Mass Transfer/Waerme- und Stoffuebertragung**, v. 56, n. 1, p. 121–142, 2020. Heat and Mass Transfer.

ONG, C. L.; AMALFI, R. L.; JACKSON, B.; LAMAISON, N.; THOME, J. R. TWO-PHASE MINI-THERMOSYPHON FOR COOLING OF DATACENTERS: EXPERIMENTS, MODELING AND SIMULATIONS. , p. 1–12, 2017.

ONG, C. L.; LAMAISON, N.; MARCINICHEN, J. B.; THOME, J. R. Two-phase mini-thermosyphon electronics cooling, Part 1: Experimental investigation. **Proceedings of the 15th InterSociety Conference on Thermal and Thermomechanical Phenomena in Electronic Systems, ITherm 2016**, p. 574–581, 2016. IEEE.

ONG, C. L.; THOME, J. R. Macro-to-microchannel transition in two-phase flow: Part 2 - Flow boiling heat transfer and critical heat flux. **Experimental Thermal and Fluid Science**, v. 35, n. 6, p. 873–886, 2011. Elsevier Inc.

PETUKHOV, B. S. Heat Transfer and Friction in Turbulent Pipe Flow with Variable Physical Properties. **Advances in Heat Transfer**, v. 6, n. C, p. 503–564, 1970.

RAMOS, E.; SEN, M.; TREVIÑO, C. A steady-state analysis for variable area one- and two-phase thermosyphon loops. **International Journal of Heat and Mass Transfer**, 1985.

REASOR, P.; AUTE, V.; RADERMACHER, R. Refrigerant R1234yf Performance Comparison Investigation. International Refrigeration and Air Conditioning Conference. **Anais...** . p.1–7, 2010.

RIBATSKI, G.; WOJTAN, L.; THOME, J. R. An analysis of experimental data and prediction methods for two-phase frictional pressure drop and flow boiling heat transfer in micro-scale channels. **Experimental Thermal and Fluid Science**, v. 31, n. 1, p. 1–19, 2006.

SEURET, A.; IRANFAR, A.; ZAPATER, M.; THOME, J.; ATIENZA, D. Design of a Two-Phase Gravity-Driven Micro-Scale Thermosyphon Cooling System for High-Performance Computing Data Centers. **Proceedings of the 17th InterSociety Conference on Thermal and Thermomechanical Phenomena in Electronic Systems, ITherm 2018**, p. 587–595, 2018.

SHAH, M. M. A general correlation for heat transfer during film condensation inside pipes. **International Journal of Heat and Mass Transfer**, v. 22, n. 4, p. 547–556, 1979.

STEFFENSEN, J. F. Remarks on iteration. **Scandinavian Actuarial Journal**, v. 1933, n. 1, p. 64–72, 1933.

SULAIMAN, M. W.; DARAGHMEH, H. M.; WANG, C. C. Energy-saving potential of separated two-phase thermosiphon loops for data center cooling. **Journal of Thermal Analysis and Calorimetry**, v. 141, n. 1, p. 245–265, 2020. Springer International Publishing.

SZCZUKIEWICZ, S.; LAMAISON, N.; MARCINICHEN, J. B.; THOME, J. R. Passive Thermosyphon Cooling System for High Heat Flux Servers. Proceedings of the ASME 2015

International Technical Conference and Exhibition on Packaging and Integration of Electronic and Photonic Microsystems. **Anais...** . p.1–12, 2015.

TANAKA, K.; HIGASHI, Y. Thermodynamic properties of HFO-1234yf (2,3,3,3-tetrafluoropropene). **International Journal of Refrigeration**, v. 33, n. 3, p. 474–479, 2010. Elsevier Ltd and IIR.

THOME, J. R.; DUPONT, V.; JACOBI, A. M. Heat transfer model for evaporation in microchannels. Part I: Presentation of the model. **International Journal of Heat and Mass Transfer**, v. 47, n. 14–16, p. 3375–3385, 2004.

ZHANG, H.; SHI, Z.; LIU, K.; et al. Experimental and numerical investigation on a CO2 loop thermosyphon for free cooling of data centers. **Applied Thermal Engineering**, 2017.